

A KINEMATICAL THEORY OF DIFFRACTION CONTRAST OF ELECTRON TRANSMISSION MICROSCOPE IMAGES OF DISLOCATIONS AND OTHER DEFECTS

BY P. B. HIRSCH, A. HOWIE AND M. J. WHELAN*

Crystallographic Laboratory, Cavendish Laboratory, University of Cambridge

(Communicated by N. F. Mott, F.R.S.—Received 5 August 1959)

[Plates 3 to 9]

CONTENTS

	PAGE		PAGE
1. INTRODUCTION	499	4. DISCUSSION OF THE APPLICABILITY OF THE THEORY AND ITS RELATION TO DYNAMICAL THEORY	516
2. KINEMATICAL THEORY OF CONTRAST EFFECTS	502	5. COMPARISON OF THEORY WITH EXPERIMENT	518
2.1. Perfect crystal	502	5.1. Nature, width and position of dislocation contrast	518
2.2. Imperfect crystal	505	5.2. Invisible dislocations and determination of Burgers vectors	519
2.3. Stacking fault	506	5.3. Double images of dislocations	522
3. CONTRAST AT DISLOCATIONS	507	5.4. Images of dislocation loops	523
3.1. Nature of the problem	507	5.5. The interpretation of X-ray topographs	524
3.2. Amplitude-phase diagrams	508	6. CONCLUSION	525
3.3. Intensity profiles of dislocation images	512	APPENDIX. CALCULATION OF THE COORDINATES ξ_n AND η_n	526
3.4. Extension of the theory to other dislocation configurations	514	REFERENCES	528
3.5. Effect of divergence of the incident beam	516		

This paper describes a kinematical theory of electron microscope images of dislocations observed by transmission in thin crystalline foils. The contrast is essentially phase contrast in the Bragg diffracted beams, the phase differences being due to the displacements of the atoms from their positions in the ideally perfect crystal. The theory explains many of the characteristic features of the observed images, such as the dependence of the contrast on orientation, the reversal of contrast on bright and dark field images, the fact that dislocations are generally dark on bright field images, the position and width of the images, the general nature of the profile, the occurrence of dotted dislocations, the invisibility of some dislocations, the dependence of contrast on the inclination of the dislocation, and the occurrence of double images. The theory also accounts satisfactorily for the nature and width of the dislocation images obtained with X-rays.

1. INTRODUCTION

In the last few years the transmission electron microscope technique has become widely used for studying crystal imperfections such as dislocations and stacking faults (Menter 1956; Hirsch, Horne & Whelan 1956; Bollmann 1956, 1957; Whelan, Hirsch, Horne & Bollman 1957; Nicholson & Nutting 1958; for review see Menter 1958; Hirsch 1959; Nutting 1959).

* Now a Mr and Mrs John Jaffé Donation Student.

Essentially three methods have been employed for revealing lattice defects. In the first of these, due to Menter (1956), the lattice planes are resolved directly by ensuring that direct and diffracted waves enter the aperture of the objective lens of the imaging system. When the spacing of the lattice planes is too small to be resolved in present-day electron microscopes, moiré patterns due to overlapping crystals can be used to give images which, under certain conditions, can be considered essentially as magnified images of the crystal lattice (Hashimoto & Uyeda 1957; Bassett, Menter & Pashley 1958). Both these methods reveal the nature of the distortion of the lattice planes near a defect and depend for their success on good resolution and rather stringent specimen requirements. For example, the specimens must be relatively thin to avoid excessive chromatic aberration due to energy losses.

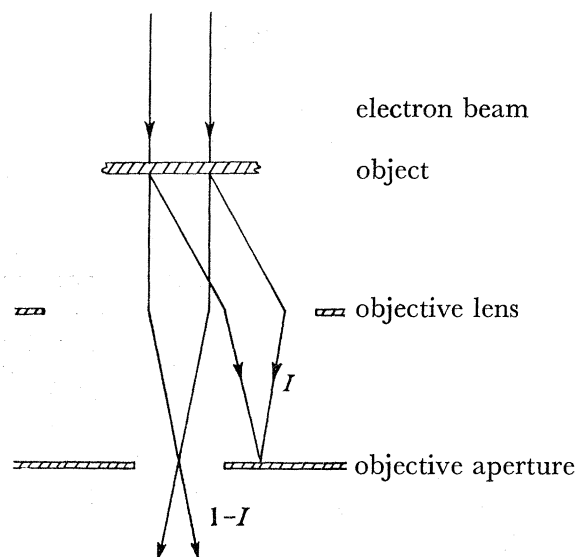


FIGURE 1. Illustrating diffraction contrast. The incident electron beam is diffracted by the specimen and the diffracted beam is removed by the aperture of the objective lens. The intensity of the incident beam is unity, that of the diffracted beam I and that of the transmitted beam $1 - I$. Contrast arises through local variations of the intensities of the diffracted beams.

In the third method, first investigated independently by Bollmann (1956) and by Hirsch *et al.* (1956), image contrast is produced by local differences in the intensities of the Bragg diffracted beams. It is generally arranged that only the direct beam (bright field image) or one diffracted beam (dark field image) enters the aperture of the objective lens (see figure 1). In the bright field image, dark contrast results wherever local conditions in the crystal lead to strong diffraction. This 'diffraction contrast' is sensitive to changes in orientation or thickness, and to displacements of the atoms from their normal positions due to lattice strains. In the perfect crystal this type of contrast is responsible for 'extinction contours', which are bands of constant orientation or of thickness corresponding to conditions of particularly strong diffraction. In the imperfect crystal, dislocations appear as lines because of the atomic displacements near them, and stacking faults give rise to a characteristic fringe pattern. This method of contrast formation has the advantage that the atomic array is not resolved, that resolution is therefore not a limiting factor, and that specimen requirements are less stringent. For example, a projection of the three-dimensional arrangement of dislocations can be obtained for crystals whose thickness would be too great for

resolution of lattices or of moiré patterns of small spacings. The main application of this method is in the study of the distribution of defects and also of their behaviour, for example, on heating or straining the specimen, while the first two methods are particularly suitable for the study of the nature of the atomic displacements near the defect.

So far no complete theory of contrast for any of these methods is available. Most of the ideas on contrast in the image formed by the electron microscope (Scherzer 1949; Haine 1957; Lenz 1958) seem to be based on theories dealing with the scattering from single atoms (Lenz 1954). In general, of course, the contrast in electron microscope images is determined by the amplitude and phase distribution of the electron waves passing through the objective aperture. Theories in which this distribution is worked out for single atoms apply strictly only to a specimen in which all atoms scatter independently, and therefore can at best only be considered as crude approximations in the case of the most amorphous solids. Even solids such as amorphous carbons give scattering curves which differ considerably, particularly in the all-important low-angle region, from those expected from independently scattering atoms (see, for example, Franklin 1950). This point has been emphasized by Niehrs (1958 *a*), and is understandable, for if atoms are adjacent to each other, the phase relation between their scattered amplitudes becomes important. The general problem in the case of crystals as for other solids involves the calculation of the distribution of amplitude and phase in the transmitted beam. This has been discussed for the case of lattice resolution by Menter (1956, 1958), Niehrs (1958 *b*), and Hashimoto, Naiki & Mannami (1958), for moiré patterns by Bassett *et al.* (1958), Dowell, Farrant & Rees (1958), Hashimoto *et al.* (1958), and Kamiya, Nonoyama, Tochigi & Uyeda (1958), and for diffraction contrast for various cases by Heidenreich (1949), Kato (1952 *a, b*, 1953) and Whelan & Hirsch (1957 *a, b*). There is, however, as yet no theory of diffraction contrast from dislocations. It is the aim of the present paper to develop an approximate theory which will make it possible to interpret correctly most of the contrast features which are observed on electron micrographs.

To describe the diffraction contrast from dislocations completely, a dynamical theory taking account of the equilibrium between the waves in the imperfect crystal is required, but in spite of the urgent need for such a theory for the correct interpretation of electron micrographs this problem is still unsolved. However, a 'correspondence principle' exists whereby the results of dynamical theory become asymptotic to those of the so-called kinematical theory of diffraction, for large enough deviations from the Bragg angle or for sufficiently thin crystals. Under these conditions the kinematical theory predicts correctly the intensity of the diffracted beam at an infinite distance from the crystal. Most of the interference between the diffracted waves takes place in the crystal itself, and it will be assumed that the diffracted waves at the lower crystal surface (figures 2 and 4) are essentially plane. The diffracted amplitude emerging from any small area of the lower surface of the crystal (at *B* in figure 2) can then be regarded as coming from a column *AB* drawn in the direction of the diffracted beam. The kinematical theory gives an expression for the amplitude of this beam, both in the perfect crystal and in the imperfect crystal, when the atoms in the column are displaced from their equilibrium positions. The application of this method to the case of an imperfect crystal containing dislocations is justified by the fact that the diffracted beams from such a crystal are mainly concentrated in directions very close to those corresponding to a perfect crystal (Wilson 1950; Suzuki, reported by Willis 1957),

and that therefore the waves at the lower surface of the crystal may again be expected to be approximately plane. The calculation of the intensity diffracted from a column as a function of its position in the crystal leads in the first instance to a description of the dark field image, and the bright field image is obtained on the assumption that the two images are complementary. Alternatively, the bright field image can be found directly by calculating the intensity diffracted away from a column in the direction of the direct beam.

In the cases where the dynamical theory has been used, i.e. for the perfect crystal and for the crystal containing a stacking fault, the results predicted by the simple kinematical theory are in good qualitative agreement with those of the more accurate treatment. Some confidence is therefore placed in extending the kinematical theory to the dislocated crystal, and the experimental confirmation of many of its predictions is further justification of the method.

2. KINEMATICAL THEORY OF CONTRAST EFFECTS

2.1. Perfect crystal

A thin crystal free of defects such as dislocations, faults, etc., but possibly containing long wavelength strains due to bending, is called a perfect crystal. The method of the kinematical theory is illustrated in figure 2, where only one diffracted beam is considered. The intensity

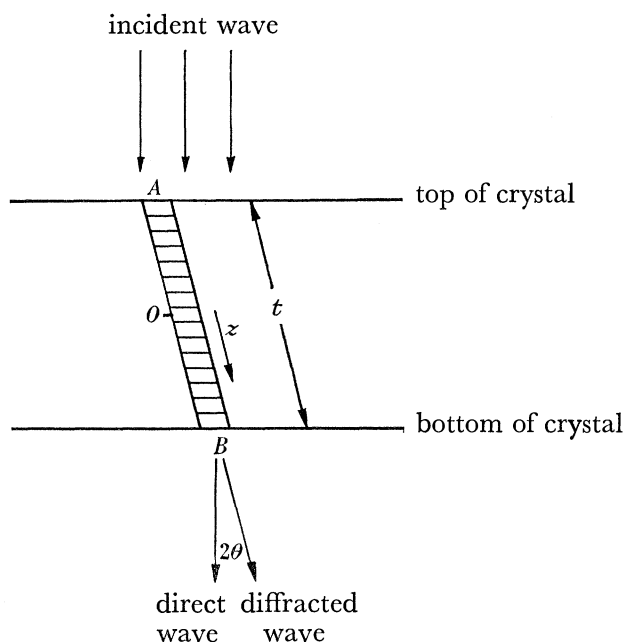


FIGURE 2. Section through a thin crystal showing the column of crystal chosen for calculating the intensity of the dark field image. The column is inclined in the direction of the diffracted beam.

of the dark field image is obtained by calculating the amplitude scattered by a column of crystal in the direction of the diffracted beam shown shaded in figure 2. The amplitude diffracted by the column is

$$A = \sum_j F_j \exp(2\pi i(\mathbf{g} + \mathbf{s}) \cdot \mathbf{r}_j), \quad (1)$$

where F_j is the scattering factor for electron waves of the contents of the unit cell situated at \mathbf{r}_j in the column, \mathbf{g} is the reciprocal lattice vector corresponding to the Bragg reflexion, and

\mathbf{s} is a small vector indicating a deviation of the reciprocal lattice point from the reflecting sphere. Since \mathbf{g} is a reciprocal lattice vector, and \mathbf{r}_j is a lattice vector, the product $\mathbf{g} \cdot \mathbf{r}_j$ is an integer.

Hence for a perfect crystal

$$A = \sum_j F_j \exp(2\pi i \mathbf{s} \cdot \mathbf{r}_j). \quad (2)$$

If all the unit cells are similar, the F_j 's are constant and can be taken outside the summation sign. The summation is then replaced by an integral, and taking the origin O at the middle of the column in figure 2, the amplitude A is found to be proportional to $\{\sin \pi t s\}/\pi s$ and the intensity I proportional to

$$(\sin^2 \pi t s)/(\pi s)^2, \quad (3)$$

where t is the thickness of the crystal measured along the column and s is the distance of the reciprocal lattice point from the reflecting sphere, also measured along the column. This is the familiar expression for the kinematical intensity distribution around a reciprocal lattice point for a crystal of thickness t , which gives rise to a spike in reciprocal space along the direction of t . Now expression (2) gives the amplitude scattered in a particular direction from a column one unit cell diameter thick. For each reflexion the diffracted rays from such a column are actually spread out over a whole range of directions. However, because of the interference in the crystal between rays diffracted from neighbouring columns the rays at the bottom surface will be concentrated in a small range of angles around that corresponding to the reciprocal lattice point for the operating reflexion. The total intensity diffracted from a column in this small range of angles is given by an expression identical to (3), where the proportionality factor is obtained by calculating the average intensity per unit area of cross-section from a column of finite lateral dimensions and integrating the intensity scattered over the reflecting sphere. In this way the factor is found to be $F^2/k^2 V^2 \cos^2 \theta$ (for the symmetrical Laue case where incident and diffracted beams are inclined at the same angle θ to the normal to the foil surface); $k = \lambda^{-1}$ is the wave vector of the incident electron wave, V is the volume of the unit cell, θ is the Bragg angle, and F is the scattering factor of the contents of a unit cell for electron waves. In most of the subsequent discussion this factor will be omitted. The angle θ is usually of the order of one or two degrees so that the column can be effectively considered as being normal to the crystal surface. Equation (3) shows that the intensity of the diffracted wave oscillates sinusoidally with t for fixed s , a result which is well known from dynamical theory.

The calculation of diffracted amplitudes is conveniently illustrated by means of an amplitude-phase diagram as shown in figure 3. The amplitude scattered by an element of the column lying between depths z and $z + dz$ (measured along the column) is proportional to dz and has a phase angle $2\pi s z$. The amplitude-phase diagram (which represents the sum of all the elements of amplitude scattered by the various parts of the column) is therefore a circle of radius $(2\pi s)^{-1}$, i.e. analogous to the case of diffraction by a slit in physical optics. If we choose the phase zero in the middle of the column, the amplitudes from the top and bottom halves of the crystal in figure 2 are represented by PO and OP' in figure 3, where the arcs PO and OP' are equal to $\frac{1}{2}t$. The resultant amplitude is PP' and as t varies PP' will oscillate. The average diffracted amplitude is proportional to s^{-1} and the average diffracted intensity to s^{-2} . The depth periodicity of the intensity oscillation is $t'_0 = s^{-1}$.

Figure 4 shows schematically the intensity variations of the direct and diffracted waves in the crystal. As s decreases the wavelength of the oscillations t'_0 increases, i.e. the radius of the circle in figure 3 increases. According to the kinematical theory t'_0 may increase indefinitely. However, for small s dynamical effects become important, and the results of this theory mentioned in §4 show that t'_0 has an upper limit t_0 known as the extinction distance for the Bragg reflexion. The depth variation of intensities of direct and diffracted waves gives rise to

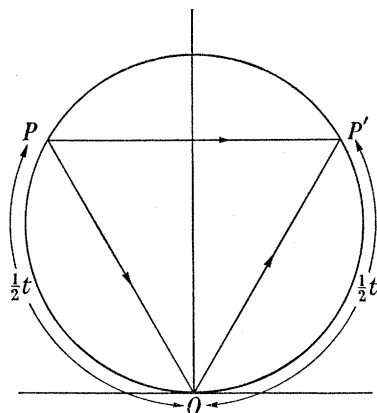


FIGURE 3. Amplitude-phase diagram for a perfect crystal. The circle is of radius $(2\pi s)^{-1}$. PP' is the amplitude diffracted from a crystal of thickness t . The intensity is PP'^2 . As s or t varies the value of PP' will oscillate.

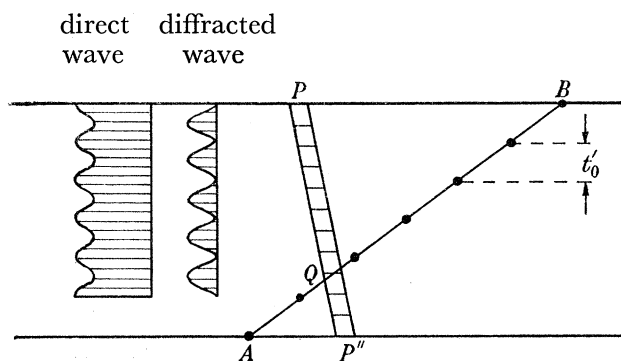


FIGURE 4. Cross-sectional diagram illustrating schematically the intensity oscillations of direct and diffracted waves as a function of depth in the crystal in the kinematical case. The depth periodicity of the intensity oscillations is $t'_0 = s^{-1}$. AB is an inclined plane of discontinuity of crystal structure such as a stacking fault, grain boundary, or a crystal surface of a wedge crystal. Fringes will be visible over the region AB . The number of fringes visible is determined essentially by the depth periodicity t'_0 and the crystal thickness. The circles represent the points along AB at which the intensity of the diffracted beam is zero.

thickness extinction contours (Heidenreich 1949). For a wedge-shaped crystal (figure 4) the intensity of the directly transmitted wave will clearly vary along the wedge. Figure 5(a), plate 3, is an example of thickness extinction contours in an aluminium foil containing a depression over a local region; the fringes are contours of equal thickness of the foil. Similar fringes are also observed at grain boundaries running obliquely through the foil (figure 5(c)), and also, as will be seen later, at stacking faults on oblique planes (figure 5(d)). A foil of uniform thickness may show extinction contours due to buckling (Heidenreich 1949). In this case t is fixed and s varies across the foil so that the reflecting sphere sweeps through the

intensity distribution around the reciprocal lattice point. This gives rise to multiple fringes corresponding to the various intensity maxima of equation (3). An example of such bend contours in aluminium is shown in figure 5(b). Again, it is found that the kinematical theory gives an adequate qualitative account of the features of the contour, although dynamical theory is required for a detailed interpretation.

2.2. Imperfect crystal

A defect generally causes displacements of the atoms from their ideal positions, and if impurity atoms are involved, local changes in the scattering factor F . The latter effect can of course be taken into account, but in this discussion only the atomic displacements which usually have a more important effect on the contrast will be considered.

The amplitude diffracted by a column of imperfect crystal is then given by

$$A = F \sum_j \exp(2\pi i(\mathbf{g} + \mathbf{s}) \cdot (\mathbf{r}_j + \mathbf{R})), \quad (4)$$

where \mathbf{R} is the displacement of the cell from the ideal position \mathbf{r}_j . \mathbf{R} may in general be a function of \mathbf{r}_j , as for a dislocation. This reduces to

$$A = F \sum_j \exp(2\pi i\mathbf{g} \cdot \mathbf{R}) \exp(2\pi i\mathbf{s} \cdot \mathbf{r}_j), \quad (5)$$

where the product $\mathbf{s} \cdot \mathbf{R}$ in the exponent of (4) has been neglected in comparison with the other terms, since R is usually of atomic dimensions or less, while s is usually the reciprocal of a macroscopic dimension. Thus the displacement of a cell produces a phase angle $\alpha = 2\pi\mathbf{g} \cdot \mathbf{R}$ in the scattered wave, and the resultant amplitude given by equation (5) will differ from that from a perfect crystal. The contrast therefore arises through a phase-contrast mechanism, the phase difference being produced by atomic displacements. Equation (5) may be approximated by an integral. Leaving out the factor F/V

$$A = \int_{\text{column}} \exp(i\alpha) \exp(2\pi i\mathbf{s}z) dz, \quad (6)$$

where α is a function of z , depending on both the reflexion \mathbf{g} and the displacement \mathbf{R} . The amplitude is essentially the Fourier transform of the phase factor $\exp(i\alpha)$ over the whole column.

As in the case of a perfect crystal the resultant contrast is obtained by taking into account the interference between neighbouring columns and integrating the diffracted intensity over the range of angles around that corresponding to the reciprocal lattice point. We appeal here to the results of the theories of diffraction from crystals containing stacking faults (Paterson 1952) or dislocations (Wilson 1950; Suzuki, reported by Willis 1957) that in both these cases this range of angles is still small. If the range of angles in the diffracted beam at the lower surface of the crystal is $d\phi$, the rays contributing to the amplitude at any point on the lower surface will come from a column of diameter $\sim t d\phi$, where t is the length of the column. The range of angles $d\phi$ is generally quite small; for example, for a crystal of diameter t containing a dislocation, $d\phi \sim \mathbf{b}/t$ (where \mathbf{b} is the Burgers vector) so that the diameter of the contributing column is of atomic dimensions. This means that the intensity at any point on the lower surface of the crystal will depend mainly on the displacements in the column passing through that point, and will be relatively unaffected by those in neighbouring

columns; the total diffracted intensity will be approximately proportional to $|A|^2$, the factor of proportionality being the same as that for the perfect crystal (see §2.1). This is true for crystals with stacking faults, for which the results of the dynamical theory for large deviations from the Bragg angle are found to be identical with those of the kinematical theory (Whelan & Hirsch 1957*a, b*). The above arguments suggest that the same conclusions apply to crystals with dislocations.

2.3. Stacking fault

A simple example which illustrates the use of amplitude-phase diagrams is the case of a stacking fault in a face-centred cubic crystal. Suppose the fault runs obliquely across the foil as shown in figure 4. The two parts of the crystal separated by the fault are displaced

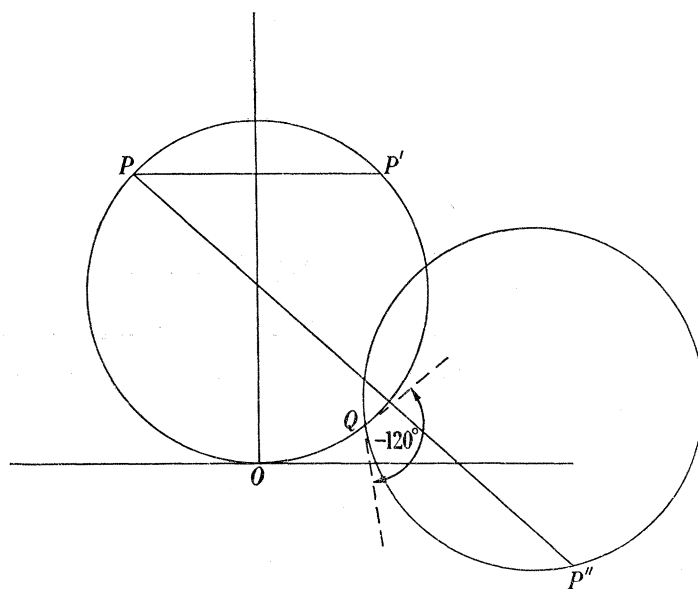


FIGURE 6. Amplitude-phase diagram for a face-centred cubic crystal containing a stacking fault (figure 4).

relative to each other parallel to the fault plane by the vector $\mathbf{R} = \frac{1}{8}[112]$. This produces a phase difference α in waves diffracted from opposite sides of the fault equal to $\frac{1}{3}\pi[h+k+2l]$, where h, k and l are the indices of the Bragg reflexion. The possible values of α are $\pm 120^\circ$ or 0° depending on the indices of the reflexion. The amplitude-phase diagram for $\alpha = -120^\circ$ is shown in figure 6, where the point O corresponds to the middle of the column in figure 4. The circle POP' of radius $(2\pi s)^{-1}$ is called the initial circle; this is the amplitude-phase diagram for the unfaulted crystal. At the point Q on this circle corresponding to the intersection of the column and the fault plane an abrupt change of phase -120° occurs. The amplitude-phase diagram thereafter follows the final circle, also of radius $(2\pi s)^{-1}$ passing through Q and making an angle of -120° with the initial circle. The amplitude from the part of the column above the fault is PQ , while that from the bottom part is QP'' . The resultant amplitude is PP'' , which in general is different from PP' , the amplitude from the unfaulted crystal. If the fault runs obliquely across the foil, P is fixed (figure 6) but Q and P'' and hence PP'' vary as the position of the column is changed. For any two points on the fault whose depths differ by t'_0 , Q occupies identical positions on the initial circle. The corresponding difference in length of the column in the lower crystal will also be t'_0 and hence

the two positions of P'' are also identical. Thus PP'' will have the same value for these points on the fault. It follows that the contrast is in the form of fringes parallel to the intersection of the fault with the foil surface, the periodicity of the fringes being determined by t'_0 . An example of stacking-fault fringes is shown in figure 5 (*d*). The resultant intensity distribution in the fringes can of course be obtained from equation (6).

3. CONTRAST AT DISLOCATIONS

3.1. Nature of the problem

In this section the method of the kinematical theory outlined in the previous section will be applied to the case of a dislocation. If one looks down on a thin crystal containing a dislocation parallel to the surface, the line of vision passing through the centre of the dislocation, it

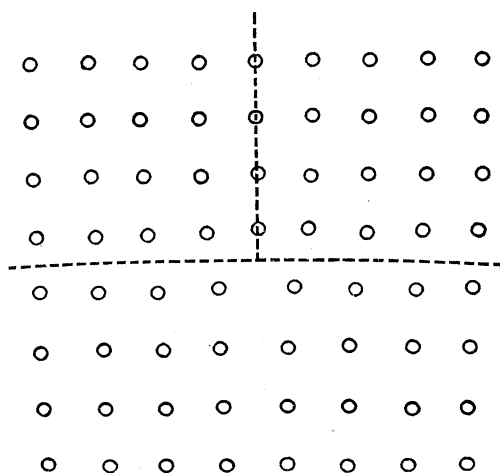


FIGURE 7. Diagram illustrating the local rotation of lattice planes near an edge dislocation in a simple cubic lattice (courtesy Clarendon Press).

is readily seen that the atoms above the dislocation are displaced relative to those below by an amount equal to half the Burgers vector. (This is most easily seen for pure screw or edge dislocations; see, for example, Read (1953).) Thus if the column of figure 2 passes through the centre of the dislocation an abrupt change of phase occurs, and the calculation of contrast is similar to that for a fault. For other positions of the column not passing through the centre of the dislocation, the column is continuously deformed so that the phase angle $\alpha = 2\pi\mathbf{g}\cdot\mathbf{R}$ becomes a continuous function of position. In this simple way it is easy to see how contrast arises.

One significant feature of the contrast from dislocations can be deduced immediately from the fact that the atomic displacements on opposite sides of the dislocation are in opposite directions. (This is shown for an edge dislocation in figure 7.) In equation (6) the phase angle α due to displacement will add to that due to depth in the crystal (i.e. the phase angle $2\pi sz$) on one side of the dislocation, and will subtract from it on the other side. In the former case the effect of the dislocation is to bring the crystal locally further from, and in the latter case nearer to the reflecting position. Generally, therefore, the contrast will lie on one side of the centre of the dislocation. This can also be interpreted in terms of a local rotation of lattice planes, which can be seen for an edge dislocation in figure 7. The conclusions that the

sense of the phase angle and the rotation of the lattice planes are opposite on opposite sides of a dislocation, and that the contrast appears only on one side, apply to dislocations of all types.

3.2. Amplitude-phase diagrams

For the construction of amplitude-phase diagrams and associated calculations for the column of crystal near a dislocation, the simplest case to consider is that of a screw dislocation parallel to the surface of a thin foil and at distances of z_1 and z_2 from the top and bottom surfaces. Figure 8 shows the arrangement and the co-ordinate system used. The atomic displacements around the screw are taken to be the same as in an infinite medium, i.e.

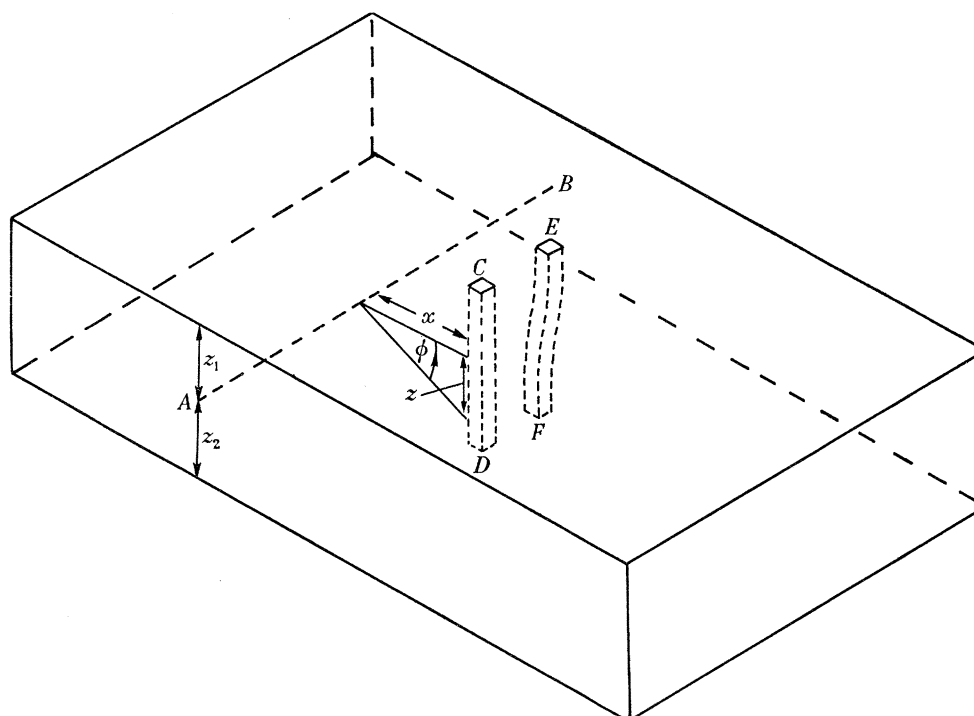


FIGURE 8. Crystal containing a screw dislocation AB parallel to the plane of the foil. A column of crystal CD in the perfect crystal is deformed to shape EF after introduction of the screw dislocation. The diagram illustrates the choice of parameters x , z and ϕ .

the effects of image dislocations in the surfaces are neglected. If these are included additional complications are introduced, but it is thought that the main qualitative results will be unaffected, provided the dislocation is not too close to the surface. Figure 8 shows the nature of the displacements; a column of crystal CD is deformed to a shape EF after introduction of the screw dislocation AB .

The displacement vector $\mathbf{R} = \mathbf{b}\phi/2\pi = (\mathbf{b}/2\pi) \tan^{-1}(z/x)$, where \mathbf{b} is the Burgers vector of the dislocation. Hence

$$\alpha = 2\pi\mathbf{g} \cdot \mathbf{R} = \mathbf{g} \cdot \mathbf{b} \tan^{-1}(z/x) = n \tan^{-1}(z/x). \quad (7)$$

Since \mathbf{g} is a reciprocal lattice vector and \mathbf{b} is an interatomic vector, n is an integer which may take positive and negative values and zero. $n\pi$ is the phase difference between waves scattered immediately above and below the dislocation. Since the atomic scattering factor decreases rapidly with increasing scattering angle the diffracted beams corresponding to small values

\mathbf{g} are most important in producing contrast, and in this paper the values of n considered are of $n = 0, 1, 2, 3, 4$, (n can always be regarded as positive provided the sign of x is suitably adjusted). The case $n = 0$, i.e. $\alpha = 0$, corresponds to \mathbf{g} and \mathbf{b} being perpendicular to each other. This case in which the dislocation is invisible will be mentioned later (§5.2). Now \mathbf{g} is perpendicular to the reflecting planes, and this condition implies that displacements parallel to the reflecting planes produce no contrast. In particular since the Bragg angles are small, displacements parallel to the incident beam, i.e. approximately normal to the foil surface produce no contrast.

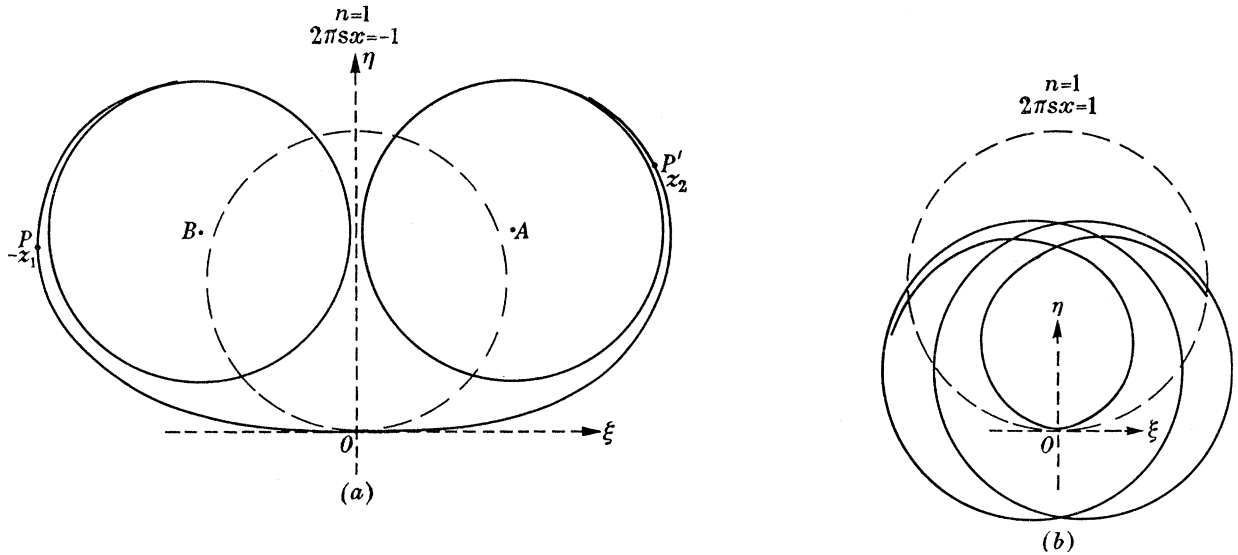


FIGURE 9. Amplitude-phase diagrams for a column of crystal close to a screw dislocation (figure 8). The radius of the broken circle is $(2\pi s)^{-1}$. The diagram is an unwound spiral (a) or wound-up spiral (b). The diagrams (a) and (b) refer to $n = 1$, $2\pi s x = -1$ and $2\pi s x = +1$, respectively. There is a different diagram for each value of $2\pi s x$. The amplitude diffracted by the column of crystal EF in figure 8 is obtained by joining points PP' corresponding to the top and bottom of the column. The separation between the points P and P' measured along the curves is equal to the crystal thickness. The amplitude diffracted from one side of the dislocation (a) is greater than that from the other side (b).

Substitution of (7) in equation (6) gives

$$A = \int_{-z_1}^{+z_2} \exp(in \tan^{-1} z/x + 2\pi isz) dz. \tag{8}$$

Since the integral (8) is an expression for the amplitude-phase diagram (z being distance measured along the curve and $n \tan^{-1} z/x + 2\pi isz$ the slope), diagrams for various situations can be constructed graphically with tolerable accuracy (figures 9, 10 and 14). The following points are to be noted.

(a) The size of the diagram, and therefore the amplitude, are proportional to s^{-1} as in the case of a perfect crystal or a crystal with a stacking fault. The form of the diagram depends on two parameters only, namely, n and $\beta = 2\pi s x$. For fixed s , β will vary with x and $-\infty \leq \beta \leq \infty$. The centre of the dislocation corresponds to $\beta = 0$.

(b) In figure 9(a) and (b) the circle corresponding to the perfect crystal is shown by a broken line. This is called the original circle. O corresponds to $z = 0$ in figure 8, i.e. to the

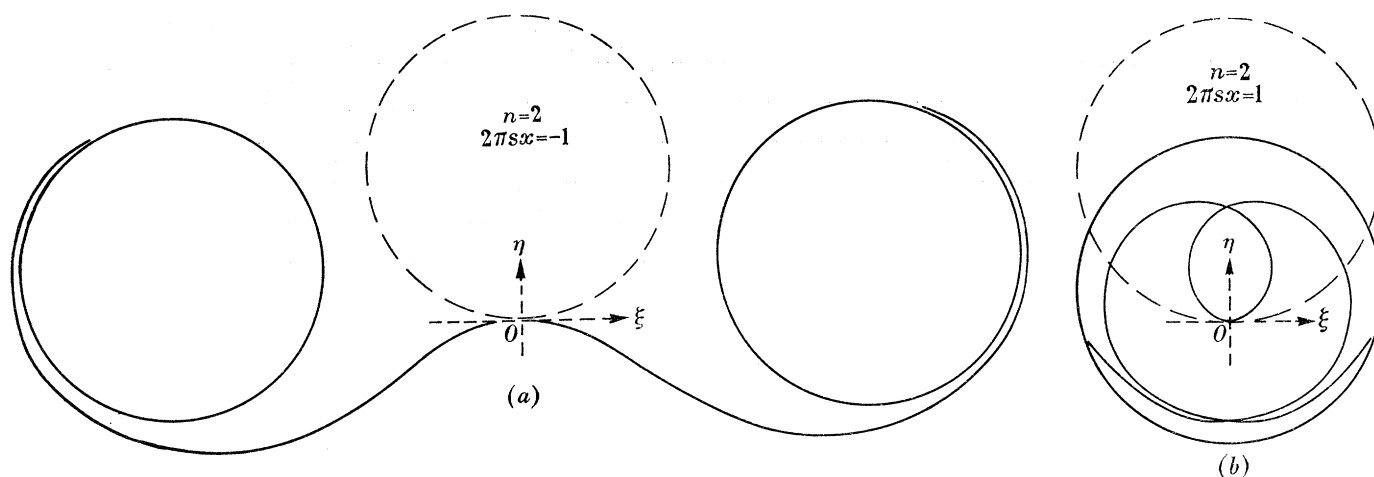


FIGURE 10. Amplitude-phase diagrams for a screw dislocation for $n = 2$, $2\pi s x = \pm 1$.

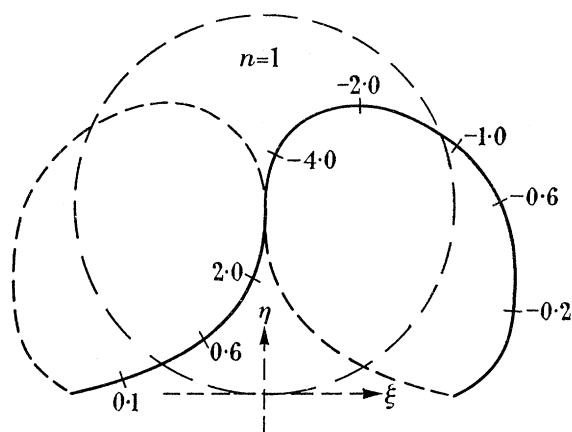


FIGURE 11. Full curve: locus of the centre of the final circle (A in figure 9) as $\beta (= 2\pi s x)$ varies. Broken curve, similar locus of the centre of the initial circle (B in figure 9). The diagram is for $n = 1$, and values of β are marked on the locus. The broken circle represents the original circle of radius $(2\pi s)^{-1}$.

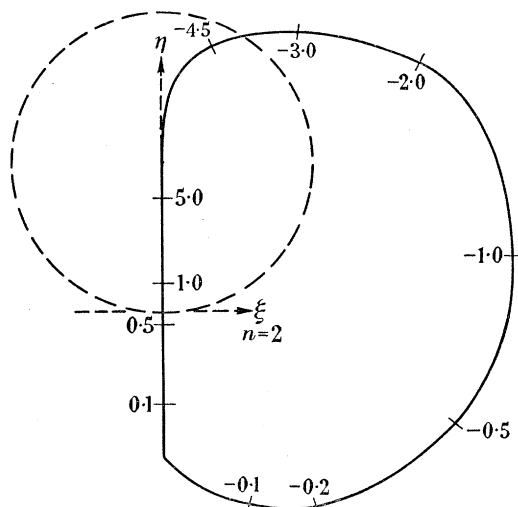


FIGURE 12. Locus of the centre of the final circle for $n = 2$. The broken circle is the original circle of radius $(2\pi s)^{-1}$. Values of $\beta (= 2\pi s x)$ are marked on the locus.

point on the column nearest the dislocation. At the top of the column CD in figure 8 the crystal is nearly perfect, so that the resultant amplitude scattered from such a region is a chord of a curve which is asymptotic to a circle of radius $(2\pi s)^{-1}$ centred at B in figure 9(a). Similar considerations hold for the part of the column near the bottom of the foil remote

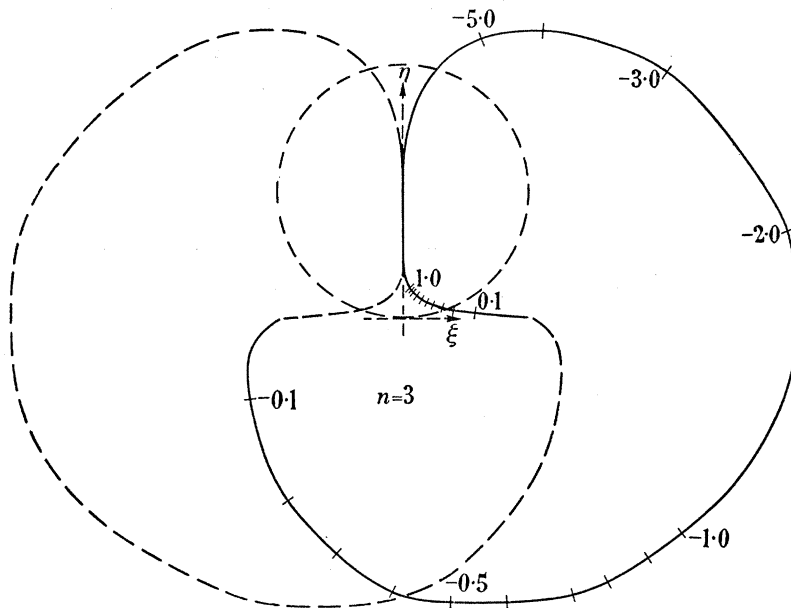


FIGURE 13. Loci of the centres of the initial circle (broken curve) and final circle (full curve) for $n = 3$. The broken circle is the original circle of radius $(2\pi s)^{-1}$. Values of $\beta (= 2\pi s x)$ are marked on the locus.

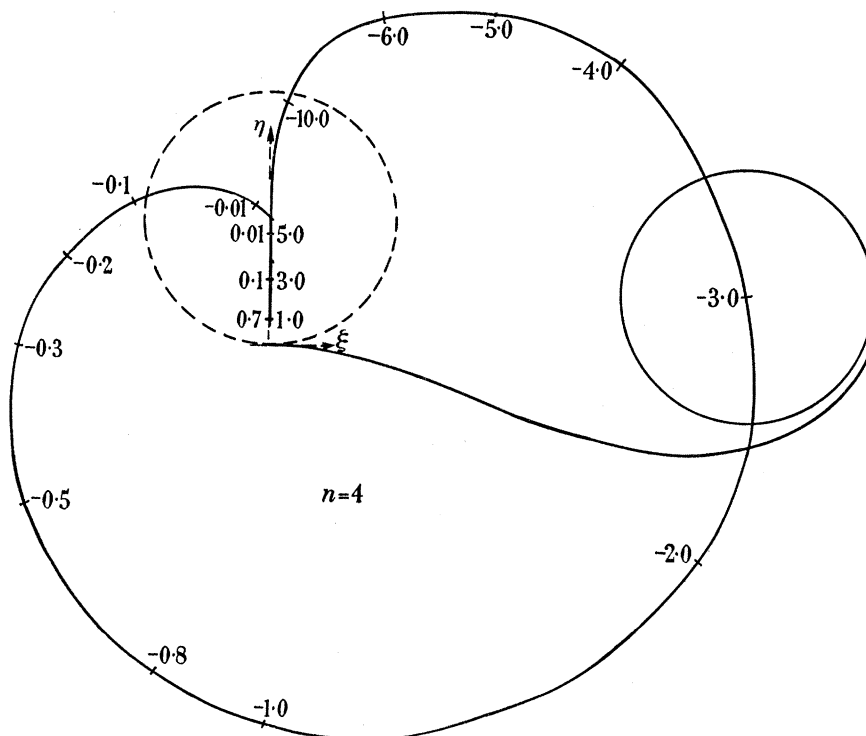


FIGURE 14. Locus of the centre of the final circle for $n = 4$. The broken circle is the original circle of radius $(2\pi s)^{-1}$. Values of $\beta (= 2\pi s x)$ are marked on the locus. The diagram also shows a graphically constructed amplitude-phase diagram for $\beta = 2\pi s x = -3$.

from the dislocation. Here the amplitude-phase diagram is asymptotic to a circle of radius $(2\pi s)^{-1}$ centred at A in figure 9(a). These two circles are called the initial and final circles, respectively. The complete amplitude-phase diagram is a double spiral curve connecting the initial and final circles. It will be noted that two types of spiral occur; these are shown in figures 9 and 10. For negative β the phase angles in the integral (8) subtract and the resultant spiral can be regarded as generated by unwinding the original circle (figures 9(a) and 10(a)). For positive β the phase angles are additive and the spiral winds up (figures 9(b) and 10(b)).

(c) The significance of the amplitude-phase diagram is as follows. The amplitude diffracted by a column $-z_1 \leq z \leq z_2$ is given by the line joining the points PP' corresponding to $-z_1$ and z_2 on figure 9(a). Usually P and P' will be near the initial and final circles, respectively. The arc length PP' along the double spiral is proportional to $z_1 + z_2$.

(d) For a dislocation in an unbent uniform foil z_1, z_2, s and n are fixed for a given reflexion, and the amplitude diffracted will vary with x , i.e. with $\beta = 2\pi s x$. As β varies the centre of the final circle (with co-ordinates ξ_n and η_n) describes a locus which passes through the centre of the original circle when $\beta = \pm \infty$ (this corresponds to a column far from the dislocation where the crystal is perfect). Figures 11 to 14 show the loci for $n = 1, 2, 3, 4$; values of β are marked on the loci. The co-ordinates ξ_n and η_n have been calculated from the integral (8) with $z_1 = 0$ and $z_2 = \infty$. The calculation is given in the appendix. Knowing the centre of the final circle the amplitude-phase diagram can be constructed graphically. As β varies the initial circle also moves along a locus which is the reflexion of the above locus in the η axis. When $x = \beta = 0$, $\alpha = n \tan^{-1} z/x = \frac{1}{2}n\pi$ (neither s nor $z = 0$). The final circle in this case must pass through the origin and make an angle $\frac{1}{2}n\pi$ with the original circle. These simple considerations are sufficient to fix the initial and final points of the locus.

3.3. Intensity profiles of dislocation images

Inspection of a typical amplitude-phase diagram, e.g. figure 9(a), shows that the diffracted amplitude PP' consists of two parts—a steady component represented by the distance between the centres of the two circles $BA = 2\xi_n$ and a fluctuating part depending on the exact positions of the points P and P' near these circles. As x varies both these contributions to the diffracted amplitude will change, but since the angular position of P' near its circle behaves like $\tan^{-1} z_2/x$ it can be taken as constant for $|x| < \frac{1}{4}z_2$ say. In practice this means that all the variation of the diffracted amplitude within the region where the contrast in the image is appreciable comes from the steady component. Since the amplitude is also proportional to $(2\pi s)^{-1}$, a convenient measure of the diffracted intensity is thus given by the quantity $(4\pi s \xi_n)^2$ which has been calculated (see appendix) and plotted against β for various values of n in figure 15.

The first point of interest is that the dislocation scatters more intensity into the Bragg reflexion than the surrounding regions, and should appear as a dark line on bright field images, and as a bright line on the dark field image. Secondly, the intensity peak occurs for negative values of β , i.e. the intensity scattered is larger on one side of the dislocation than on the other (in fact for $n = 2, 4$, ξ_n is zero for positive β). This of course corresponds to the differences in behaviour of the spiral on opposite sides of the dislocation and to the elementary considerations mentioned in §3.1. Thus the image of a dislocation should lie to one side

of the centre of the dislocation; the displacement of the peak from 0 in figure 15 is of the order of the width of the image. Moreover, for $n = 3$ and $n = 4$ two maxima occur— a principal one and a subsidiary one at a smaller value of $|\beta|$. Thus the image should show two peaks on the same side of the dislocation. Dislocations with multiple images have been observed occasionally, but it is not known whether the theory is sufficiently reliable to predict this fine detail. Double images are more readily explained in another way (see § 5 (c)). All the profiles rise steeply from low values of $|\beta|$ and tail off more gradually.

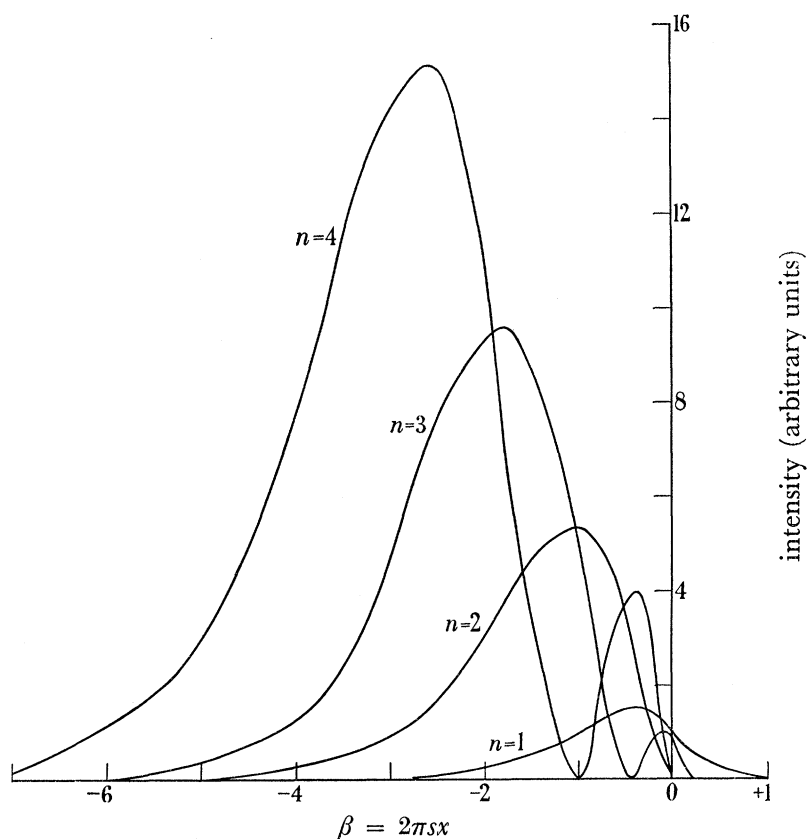


FIGURE 15. Intensity profiles of images of a screw dislocation for various values of n . $(4\pi s\xi_n)^2$ is plotted as a function of $\beta (= 2\pi s x)$. The centre of the dislocation is at $\beta = 0$. Note that the contrast lies to one side of the centre of the dislocation.

It should be noted that the intensity profiles of figure 15 do not take into account the smaller atomic scattering factors for larger values of n . This effect would tend to make the peak heights for different n more nearly equal. The curves of figure 15 can be considered as dislocation profiles for various n for the same value of s . However it will be seen (§ 4) that for any reflexion the smallest possible effective value of s (corresponding to maximum contrast, since the intensity is proportional to $(2\pi s)^{-2}$) is of the order of the reciprocal of the extinction distance t_0 . Reference to table 1 shows that t_0 increases with increasing order of reflexion. Thus, smaller effective values of s are possible for higher values of n . It is thought that the result of these two effects is to give intensity profiles under optimum contrast conditions whose peak heights are approximately independent of n , but whose width increases with increasing values of n so that the profile for $n = 4$ is about five times as wide and as far from the dislocation as that for $n = 1$.

3.4. *Extension of the theory to other dislocation configurations*(a) *Screw dislocation inclined at an angle ψ to the plane of the foil*

The dislocation AB and the column of crystal are shown in figure 16. The displacement is now $(\mathbf{b}/2\pi) \tan^{-1} y/x = (\mathbf{b}/2\pi) \tan^{-1} (z \cos \psi)/x$. The calculation of the diffracted amplitude proceeds therefore as before x now being replaced by $x/\cos \psi$. This means that the amplitude at $x \cos \psi$ will be the same as that at x for the screw parallel to the surface, i.e. the dislocation will appear narrower by a factor $\cos \psi$ (the amplitude is also less by a factor of $\cos \psi$).

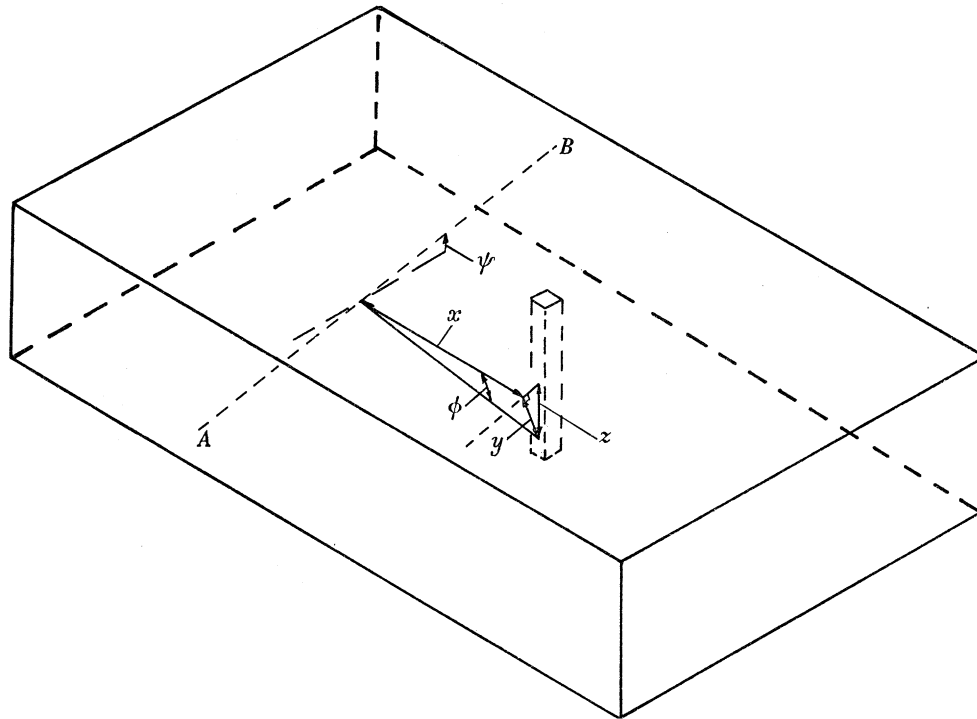


FIGURE 16. Thin foil containing a screw dislocation AB inclined to the plane of the foil. The diagram shows the definition of the distances x , y , z and the angles ϕ , ψ .

Another effect which can occur with an inclined dislocation is an oscillation in the diffracted amplitude along its length because the positions of P and P' (figure 9 (a)) near their respective circles vary for different parts of the dislocation situated at different depths (z). As before, for each z the positions of P and P' are approximately independent of x within the image. Since the origin of z is taken at the level of the dislocation, P and P' will move in such a way as to keep constant the distance PP' measured round the curve and the extremes of the motion will be when either P or P' coincides with O (corresponding to the point where the dislocation meets one or other of the foil surfaces). Figure 17 shows how this may produce large oscillations in some cases and small or no oscillations in others. The points A , B , C and A' , B' , C' correspond to these different positions of P and P' . Inspection of figure 17 reveals that in all these cases oscillations will always occur when either P or P' is near O and thus the oscillations of the diffracted amplitude which produce a dotted image should be more pronounced when the dislocation is near one of the surfaces of the foil.

(b) *Edge dislocation*

The displacements due to an edge dislocation in an infinite medium are (Read 1953):

$$R_1 = \frac{b}{2\pi} \left[\phi + \frac{\sin 2\phi}{4(1-\nu)} \right] \text{ parallel to the Burgers vector,}$$

$$R_2 = -\frac{b}{2\pi} \left[\frac{1-2\nu}{2(1-\nu)} \ln |r| + \frac{\cos 2\phi}{4(1-\nu)} \right] \text{ normal to the slip plane,}$$

$$R_3 = 0 \text{ parallel to the dislocation line.}$$

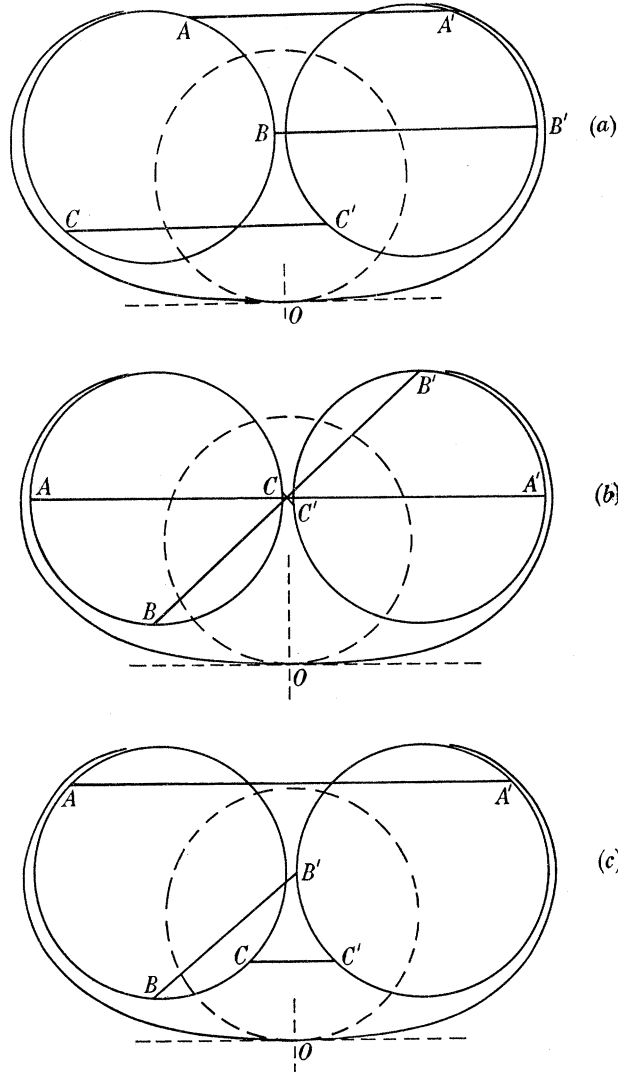


FIGURE 17. Amplitude-phase diagrams for an inclined screw dislocation illustrating how dotted images can occur. In (a), A and A' correspond to the top and bottom of the column in figure 16. For a sufficiently thick foil A and A' will lie close to the initial and final circles and are actually shown on these circles for clarity. As the column is moved along the dislocation, keeping x constant, AA' will move to BB' and CC' . The amplitudes AA' , BB' and CC' will remain approximately constant, giving a continuous dislocation image. In (b), AA' , BB' and CC' may differ considerably as the position of the column varies giving rise to a dotted image; (c) shows an intermediate case. In all cases the points AA' move in such a way that the total arc length measured along the curves between A and A' , B and B' , C and C' remains constant and equal to the crystal thickness.

ν is Poisson's ratio; ϕ is an angular co-ordinate in the plane normal to the dislocation line measured from the direction of the Burgers vector.

When the slip plane is parallel to the surface of the foil, R_1 is the displacement which affects the contrast (see §3.2).

For

$$\nu = \frac{1}{3}, \quad \alpha = 2\pi\mathbf{g} \cdot \mathbf{R}_1 = n[\phi + \frac{3}{8}\sin 2\phi] \approx n \tan^{-1}(2z/x),$$

to a reasonable approximation, where $\tan \phi = z/x$. The amplitude is the same at $2x$ and x for edge and screw dislocations for the same s . Thus the edge dislocation in this orientation will appear about twice as wide as a screw dislocation.

No calculations have been performed for the case of an edge dislocation whose Burgers vector is normal to the foil. In this case $\alpha = 2\pi\mathbf{g} \cdot \mathbf{R}_2$ and the presence of the term in $\ln|r|$ means that the amplitude-phase diagram is no longer asymptotic to a circle for large $|z|$. Two general remarks can be made however.

(1) The phase factor α for this displacement does not change sign with x . Thus any image that results will be symmetrically placed relative to the dislocation.

(2) Most of the effect should come from the $\ln|r|$ term in the phase factor, since the term in $\cos 2\phi$ changes sign twice in any column of crystal. Since the $\ln|r|$ term varies extremely slowly at large distances the image is likely to be very narrow.

3.5. Effect of divergence of the incident beam

Under microscopy conditions in the Siemens Elmiskop I electron microscope the maximum divergence of the incident beam is approximately 3×10^{-3} radians (600μ condenser aperture). This corresponds to a fractional variation in s of about $\frac{1}{6}$ for a typical reflexion and reasonable value of s . Consequently, all the dislocation image profiles should be averaged over this range of s which corresponds to a variation of approximately 60° in the angular position of a point such as P' on the final circle in figure 9(a). Of course the size of the circle also changes with s . Probably this effect would be sufficient to obscure some of the fine details that might otherwise appear on the images and it may be the explanation for the comparative rarity of dotted images. Absorption effects, if important, would also be expected to obscure fine detail except perhaps for dislocations close to the surface.

4. DISCUSSION OF THE APPLICABILITY OF THE THEORY AND ITS RELATION TO DYNAMICAL THEORY

The basic feature of the kinematical theory is the amplitude-phase diagram and it is necessary to discuss its validity and be aware of its limitation in view of the fact that dynamical effects are known to be important in electron diffraction.

For a perfect crystal the dynamical theory of electron diffraction gives the following expressions for the amplitudes transmitted (T) and diffracted (A) by a crystal of thickness t (see, for example, Whelan & Hirsch 1957*a*). The amplitude of the incident wave is taken to be t_0/π .

$$T = (t_0/\pi) \{-i \cos \pi t \bar{s} - (s/\bar{s}) \sin \pi t \bar{s}\}, \quad (9)$$

$$A = (\sin \pi t \bar{s})/(\pi \bar{s}), \quad (10)$$

where

$$\bar{s} = \sqrt{(t_0^{-2} + s^2)},$$

and t_0 is the extinction distance, equal to $(\pi V k \cos \theta)/F$; t_0 depends on the indices of the reflexion mainly through the factor F (§2.1). Since F falls off rapidly with increasing scattering angle the extinction distance increases for higher-order reflexions. Table 1 lists some typical extinction distances for face-centred cubic metals. F has been calculated using the Born approximation (Mott & Massey 1933). It is to be noted that extinction distances for low-order reflexions are about a few hundred ångströms.

TABLE 1. EXTINCTION DISTANCES (Å) OF TYPICAL METALS FOR
100 kV ELECTRONS ($\lambda = 0.037$ Å)

reflexion	111	200	220
Al	646	774	1240
Ni	258	302	468
Cu	268	308	472
Ag	250	285	403
Pt	165	188	262
Au	181	204	281

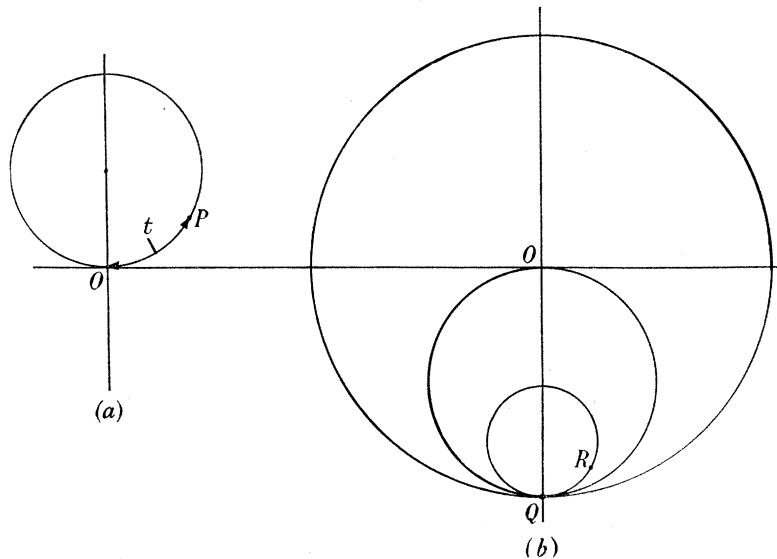


FIGURE 18. Amplitude-phase diagrams representing dynamical scattering from a perfect crystal. (a) Diffracted wave. The radius of the circle is $(2\pi\bar{s})^{-1}$. OP is the dynamical amplitude for a crystal of thickness t . (b) The transmitted wave amplitude is OR , where R lies on a circle QR of radius $t_0(\bar{s} - s)(2\pi\bar{s})^{-1}$. $OQ = t_0/\pi$ and QR is parallel to OP in (a). As the crystal thickness varies both OP and OR oscillate. When s is large compared with t_0^{-1} the circle QR in (b) is much smaller than the circle OP in (a) and approximates to a point. This is the kinematical approximation. For small s both the circles OP and QR expand to a maximum radius $t_0/2\pi$.

Equation (10) is identical with the kinematical expression for the diffracted amplitude with s replaced by \bar{s} . The minimum value of \bar{s} is t_0^{-1} .

Amplitude-phase diagrams can be constructed to represent A and T . The diagram for the diffracted wave (figure 18 (a)) is a circle of radius $(2\pi\bar{s})^{-1}$, while that for the transmitted wave is a circle of radius $t_0(\bar{s} - s) \times (2\pi\bar{s})^{-1}$ (figure 18 (b)). OP is the diffracted amplitude for a crystal of thickness t ; OR is the transmitted amplitude; OP is parallel to QR . As the crystal thickness varies both OP and OR oscillate. For s large compared with t_0^{-1} the circle QR in

figure 18 (*b*) has a much smaller radius than the circle in figure 18 (*a*), i.e. OR oscillates only very slightly from OQ . This is the region in which the kinematical approximation is justified. The circle in figure 18 (*a*) is then approximately of radius $(2\pi s)^{-1}$ as assumed in the kinematical theory. However, as $s \rightarrow 0$ the oscillations of OP and OR increase in amplitude until eventually when $s = 0$ both OP and OR describe circles of radius $t_0/2\pi$ passing through O . In this case both transmitted and diffracted amplitudes oscillate between zero and t_0/π with 90° phase difference. This corresponds to the centre of the dynamical region and illustrates the well-known phenomenon of periodic extinction of the transmitted wave. Thus for a perfect crystal the transition from the kinematical to the dynamical regions is gradual, and no well-defined limits to the applicability of kinematical theory occur. However, it is clear that amplitudes greater than t_0/π have no physical meaning on amplitude-phase diagrams, and that for a dislocated crystal dynamical effects will tend to distort the diagrams to a greater extent for smaller s , so that they are always contained by a circle of radius t_0/π .

5. COMPARISON OF THEORY WITH EXPERIMENT

The theory developed in the previous sections explains a number of features associated with images of dislocations.

5.1. *Nature, width and position of dislocation contrast*

The theory predicts that dislocations should appear as dark lines on bright field micrographs and that the contrast should be reversed in dark field. Figures 19 (*a*) and (*b*), plate 4, provide a striking example of the reversal of contrast in bright and dark field micrographs of dislocations in aluminium. The reflexion producing the contrast is (220) . Some cases have been observed where the bright and dark field images are not complementary (dislocations are dark in both), but usually then another high-order reflexion is found to be operating.

The intensity profiles of figure 15 suggest that the width Δx of a dislocation at half maximum intensity for $n = 1$ and 2 should correspond to $\Delta\beta = 2\pi s\Delta x \sim 2$, with possibly a considerably larger width for $n = 3$ and 4. The experimental evidence seems to suggest that $n = 1, 2$ occur frequently while $n = 3, 4$ occur seldom if ever. The width of a dislocation should therefore be $\Delta x \sim (\pi s)^{-1} = t'_0/\pi$. According to the kinematical theory the width should become infinite when s tends to zero. However, we have seen that dynamical conditions effectively limit s to values greater than t_0^{-1} . The maximum width of a dislocation is therefore expected to be about t_0/π or less. Using the extinction distances t_0 of table 1 it is seen that dislocations in aluminium should appear as lines about 200 to 400 Å wide or less depending on the reflexion, while other metals may have smaller maximum dislocation widths (e.g. for Ni about 80 to 150 Å). These considerations are also in general agreement with observations.

The theory predicts that the contrast peak should be to one side of the centre of the dislocation, the displacement of the peak being of the order of the dislocation width. The position of the peak depends on the factors \mathbf{g} , \mathbf{b} and \mathbf{s} ; it reverses if any of these parameters changes sign. Figure 20, plate 4, shows a typical example of peak reversal when s changes sign for dislocations in aluminium. The orientation of the normal to the foil is $[112]$ and it is thought that the dislocations lie in (111) with Burgers vectors either $\pm\frac{1}{2}[1\bar{1}0]$ or $\pm\frac{1}{2}[0\bar{1}1]$. Running across the micrograph is a bend extinction contour of the $1\bar{3}1$ reflexion (the

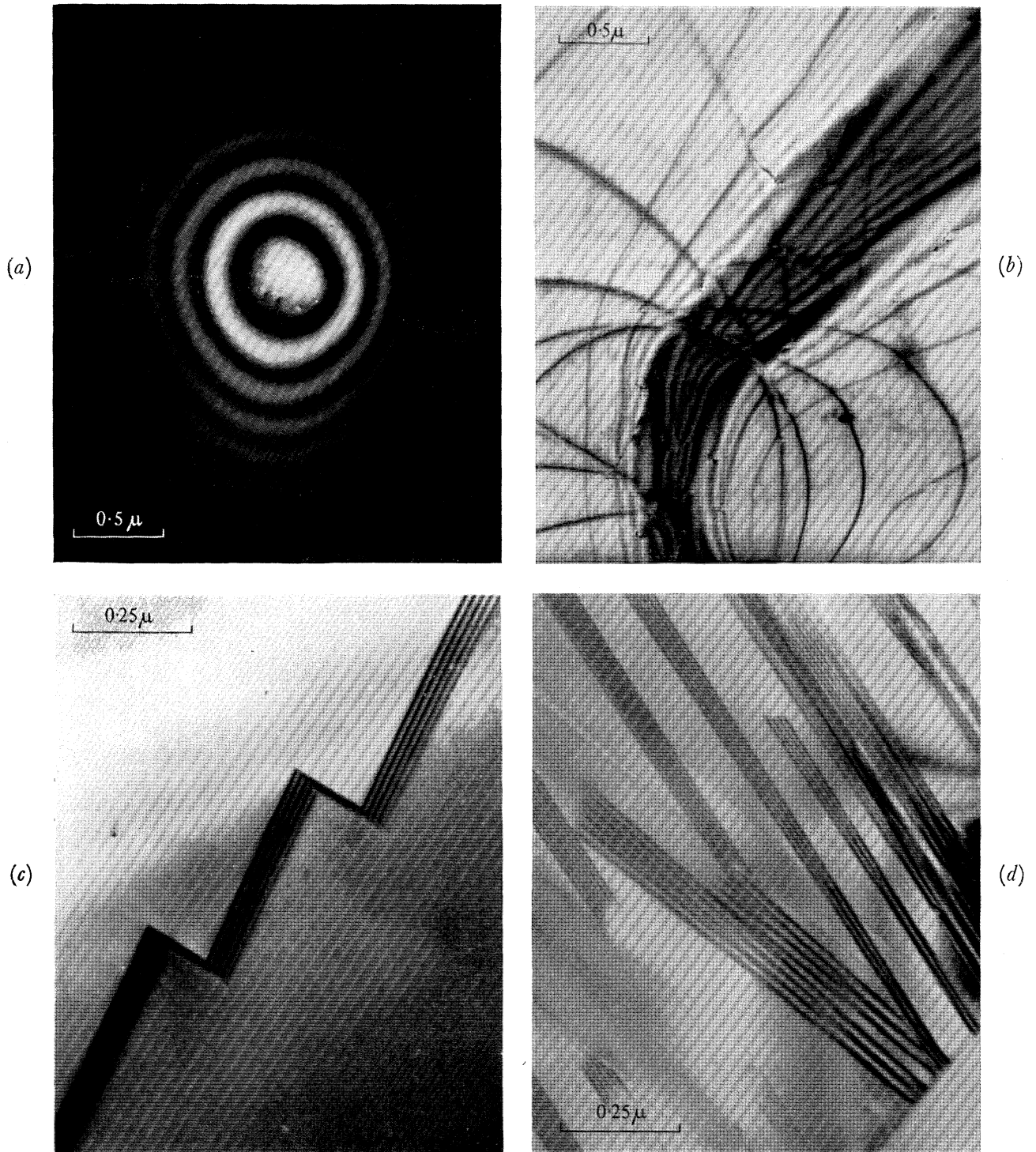


FIGURE 5. Examples of fringes in thin metal foils. (a) Thickness extinction contours in aluminium around a nearly circular depression. (Magn. $\times 30\,000$.) (b) Extinction contours in aluminium due to buckling of the foil. (Magn. $\times 30\,000$.) (c) Fringes at a twin boundary in stainless steel. (Magn. $\times 60\,000$.) (d) Fringes at stacking faults in stainless steel. (Magn. $\times 80\,000$.)

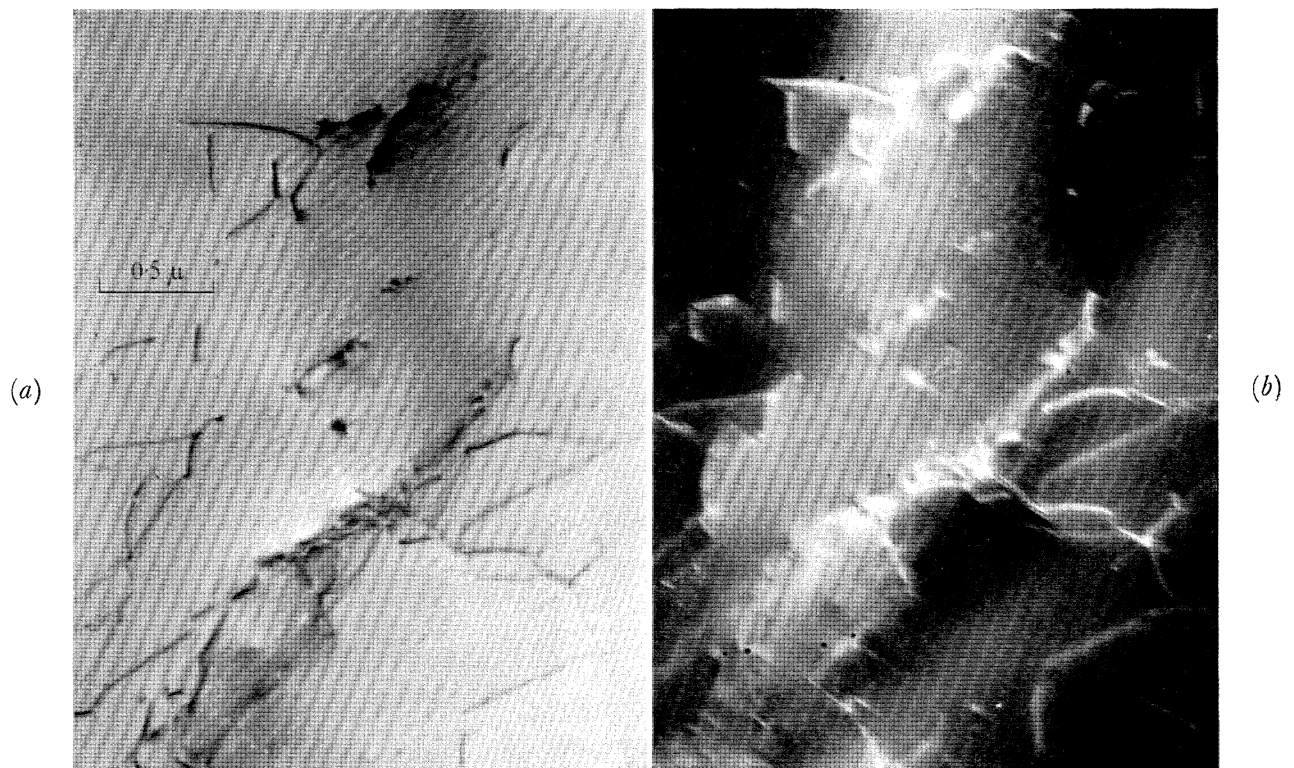


FIGURE 19. Bright field and dark field images of dislocations in aluminium. Note that the dislocations appear as light lines on the dark field image and as dark lines on the bright field image. (Magn. $\times 30\,000$.)

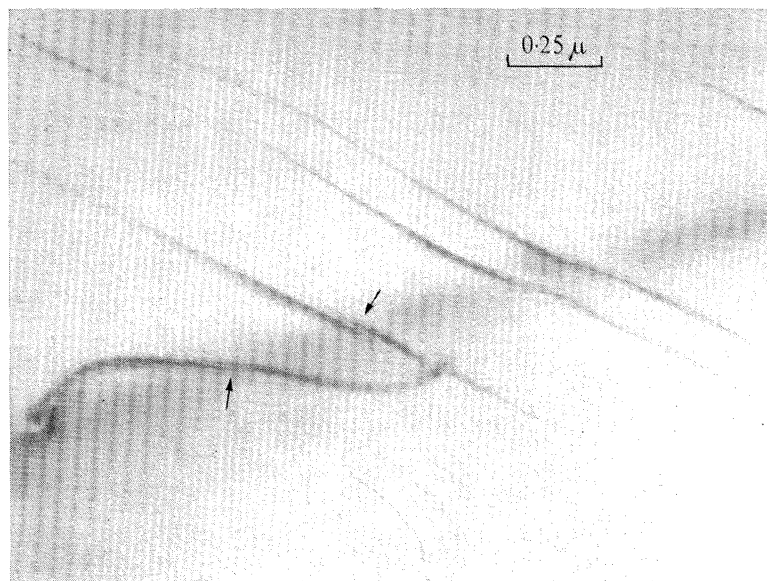


FIGURE 20. Micrograph illustrating the one-sided nature of dislocation contrast in aluminium. Note that the contrast changes from one side of the dislocation to the other where the dislocation crosses the extinction contour. Note also the rapid decrease in contrast on the side facing the dislocation and slower decrease on the other side. The width and total intensity of the image is a maximum on the edge of the extinction contour. (Magn. $\times 50\,000$.)

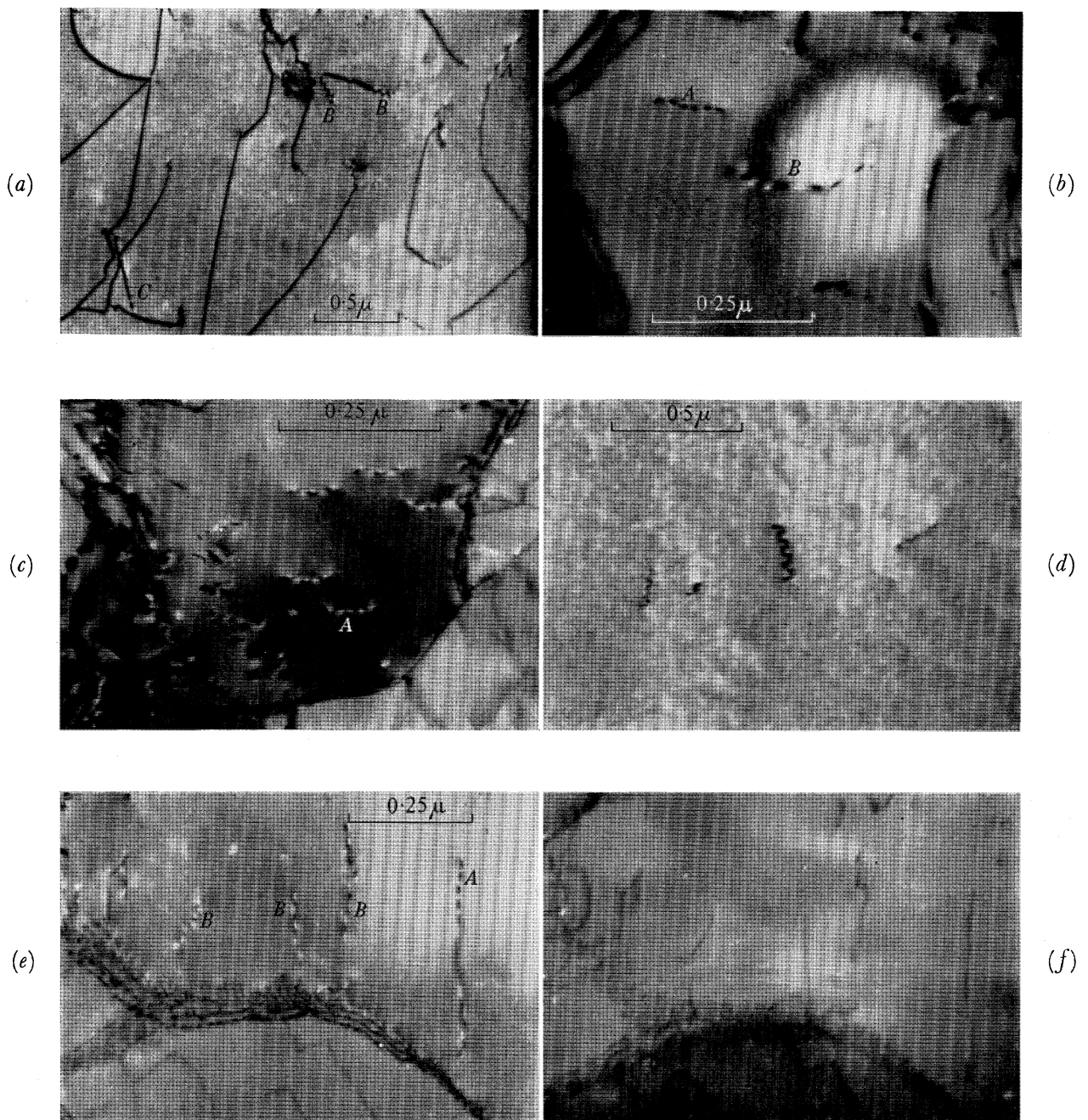


FIGURE 21. Micrographs of aluminium showing special contrast effects at dislocations. (a) *A*, alternating black-white appearance, *B*, zigzag contrast, *C*, dotted contrast. (Magn. $\times 26\,000$.) (b) *A*, dotted contrast; *B*, alternating black and white contrast. (Magn. $\times 100\,000$.) (c) Dotted, white contrast at dislocations in region of dark extinction contour. (Magn. $\times 100\,000$.) (d) Zigzag contrast. (Magn. $\times 40\,000$.) (e) *A*, dotted contrast; *B*, zigzag contrast. (Magn. $\times 75\,000$.) (f) Same area as (e) after tilting the specimen. (Magn. $\times 75\,000$.)

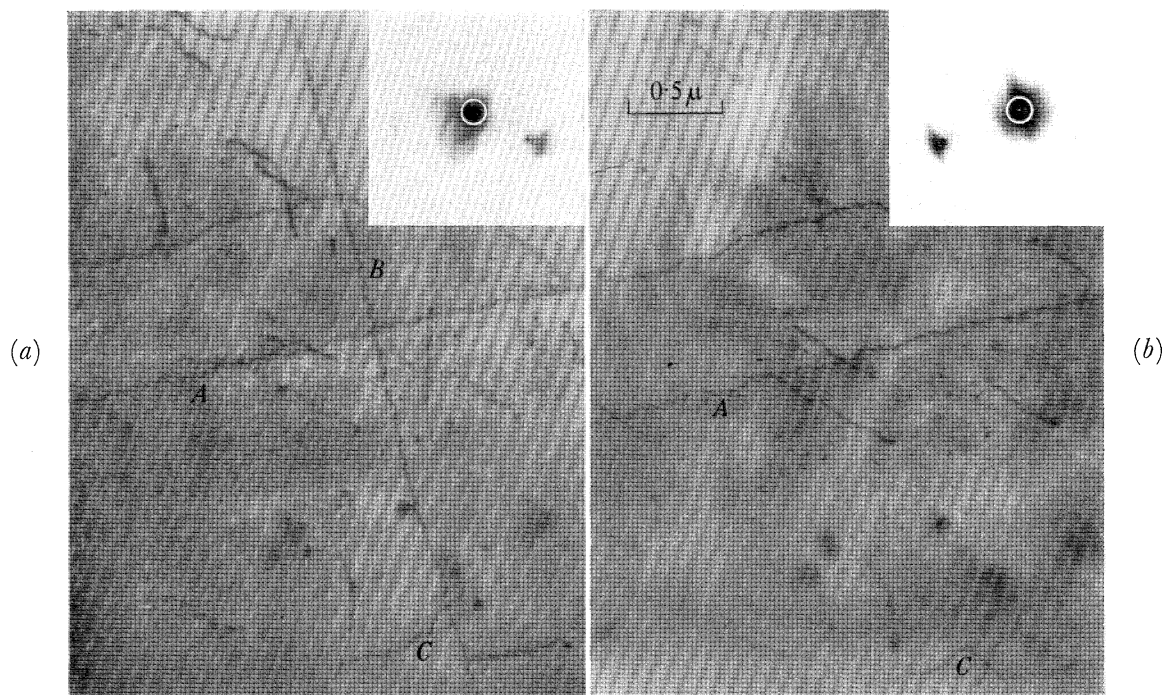


FIGURE 22. Sequence of micrographs (and diffraction patterns) of quenched aluminium + 4% copper alloy showing two helical dislocations *A* and *B*. After tilting dislocation *B* has vanished. Another dislocation has appeared at *C*. (Magn. $\times 25\,000$.)

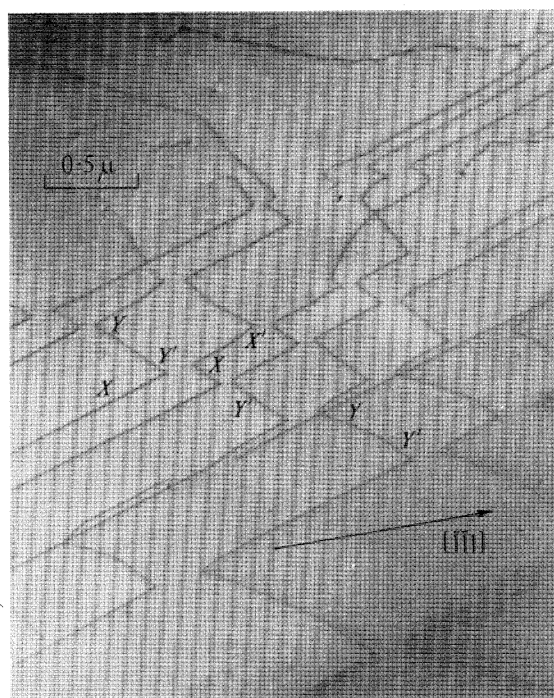


FIGURE 23. Interaction of two sets of dislocations *X* and *Y* to produce a resultant dislocation which is invisible. The normal to the foil is $[213]$. See figure 24 and text for interpretation. (Magn. $\times 25\,000$.)

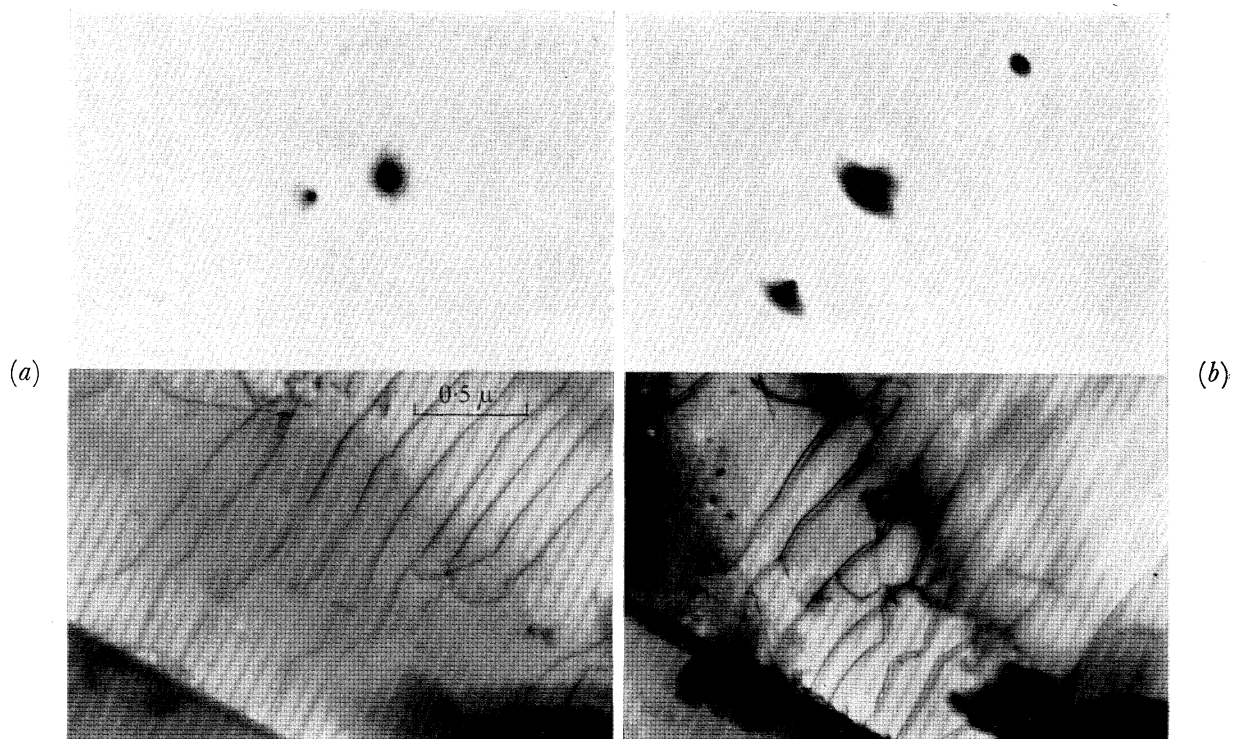


FIGURE 25. Micrographs of nickel showing (a) single images and (b) double images in the same area. Corresponding diffraction patterns are shown. See text for discussion. (Magn. $\times 30\,000$.)

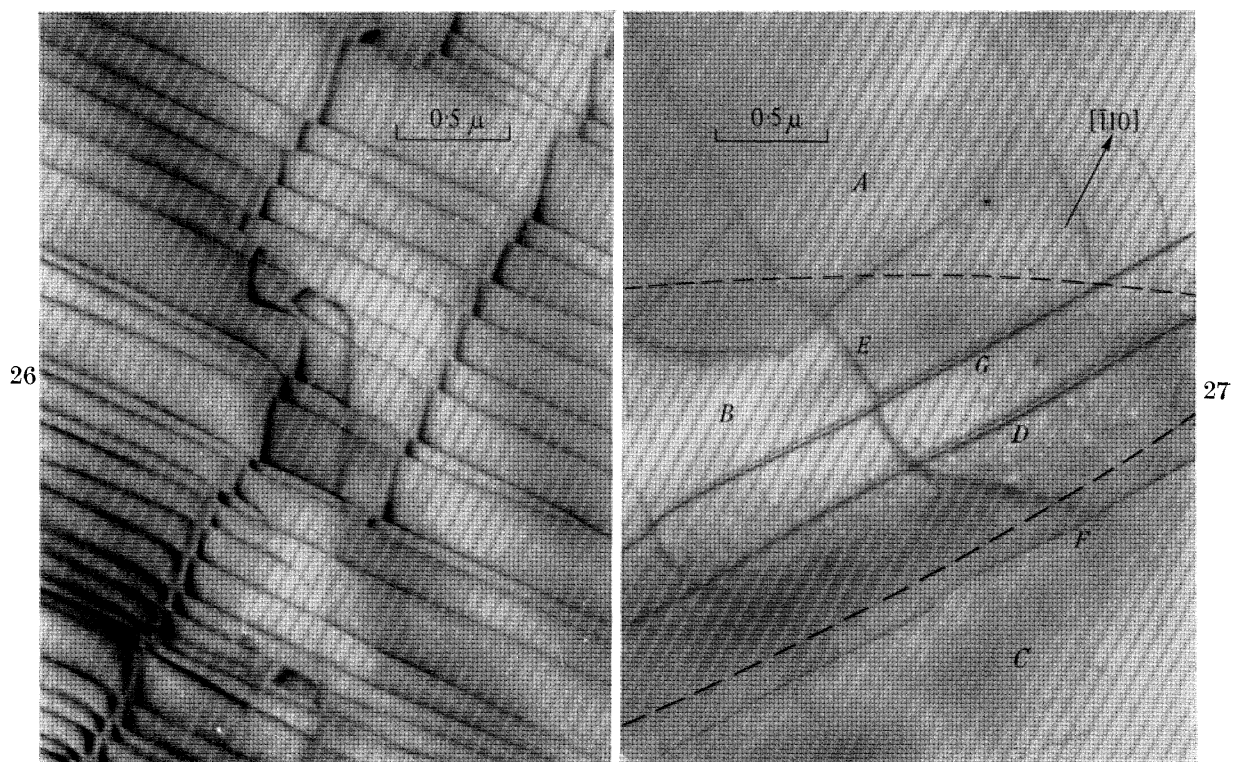


FIGURE 26. Micrograph of interacting dislocations in aluminium. Note the wide double images for one type of dislocation. See text for discussion. (Magn. $\times 30\,000$.)

FIGURE 27. Region showing double images of dislocations in aluminium. The approximate centres of high-order extinction contours are marked with broken lines. See text for discussion. (Magn. $\times 26\,000$.)

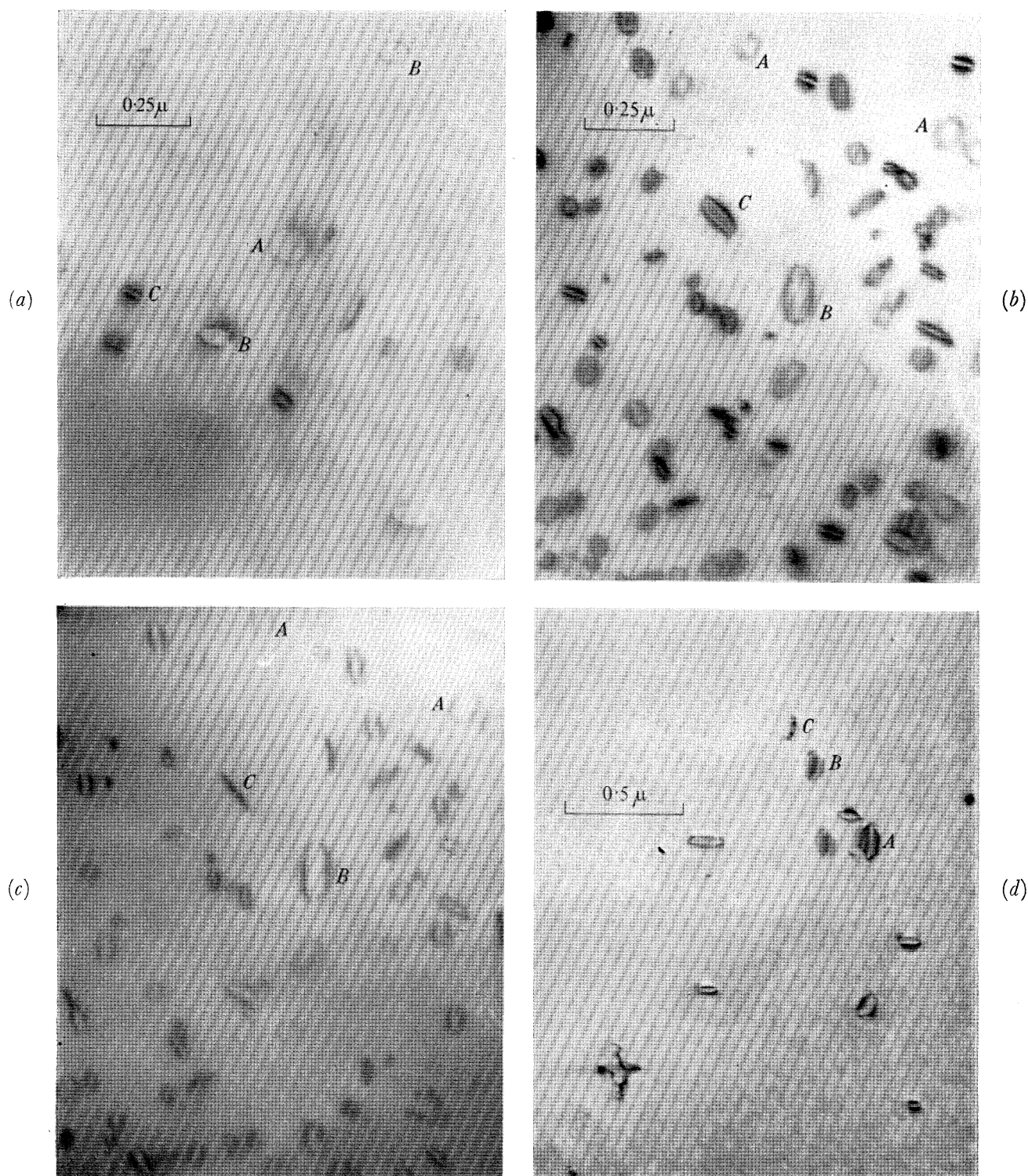


FIGURE 28. Images of dislocation loops in quenched aluminium. (a) A, hexagonal loop lying in a plane nearly parallel to the foil surface showing uniform contrast. Loops B and C are on inclined planes and the more steeply inclined parts are less visible. (Magn. $\times 65\,000$.) (b) A, dislocation with nearly uniform contrast. B, C, double images of dislocation loops. (Magn. $\times 60\,000$.) (c) Same area as (b) after tilting. (Magn. $\times 60\,000$.) (d) A, B, hexagonal loops showing double images. C, dotted appearance of a loop thought to be lying in a plane normal to that of the foil. (Magn. $\times 40\,000$.)

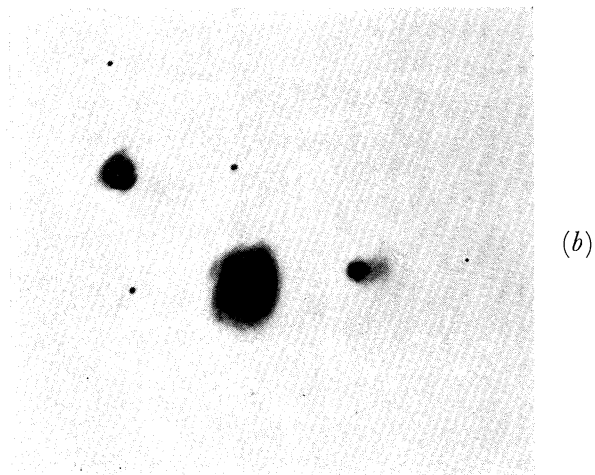
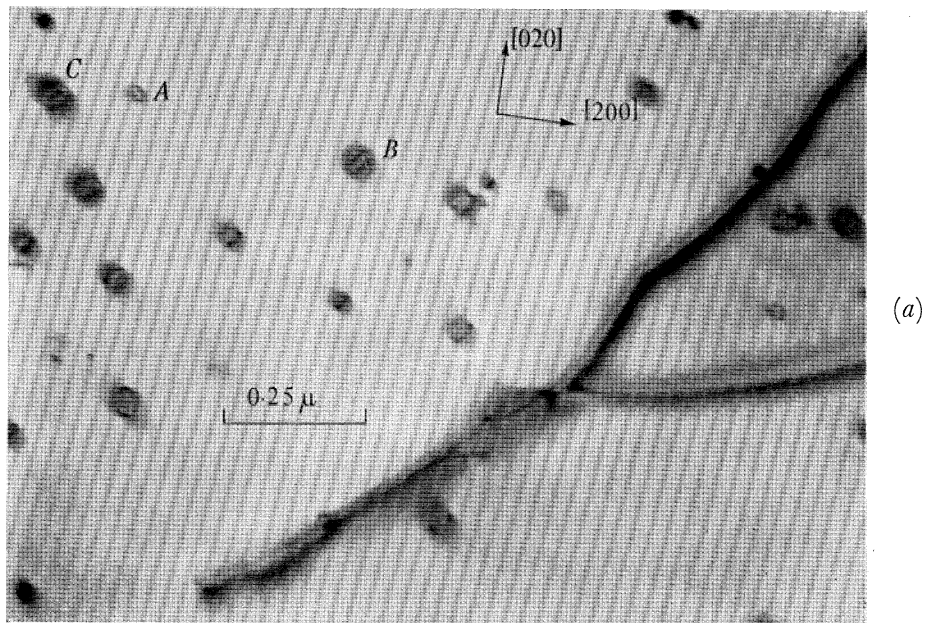


FIGURE 29. (a) Dislocation loops in quenched aluminium. Note the double images of loops at *B* and *C*. See text for discussion. (Magn. $\times 75\,000$.) (b) Selected area diffraction pattern from (a).

indices have been determined by selected area diffraction); the values of n are ± 2 for both possible Burgers vectors. At the extinction contour s changes sign and it can be clearly seen that the position of the peak also changes from one side of the dislocation to the other, e.g. at the points marked with arrows. The displacement of the peaks is of the same order as their width, as expected. It will also be noted that the contrast at these dislocations is a maximum just outside the centre of the contour, i.e. in the region where the kinematical theory is expected to be valid. The contrast falls very steeply on the side facing the dislocation and fades out gradually on the other side, just as expected from the profiles of figure 15. The contrast and width of the dislocation also decrease very rapidly with distance from the contour, i.e. with increasing $|s|$. This behaviour of dislocations at bend contours has been observed a number of times. All these facts are in excellent agreement with the predictions of the theory.

A number of more complicated image effects can be seen in figure 21 (*a*) to (*f*), plate 5. In figure 21 (*a*) the dislocations show an alternating black-white appearance (*A*), zigzag appearance (*B*), and dotted appearance (*C*). Figure 21 (*b*) also shows a dislocation *A* running through the foil which appears as a series of dark dots along its whole length. Close to *B* another dislocation is seen in the region of an extinction contour; the change over to the alternating black-white appearance is evident at this dislocation. The theory provides a ready qualitative explanation of the dark dotted contrast (§3.4) and also for the frequent occurrence of these phenomena at those parts of inclined dislocations near the foil surface (e.g. figure 21 (*a*) at *C*). Sometimes dislocations are observed which appear lighter than their surroundings on bright field micrographs. An example of this is visible in figure 21 (*c*) where dislocations appear as a series of white dots at *A*. In these cases the surrounding regions of the foil are usually diffracting strongly. The white dotted appearance is thought to be a dynamical effect not predicted by the present theory. The zigzag effects are also not easily explained on the present theory. Figure 21 (*a*) at *A* and *B* shows an effect which is observed frequently, the contrast is observed to zigzag as the dislocation approaches the top and bottom surfaces of the foil. Sometimes the contrast zigzags along the whole length of the dislocation. Figure 21 (*d*) shows particularly good examples of zigzag dislocations, which might at first sight be taken to be helical dislocations. However, all these zigzag and dotted contrast effects are extremely sensitive to orientation; by tilting the specimen slightly it is possible to alter the contrast to a continuous dark line. This is shown quite clearly in figure 21 (*e*) and (*f*). Figure 21 (*e*) shows dotted contrast at *A* and zigzag contrast at *B*. Figure 21 (*f*) shows the same area after tilting the specimen slightly; the dislocations now appear as continuous dark lines. It is thought that the detailed explanation of all these effects will require a treatment by dynamical theory (possibly including absorption); the effects are presumably connected with the depth oscillations of the crystal wave fields in the dynamical region. They are mentioned here to emphasize that such effects are not to be interpreted in terms of any structural features of the dislocations.

5.2. Invisible dislocations and determination of Burgers vectors

The case $n = 0$, i.e. $\alpha = 0$, for a screw dislocation corresponds to \mathbf{g} and \mathbf{b} being mutually perpendicular and is of considerable interest. In this case the displacements of atoms are parallel to the reflecting planes and no contrast is produced. Similar considerations are

expected to hold approximately for an edge dislocation and in general for a mixed dislocation. There is considerable experimental evidence that not all dislocations may be visible on transmission micrographs (Bradley & Phillips 1957). The same contrast mechanism is expected to apply to the new techniques for revealing dislocations by transmission of X-rays (Lang 1958) and probably also to the corresponding X-ray reflexion case (Newkirk 1958; Bonse & Kappler 1958). In the former case (Newkirk 1958) the above condition for invisibility appears to have been discovered experimentally.

Figure 22 (*a*) and (*b*), plate 6, show a striking example of this effect in Al+4% Cu alloy quenched from 440 °C. This material contains helical dislocations formed from screw dislocations by vacancy climb (Thomas & Whelan 1959). The axes of the helices are parallel to the Burgers vector. The normal to the foil in figure 22 is near [001] and the helical dislocations *A* and *B* have Burgers vectors $\frac{1}{2}[\bar{1}10]$ and $\frac{1}{2}[110]$, respectively. Selected area diffraction patterns (corrected for rotation) are included with the micrographs. In figure 22 (*a*) both helices have a non-vanishing value of $\mathbf{g}\cdot\mathbf{b}$ ($=1$) for the operating 020 reflexion, and both are visible. In figure 22 (*b*) the specimen has been tilted so that $2\bar{2}0$ is the operating reflexion. \mathbf{g} is now perpendicular to *B*, and this dislocation therefore vanishes. *A* now has $\mathbf{g}\cdot\mathbf{b} = 2$ and the characteristic rapid decrease of the contrast at one side is apparent. Other dislocations have also vanished, while another has appeared at *C* showing that a feature which might otherwise have been interpreted as a pinning point is a triple node. Since a helical dislocation is mainly of edge character the theory is seen to be applicable to edges. Moreover, the vanishing of the helix *B* in figure 22 (*b*) indicates that the displacement normal to the slip plane of an edge dislocation has little effect on the contrast in agreement with the predictions made in §3.4.

Figure 23, plate 6, shows a rather interesting case of invisible dislocations formed by an interaction process. The normal to the foil is close to [213] and the slip planes involved are $(\bar{1}11)$ (dislocations of type *X*) and $(1\bar{1}1)$ (dislocations of type *Y*). The dislocations *X* lie on parallel but displaced $(\bar{1}11)$ slip planes which cut through the foil at an angle; similar considerations hold for dislocations *Y*. The directions of *X* and *Y* are approximately parallel to the traces of the $(\bar{1}11)$ and $(1\bar{1}1)$ planes on the foil surface suggesting that these dislocations lie in a direction in their slip planes approximately parallel to the surface of the foil. A detailed study of this micrograph shows that an interaction has occurred at the intersection points of dislocations of types *X* and *Y*, and that the resultant dislocations (joining the sharp bends) are invisible for contrast reasons. The possibility that the interaction might be an annihilation (Whelan 1959) is ruled out by the fact that very weak contrast is visible on the original photographic plate at some of the resultant dislocations, and by the fact that such an angular dislocation would not be stable in this configuration. The details visible at several of the interactions can be explained satisfactorily in terms of the diagram of figure 24 which shows the arrangement in terms of Thompson's reference tetrahedron (Thompson 1953). Dislocation *X* lies on the plane *ABD* ($(\bar{1}11)$) nearly parallel to *BD* with Burgers vector *BD* ($\frac{1}{2}[01\bar{1}]$), while dislocation *Y* lies on the plane *ACD* ($(1\bar{1}1)$) nearly parallel to *CD* with Burgers vector *DC* ($\frac{1}{2}[\bar{1}01]$). *X* and *Y* are nearly in the screw orientation so that at the intersection point it will be energetically favourable for them to cross-slip to the plane *BCD* ((111)) to form segments *X'* and *Y'* which interact to form a resultant dislocation with Burgers vector $BD + DC = BC$ ($\frac{1}{2}[\bar{1}10]$). The segments of dislocation *X*–*X'* and *Y*–*Y'* therefore lie on

different planes and the points where they bend from one slip plane to the other give rise to the slight kinks in the dislocations visible on the micrograph (e.g. X , X' and Y , Y').

The Burgers vectors of all the dislocations in figure 23 are therefore determined purely by geometrical considerations. In particular, the Burgers vector of the resultant dislocation is $\frac{1}{2}[\bar{1}10]$ and a selected area diffraction pattern showed that the $\bar{1}\bar{1}1$ reflexion is producing the contrast. This is in agreement with the contrast theory since $n = \mathbf{g} \cdot \mathbf{b}$ is zero for this

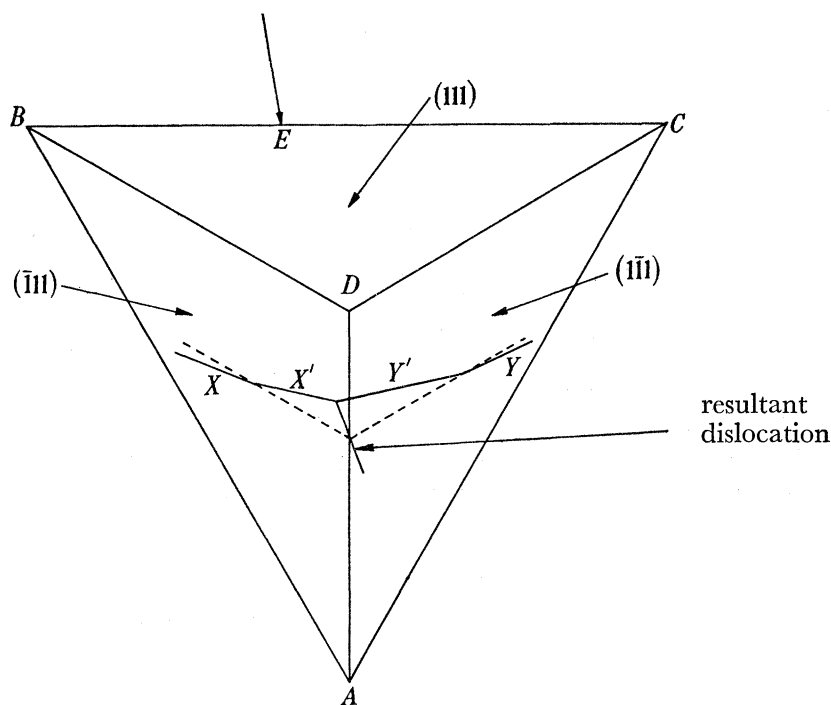


FIGURE 24. Interpretation of the interactions of figure 23. The diagram shows Thompson's tetrahedron representing the slip systems. The dislocation segment X lies in $(\bar{1}11)$ with Burgers vector BD ; Y lies in $(1\bar{1}1)$ with Burgers vector DC , while X' and Y' and the resultant dislocation lie in (111) . The direction of observation in figure 23 is roughly along EA where E lies on BC . At most of the nodes in figure 23 usually one or other of the segments X' and Y' predominates in length. Also at some interactions all of Y appears to have cross-slipped to Y' . The resultant dislocation is approximately a pure edge dislocation and is invisible in the micrograph of figure 23 because its Burgers vector is perpendicular to the reciprocal lattice vector of the Bragg reflexion producing the contrast.

Burgers vector and reflexion and the resultant dislocation is expected to be invisible. In principle therefore it should be possible to determine the Burgers vector of any dislocation by examining the contrast in several reflexions and by finding reflexions for which the contrast vanishes. However, the facilities for tilting the specimen in the electron microscope are at present not adequate to make this a practical possibility.

It should also be mentioned that the very weak contrast visible at some of the resultant dislocations in figure 23 on the original plate is probably due to the fact that these are very nearly pure edge dislocations orientated so that the displacement R_2 of § 3.4 is effective. This displacement will be approximately in the $[111]$ direction, and gives a non-vanishing phase factor with the $\bar{1}\bar{1}1$ reflexion. Thus the experimental observations are in agreement with

the conclusions of §3.4 that the contrast due to this displacement is expected to be narrow and weak. It should also be possible to distinguish between screw and edge dislocations in certain orientations by use of this effect.

5.3. *Double images of dislocations*

Double images of dislocations are frequently observed and occur when two sets of reflecting planes which produce contrast on opposite sides of the dislocation are operating simultaneously. If the parameters \mathbf{g} and s describing the two reflexions are labelled with suffixes 1 and 2 we must have either $\mathbf{g}_1 \cdot \mathbf{b}$ and $\mathbf{g}_2 \cdot \mathbf{b}$ of opposite sign or s_1 and s_2 of opposite sign. The effect is illustrated in figure 25(a) and (b), plate 7, for dislocations in nickel. In figure 25(a) the images of the dislocations are single and the diffraction pattern from a selected area shows only one strong diffracted beam. The specimen was then tilted until double images appeared (figure 25(b)). Selected area diffraction then gave the pattern shown with two strong diffracted beams. These observations are insufficient to determine the Burgers vector of the dislocations, but all the possible values for \mathbf{b} have $\mathbf{g}_1 \cdot \mathbf{b}$ and $\mathbf{g}_2 \cdot \mathbf{b}$ opposite in sign, so that s_1 and s_2 must have the same sign. This example shows again that the displacement of the image is of the same order as its width.

Another example of double images appears in figure 26, plate 7, where two sets of dislocations on different slip planes have intersected and interacted to produce short segments of resultant dislocation. One set of dislocations appears single (either because the two images fall on the same side of the dislocation or because the Burgers vector lies in one set of reflecting planes). The other dislocations have a different Burgers vector and appear as widely separated double images possibly corresponding to $n = 3$. These dislocation images also show clearly the expected gradual fading of the contrast on the side away from the dislocation.

Figure 27, plate 7, shows a situation in aluminium where both sets of intersecting dislocations appear double. In this micrograph two extinction contours $A-B$ and $B-C$ (marked by broken lines) are visible. These correspond to the $\bar{3}11$ and $2\bar{2}0$ reflexions, respectively. The extinction contours divide the micrograph into three regions A , B and C . Consideration of the reflecting sphere and the two reflexions shows that in regions A and C , s_1 and s_2 for the two reflexions have opposite sign, while in region B , s_1 and s_2 have the same sign. The electron beam passes in the $[11\bar{2}]$ direction and examination of slip traces in the area showed that the normal to the foil was some 6° away from this in the direction of $[31\bar{3}]$. Consideration of the possible Burgers vectors for the dislocations G , D and F (lying in a (111) slip plane) and E (lying in a $(\bar{1}11)$ plane) showed that the Burgers vector of E must be $\frac{1}{2}[101]$ and that of G , D and F either $\frac{1}{2}[\bar{1}\bar{1}0]$ or $\frac{1}{2}[10\bar{1}]$. Both these possibilities give opposite values of $\mathbf{g} \cdot \mathbf{b}$ for each Burgers vector in the two reflexions which agrees with the fact that s_1 and s_2 have the same sign in the region B where the dislocations appear double. The second of the two possibilities, however, in which the two Burgers vectors are mutually perpendicular provides the more satisfactory explanation of the absence of any attraction or repulsion at the points of intersection. Note the characteristic image of F with a sharp rise in contrast on one side and a gradual decrease on the other. The dislocation G becomes single after crossing the $\bar{3}11$ contour because the image due to this reflexion crosses to the other side of the dislocation. While the above observations show that double dislocations occur only

if two or more reflexions are excited simultaneously, Phillips (private communication) has been able to confirm by dark field photographs that each image arises from a different reflexion.

5.4. Images of dislocation loops

Figure 28 (*a*) to (*d*), plate 8, show some of the features of the images of dislocation loops observed in quenched aluminium (Hirsch *et al.* 1958). This type of loop lies on a $\{111\}$ plane and the Burgers vector is not in the plane of the loop. Loops such as those at *A* in figure 28 (*a*) to (*c*) lie on planes nearly parallel to the surfaces of the foil and appear round or hexagonal with uniform contrast. Many of the other loops are characterized by pronounced variation in contrast so that they appear as two arcs. These loops are lying on planes more steeply inclined to the foil; the two arcs correspond to the parts of the loop approximately parallel to the surface while the steeply inclined parts of the loops appear faint and narrow or are altogether invisible, in agreement with the predictions of §3.4 (e.g. at *B* in figure 28 (*a*) and (*c*)).

The Burgers vectors of opposite sides of a loop are of opposite sign, provided the positive sense of the dislocation is taken in the same direction on both sides. The image will therefore lie either completely inside or completely outside the dislocation loop. If two reflexions are operating which give double images, one image lies outside the loop and the other inside. Figure 28 (*b*) and (*c*) show the same area in slightly different orientation. Double images are clearly visible in figure 28 (*b*); the appearance of some of these images, for example at *B*, must not be confused with that expected from loops containing stacking faults. In figure 28 (*c*) only single images are visible. In the case of these double images the actual dislocation loop lies between the two images. If only one image occurs as in figure 28 (*c*), the images of opposite sides of the loop may actually coincide giving the appearance of a single line, such as at *C* in figure 28 (*c*). Comparison with the double image of the same loop on figure 28 (*b*) shows that the single line indeed represents a fairly steeply inclined loop. Figure 28 (*d*) shows further contrast effects observed at hexagonal-shaped loops in aluminium. A dark region is observed inside the hexagonal loop at *B* while the loop at *A* appears to have interference fringes, which might at first sight be attributed to a hexagonal disk of stacking fault contained by a Frank sessile dislocation. However, a detailed study of this contrast effect suggests that the correct explanation depends on double images as outlined above. Two reflexions are operating producing contrast both inside and outside the loop: the contrast inside the loops *A* and *B* in figure 28 (*d*) gives the appearance of fringes. The other loops visible in figure 28 (*d*) show no extra contrast. These loops are on different $\{111\}$ planes with different Burgers vectors, so that the dislocation contrast is on the same side of the loop for both reflexions.

Other more complicated contrast effects have also been observed at loops, e.g. at *C* in figure 28 (*d*). It is thought that these effects are produced by hexagonal loops on planes almost parallel to the line of sight with one segment of the loops nearly parallel to the foil surface. The double dots at the ends of the line of contrast may be due to the more steeply inclined parts of the hexagonal loop. This interpretation is, however, tentative.

The appearance of the loops and the type of reflexion operating can be used to attempt to determine the Burgers vector. Figure 29 (*a*), plate 9, is a micrograph showing double images; figure 29 (*b*) is the associated diffraction pattern showing strong 200 and $\bar{2}20$

reflexions. The orientation of the normal to the foil is approximately $[001]$. The loops at A appear single and their elongation suggests that they lie on (111) or $(1\bar{1}\bar{1})$ planes. The double image loops (e.g. at B), however, lie on $(\bar{1}11)$ or $(1\bar{1}\bar{1})$ planes. Examination of the product $\mathbf{g} \cdot \mathbf{b}$ for various Burgers vectors shows that for the single images \mathbf{b} has the possible values $\frac{1}{2}[110]$, $\frac{1}{2}[01\bar{1}]$ and $\frac{1}{2}[011]$. For those with double images \mathbf{b} has the possible values $\frac{1}{2}[\bar{1}10]$, $\frac{1}{2}[\bar{1}01]$ and $\frac{1}{2}[101]$. The first of these values is thought to be most likely as it is the only one which gives rise to $n = 2$ for one of the reflexions, all other values giving ± 1 . Such a different value of n would explain the rather different nature of the two images, i.e. one of the images is much wider as at C . All the possibilities for the double loops give values of $\mathbf{g} \cdot \mathbf{b}$ which are of opposite sign for the two reflexions. Therefore s must have the same sign for both reflexions. This has been confirmed directly from the position of the Kikuchi lines for the two reflexions. (The Kikuchi lines are not visible on figure 29 (b).) The double images of the nearby dislocation lines are also apparent.

5.5. *The interpretation of X-ray topographs*

Lang (1958) has recently developed a new technique for revealing dislocations by transmission X-ray diffraction. The method is the X-ray analogue of the dark field technique in electron microscopy. Lang reports that with $\text{AgK}\alpha$ radiation and a crystal of silicon, dislocations are observed as regions of increased diffracting power about 20μ wide. In this case the divergence of the X-ray beam at the specimen ($\sim 2'$ of arc, Lang, private communication) is much greater than the angular range of reflexion of the crystal on dynamical theory ($\sim 1/25'$). Thus an effect averaged over s should be observed, but the same considerations as in the electron case should apply. However, on averaging over s it is possible that the resultant contrast will be in the form of a single peak at the centre of the dislocation. The same conditions for visibility should apply. The X-ray extinction distances t_0 for the 111 and 220 reflexions in silicon are 55 and 46μ , respectively. t_0/π is therefore a good measure of the observed dislocation width in this case too.

Newkirk (1958) has used a reflexion X-ray technique for revealing dislocations in Fe + Si alloys and LiF crystals. The method is essentially an improvement of the Berg-Barrett technique. Although the theory of this paper applies strictly to the transmission technique only, it appears to explain qualitatively Newkirk's results also. Thus with $\text{CrK}\alpha$ radiation ($\lambda = 2.29 \text{ \AA}$), dislocations near the surface of a LiF crystal are visible as regions of enhanced diffracting power a few microns wide (Newkirk, private communication). The extinction distances for the 220 and 200 reflexions of LiF with $\text{CrK}\alpha$ radiation are $\sim 9 \mu$. This is smaller than the extinction distances in Lang's experiments. Again t_0/π is seen to be good measure of the dislocation width. Newkirk (private communication) has also studied the dislocation contrast as a function of the indices of the reflexion. The results also agree well with the predictions of the present theory concerning the variation of contrast with $n = \mathbf{g} \cdot \mathbf{b}$. Thus for different reflexions and Burgers vectors the intensity of the image seems to depend only on n , and increases with increasing n . Analysis of the photographs shows that for $n = 0$ the dislocations are invisible, for $n = 1$ and 2 the contrast is intermediate and strong, respectively. The theory (see §3.3) predicts that for optimum contrast conditions the width of the image increases with increasing n . Because of the large divergence of the X-ray beam the resultant image consists of a set of overlapping images corresponding to a range of values of s , and the

total intensity of this resultant image is expected to increase with increasing width of the dislocation profile and therefore with increasing n , as observed.

It may be noted here that Bonse (1958) has attempted to explain the contrast effects observed with X-rays by estimating the effect of strain and lattice curvature due to dislocations on the width of the reflexions. Such a theory, in which the phase relation between neighbouring diffracting elements is ignored, can at best only lead to very qualitative conclusions.

6. CONCLUSION

The kinematical theory of contrast of electron microscope images of dislocations developed in this paper explains many of the characteristic features of the observed images, such as the orientation dependence of the contrast, the reversal of contrast on bright field and dark field images, the fact that dislocations are generally dark on bright field images, the position and width of the images, the general nature of the profile, the occurrence of dotted dislocations, the invisibility of some dislocations, the dependence of contrast on the inclination of the dislocation, and the occurrence of double images. The main idea of the theory is that the contrast is essentially phase contrast, the phase variations arising from displacements of atoms near the defect. It should be possible to apply the same theory to explain other contrast effects such as the trails left behind by moving dislocations (Hirsch *et al.* 1956), or the contrast near G.P. zones in aluminium+copper alloys (Nicholson & Nutting 1958), provided the nature of the strain field near the defect is known. The theory also accounts satisfactorily for the nature and width of the dislocation images obtained with X-rays, for example, using the techniques of Lang (1958) or Newkirk (1958).

The theory does not, however, explain the 'white' dislocations which have been observed occasionally, or the characteristic black-white or zigzag appearance which is observed more frequently. Both these effects are thought to find their explanation in a full dynamical treatment of the wave propagation in the crystal. There is also some reason to believe that in thicker foils ($t \gtrsim 1000 \text{ \AA}$) absorption processes may play some part in the image formation. It is found that in thick regions the bend extinction contours (corresponding to small deviations from the Bragg angle) widen into broad dark bands in which the transmitted and diffracted beams are heavily absorbed. On either side of these bands the foil is particularly transparent and the dislocations are clearly visible. In these regions the absorption appears to be anomalously low; thus dislocations have been seen quite clearly in such areas in foils of aluminium+4% copper alloy about 7500 \AA thick (Thomas & Whelan 1959). This anomalous transmission may be analogous to the Borrmann (1941, 1950) effect observed with X-rays and part of the contrast in the image of a dislocation may be due to enhanced absorption near the dislocation. These observations suggest that a full treatment of the dynamical theory including absorption for a dislocated crystal may be required to explain all the details of the observed contrast effects. It might be noted here that while the contrast at dislocations in the X-ray experiments of Lang (1958) can be explained on the basis of the kinematical theory, that observed by Borrmann, Hartwig & Irmeler (1958) is also likely to be due to a locally enhanced absorption effect. Most of the evidence presented here has referred to aluminium, for which absorption effects are relatively unimportant even in thicker areas of this material. However, the same contrast effects have also been observed

with suitable specimens of other metals, e.g. Cu, Ni, Au, Fe, α -brass, stainless steel, so that the theory is applicable to many metals.

For most practical purposes, however, particularly for transmission electron microscopy, the kinematical theory will probably be sufficient. Its most important application will be in the determination of the Burgers vectors of dislocations. The most satisfactory method for this purpose would be to change the orientation of the specimen until the image disappears; the indices of the operating reflexion are then obtained from the diffraction pattern and \mathbf{b} is derived from the criterion $\mathbf{g} \cdot \mathbf{b} = 0$. Should there still be some ambiguity this method could be repeated for another reflexion. In order to carry out such experiments satisfactorily electron microscopes must be provided with goniometer stages which allow the specimen to be rotated several degrees about two directions at right angles. Even without such equipment it may be possible to determine \mathbf{b} in many cases by using the existing stereofacilities for tilting the specimens about one axis, and observing the nature of the contrast in several reflexions. Thus it should be possible to determine the value of $\mathbf{g} \cdot \mathbf{b}$ from the width of the dislocation images under conditions of optimum contrast; a number of such determinations taken in conjunction with any other information, for example, on the slip plane of the dislocation, should enable \mathbf{b} to be found. So far, however, no systematic experiments have been carried out to test how these methods can be applied in practice.

The theory can also be useful in other ways; for example, from the variation of the contrast around a dislocation loop, its plane can be determined. And finally the existence of complicated effects such as dotted dislocations or double images shows that care must be taken in interpreting similar contrast effects in terms of segregation or precipitation phenomena.

We are indebted to Professor N. F. Mott, F.R.S., and to Dr W. H. Taylor for their interest and encouragement during the course of this work. Mention should be made of helpful discussions with Dr D. W. Pashley and also with Dr A. Lang and Dr J. B. Newkirk, both of whom showed us unpublished work. Thanks are due to Dr G. Thomas for supplying the specimen from which the micrographs in figure 22 were taken and to Mr J. Silcox for supplying figures 28 and 29. Acknowledgments for financial support are due to Trinity College, Cambridge, for a Research Studentship (A. H.), and to D.S.I.R. and Gonville and Caius College, Cambridge, for Research Fellowships (M. J. W.).

APPENDIX. CALCULATION OF THE CO-ORDINATES ξ_n AND η_n

Consider the integral

$$A = \int_0^\infty \exp(\pm in\phi + 2\pi isz) dz, \quad (\text{A } 1)$$

where $\phi = \tan^{-1}(z/|x|)$ is defined in figure 8. The positive and negative signs are taken for x positive and negative, respectively. The co-ordinates ξ_n and η_n of the centre of the final circle represent the point in the complex plane about which the integral (A 1) oscillates.

Integrate (A 1) by parts and extract the part which does not oscillate at the upper limit:

$$\xi_n + i\eta_n = \frac{1}{2\pi s} \left[i \mp n \int_0^{\frac{1}{2}\pi} \exp(\pm in\phi + 2\pi isz) d\phi \right]. \quad (\text{A } 2)$$

Put $\tan \phi = u$, then $z = xu$ for positive x and $z = |x|u$ for negative x . Without loss of generality we may take s positive so that $\beta = 2\pi s x$ is positive for positive x and negative for negative x . The integral in (A 2) may then be transformed to

$$\mp n \int_0^\infty \exp(i|\beta|u) \frac{(1 \pm iu)^n}{(1+u^2)^{\frac{1}{2}(n+2)}} du. \quad (\text{A } 3)$$

(A 3) can be written as

$$\mp n \left(1 \pm \frac{d}{d|\beta|}\right)^n \int_0^\infty \frac{\exp(i|\beta|u)}{(1+u^2)^{\frac{1}{2}(n+2)}} du. \quad (\text{A } 4)$$

Thus from (A 2)

$$\xi_n = \mp \frac{n}{2\pi s} \left(1 \pm \frac{d}{d|\beta|}\right)^n \int_0^\infty \frac{\cos|\beta|u}{(1+u^2)^{\frac{1}{2}(n+2)}} du, \quad (\text{A } 5)$$

$$\eta_n = \frac{1}{2\pi s} \mp \frac{n}{2\pi s} \left(1 \pm \frac{d}{d|\beta|}\right)^n \int_0^\infty \frac{\sin|\beta|u}{(1+u^2)^{\frac{1}{2}(n+2)}} du. \quad (\text{A } 6)$$

ξ_n can be evaluated in terms of modified Bessel functions of the second kind. Watson (1922) gives a formula for the integral in (A 5) which leads to the following expression for ξ_n .

$$\xi_n = \mp \frac{n}{2\pi s} \frac{\sqrt{\pi}}{2^{\frac{1}{2}(n+1)} \Gamma(\frac{1}{2}n+1)} \left(1 \pm \frac{d}{d|\beta|}\right)^n |\beta|^{\frac{1}{2}(n+1)} K_{\frac{1}{2}(n+1)}(|\beta|).$$

The expressions for ξ_n can then be simplified using the recurrence relations for K_ν and its derivatives (Watson 1922).

Watson (1922) also gives a formula for the sine integral in (A 6) in terms of Bessel functions I_ν and the modified Struve function L_ν . Unfortunately, an indeterminacy occurs for even values of n and the values of L_ν are not extensively tabulated.

However, tables of

$$\phi(x) = \int_0^\infty \frac{\sin t}{(x^2+t^2)^{\frac{1}{2}}} dt$$

and of $\phi'(x)$ have been given by Müller (1939). In terms of these,

$$\int_0^\infty \frac{\sin \beta u}{(1+u^2)^{\frac{1}{2}}} du = \phi(\beta)$$

and

$$\int_0^\infty \frac{\sin \beta u}{(1+u^2)^{\frac{3}{2}}} du = -\beta \phi'(\beta);$$

also

$$d/d\beta(\beta \phi') = \beta \phi(\beta) - 1.$$

By means of these relations, formulae for η_1 and η_3 can be obtained. To calculate the expressions for η_2 and η_4 we use the relations

$$\begin{aligned} \int_0^\infty \frac{\sin \beta u}{1+u^2} du &= \frac{1}{2} [\exp(-\beta) \bar{\text{Ei}}(\beta) - \exp(\beta) \text{Ei}(-\beta)], \\ \int_0^\infty \frac{\sin \beta u}{(1+u^2)^2} du &= \frac{1}{2} \left[1 - \beta \frac{d}{d\beta}\right] \int_0^\infty \frac{\sin \beta u}{1+u^2} du, \\ \int_0^\infty \frac{\sin \beta u}{(1+u^2)^3} du &= \frac{1}{8} \left[3 - \beta \frac{d}{d\beta}\right] \left[1 - \beta \frac{d}{d\beta}\right] \int_0^\infty \frac{\sin \beta u}{1+u^2} du, \\ \frac{d}{d\beta} \text{Ei}(-\beta) &= \frac{\exp(-\beta)}{\beta}, \\ \frac{d}{d\beta} \bar{\text{Ei}}(\beta) &= \frac{\exp(\beta)}{\beta}, \end{aligned}$$

where the functions $\bar{\text{Ei}}(\beta)$ and $\text{Ei}(-\beta)$ are defined and tabulated by Jahnke & Emde (1933). The final expressions for ξ_n and η_n are

$$\begin{aligned}\xi_1 &= \frac{|\beta|}{2\pi s} (K_0(|\beta|) \mp K_1(|\beta|)); \\ \eta_1 &= \frac{|\beta|}{2\pi s} (\phi(|\beta|) \pm \phi'(|\beta|)); \\ \xi_2 &= 0 \quad \text{for } \beta > 0, \\ &= \frac{1}{2\pi s} 2\pi |\beta| \exp(-|\beta|) \quad \text{for } \beta < 0; \\ \eta_2 &= -\frac{1}{2\pi s} (2\beta \exp(\beta) \text{Ei}(-\beta) + 1) \quad \text{for } \beta > 0, \\ &= \frac{1}{2\pi s} (2|\beta| \exp(-|\beta|) \bar{\text{Ei}}(|\beta|) - 1) \quad \text{for } \beta < 0; \\ \xi_3 &= \frac{|\beta|}{2\pi s} \{4|\beta| [K_1(|\beta|) \mp K_0(|\beta|)] - 3K_0(|\beta|) \pm K_1(|\beta|)\}; \\ \eta_3 &= \frac{|\beta|}{2\pi s} \{\pm 4 - (3 \pm 4|\beta|) \phi(|\beta|) - (4|\beta| \pm 1) \phi'(|\beta|)\}; \\ \xi_4 &= 0 \quad \text{for } \beta > 0, \\ &= \frac{|\beta|}{2\pi s} 4\pi \exp(-|\beta|) (|\beta| - 1) \quad \text{for } \beta < 0; \\ \eta_4 &= \frac{1}{2\pi s} \{4\beta(\beta + 1) \exp(\beta) \text{Ei}(-\beta) + 4\beta + 1\} \quad \text{for } \beta > 0, \\ &= \frac{1}{2\pi s} \{4|\beta| (|\beta| - 1) \exp(-|\beta|) \bar{\text{Ei}}(|\beta|) - 4|\beta| + 1\} \quad \text{for } \beta < 0.\end{aligned}$$

With these expressions for ξ_n and η_n the locus of the centre of the final circle can be drawn for all important values of n as shown in figures 11 to 14.

REFERENCES

- Bassett, G. A., Menter, J. W. & Pashley, D. W. 1958 *Proc. Roy. Soc. A*, **246**, 345.
 Bollmann, W. 1956 *Phys. Rev.* **103**, 1588.
 Bollmann, W. 1957 *Proceedings of the Stockholm Conference on Electron Microscopy*, p. 316. Stockholm: Almqvist and Wiksell.
 Bonse, U. 1958 *Z. Phys.* **153**, 278.
 Bonse, U. & Kappler, E. 1958 *Z. Naturf.* **13a**, 348.
 Borrmann, G. 1941 *Phys. Z.* **42**, 157.
 Borrmann, G. 1950 *Z. Phys.* **127**, 297.
 Borrmann, G., Hartwig, W. & Irmeler, H. 1958 *Z. Naturf.* **13a**, 423.
 Bradley D. E. & Phillips, R. 1957 *Proc. Phys. Soc. B*, **70**, 533.
 Dowell, W. C. T., Farrant, J. L. & Rees, A. L. G. 1958 *Report of Fourth International Conference on Electron Microscopy*. Berlin: Springer-Verlag. (In the Press.)
 Franklin, R. E. 1950 *Acta. Cryst.* **3**, 107.
 Haine, M. E. 1957 *J. Sci. Instrum.* **34**, 9.
 Hashimoto, H. & Uyeda, R. 1957 *Acta Cryst.* **10**, 143.

- Hashimoto, H., Naiki, T. & Mannami, M. 1958 *Report of Fourth International Conference on Electron Microscopy*. Berlin: Springer-Verlag. (In the Press.)
- Heidenreich, R. D. 1949 *J. Appl. Phys.* **20**, 993.
- Hirsch, P. B. 1959 *Metallurg. Rev.* **4**, 101.
- Hirsch, P. B., Horne, R. W. & Whelan, M. J. 1956 *Phil. Mag.* **1**, 677.
- Hirsch, P. B., Silcox, J., Smallman, R. E. & Westmacott, K. H. 1958 *Phil. Mag.* **3**, 897.
- Jahnke, E. & Emde, F. 1933 *Tables of functions*, p. 78. Leipzig: Teubner.
- Kamiya, Y., Nonoyama, M., Tochigi, H. & Uyeda, R. 1958 *Report of Fourth International Conference on Electron Microscopy*. Berlin: Springer-Verlag. (In the Press.)
- Kato, N. 1952*a* *J. Phys. Soc. Japan*, **7**, 397.
- Kato, N. 1952*b* *J. Phys. Soc. Japan*, **7**, 406.
- Kato, N. 1953 *J. Phys. Soc. Japan*, **8**, 350.
- Lang, A. R. 1958 *J. Appl. Phys.* **29**, 597.
- Lenz, F. 1954 *Z. Naturf.* **9a**, 185.
- Lenz, F. 1958 *Report of Fourth International Conference on Electron Microscopy*. Berlin: Springer-Verlag. (In the Press.)
- Menter, J. W. 1956 *Proc. Roy. Soc. A*, **236**, 119.
- Menter, J. W. 1958 *Advanc. Phys.* **7**, 299.
- Mott, N. F. & Massey, H. S. W. 1933 *The theory of atomic collisions*, p. 87. Oxford: Clarendon Press.
- Müller, R. 1939 *Z. Angew Math. Mech.* **19**, 36.
- Newkirk, J. B. 1958 *J. Appl. Phys.* **29**, 995.
- Nicholson, R. B. & Nutting, J. 1958 *Phil. Mag.* **3**, 531.
- Niehirs, H. 1958*a, b* *Report of Fourth International Conference on Electron Microscopy*. Berlin: Springer-Verlag. (In the Press.)
- Nutting, J. 1959 Article in *The structure of metals*. London: Iliffe.
- Paterson, M. S. 1952 *J. Appl. Phys.* **23**, 805.
- Read, W. T. 1953 *Dislocations in crystals*, p. 18. New York: McGraw-Hill.
- Scherzer, O. 1949 *J. Appl. Phys.* **20**, 20.
- Thomas, G. & Whelan, M. J. 1959 *Phil. Mag.* **4**, 511.
- Thompson, N. 1953 *Proc. Phys. Soc. B*, **66**, 481.
- Watson, G. N. 1922 *Theory of Bessel Functions*, pp. 172, 332. Cambridge University Press.
- Whelan, M. J. 1959 *Proc. Roy. Soc. A*, **249**, 114.
- Whelan, M. J. & Hirsch, P. B. 1957*a* *Phil. Mag.* **2**, 1121.
- Whelan, M. J. & Hirsch, P. B. 1957*b* *Phil. Mag.* **2**, 1303.
- Whelan, M. J., Hirsch, P. B., Horne, R. W. & Bollmann, W. 1957 *Proc. Roy. Soc. A*, **240**, 524.
- Willis, B. T. M. 1957 *Proc. Roy. Soc. A*, **239**, 192.
- Wilson, A. J. C. 1950 *Research*, **3**, 387.

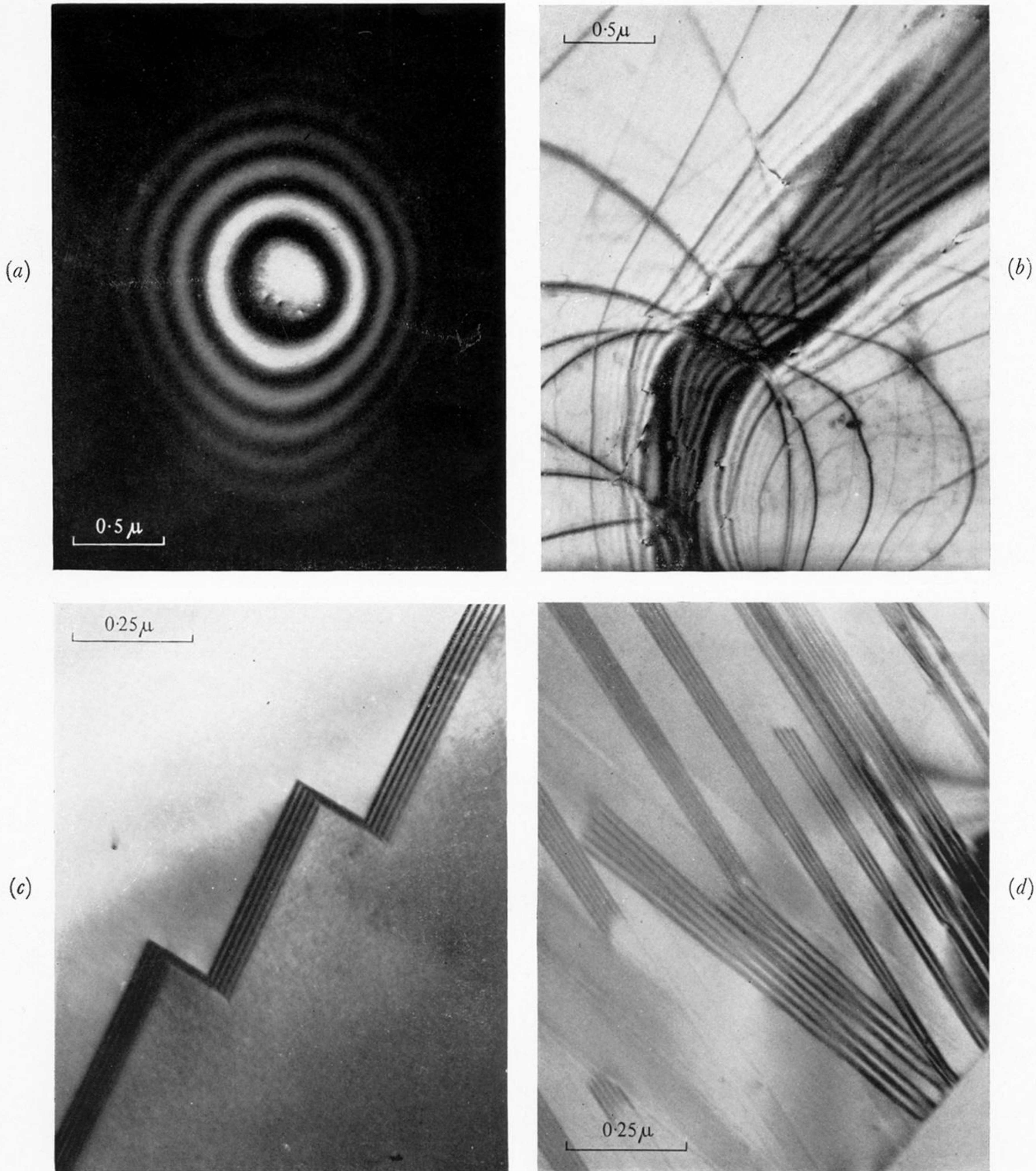
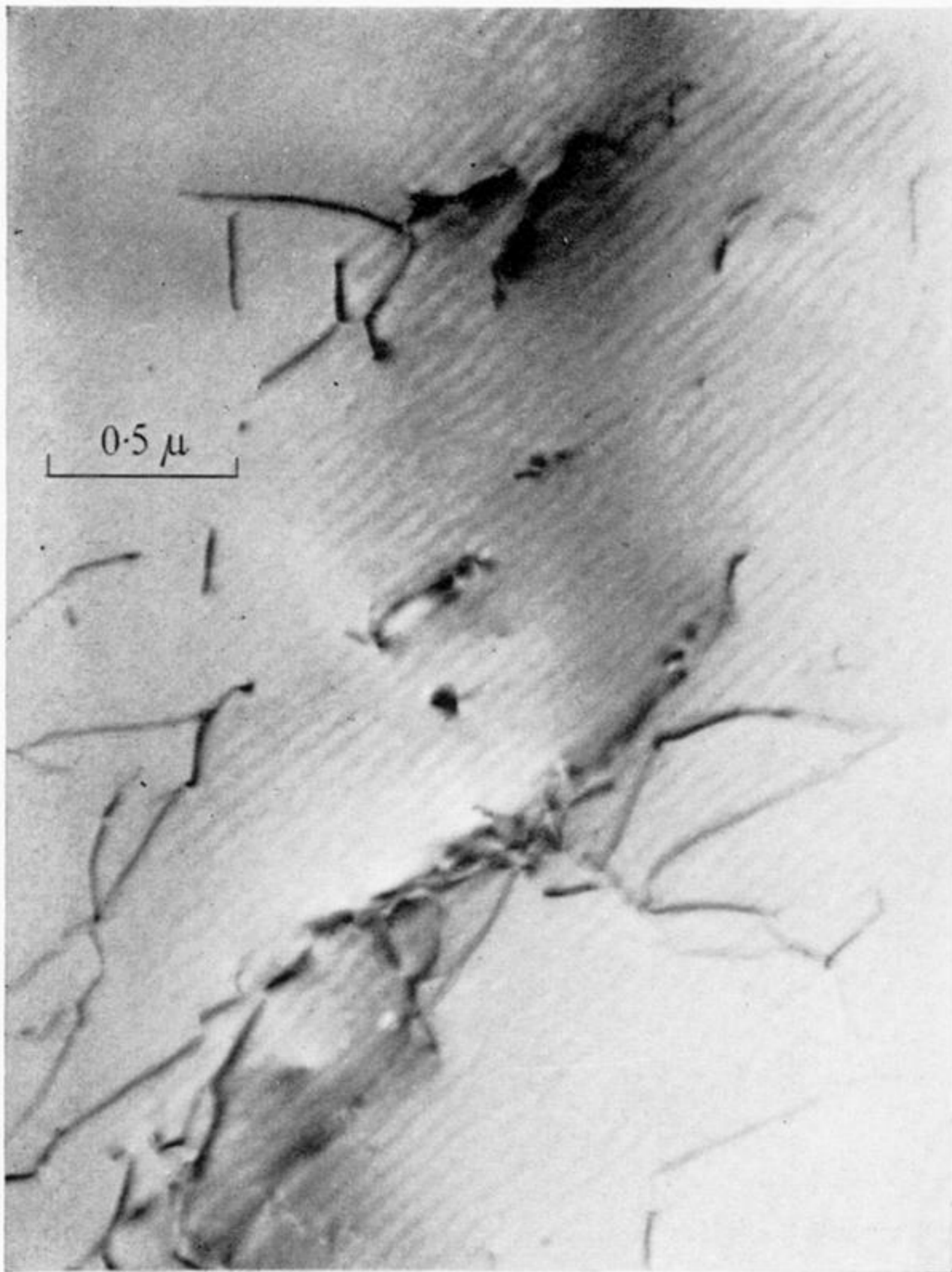


FIGURE 5. Examples of fringes in thin metal foils. (a) Thickness extinction contours in aluminium around a nearly circular depression. (Magn. $\times 30\,000$.) (b) Extinction contours in aluminium due to buckling of the foil. (Magn. $\times 30\,000$.) (c) Fringes at a twin boundary in stainless steel. (Magn. $\times 60\,000$.) (d) Fringes at stacking faults in stainless steel. (Magn. $\times 80\,000$.)

(a)



(b)

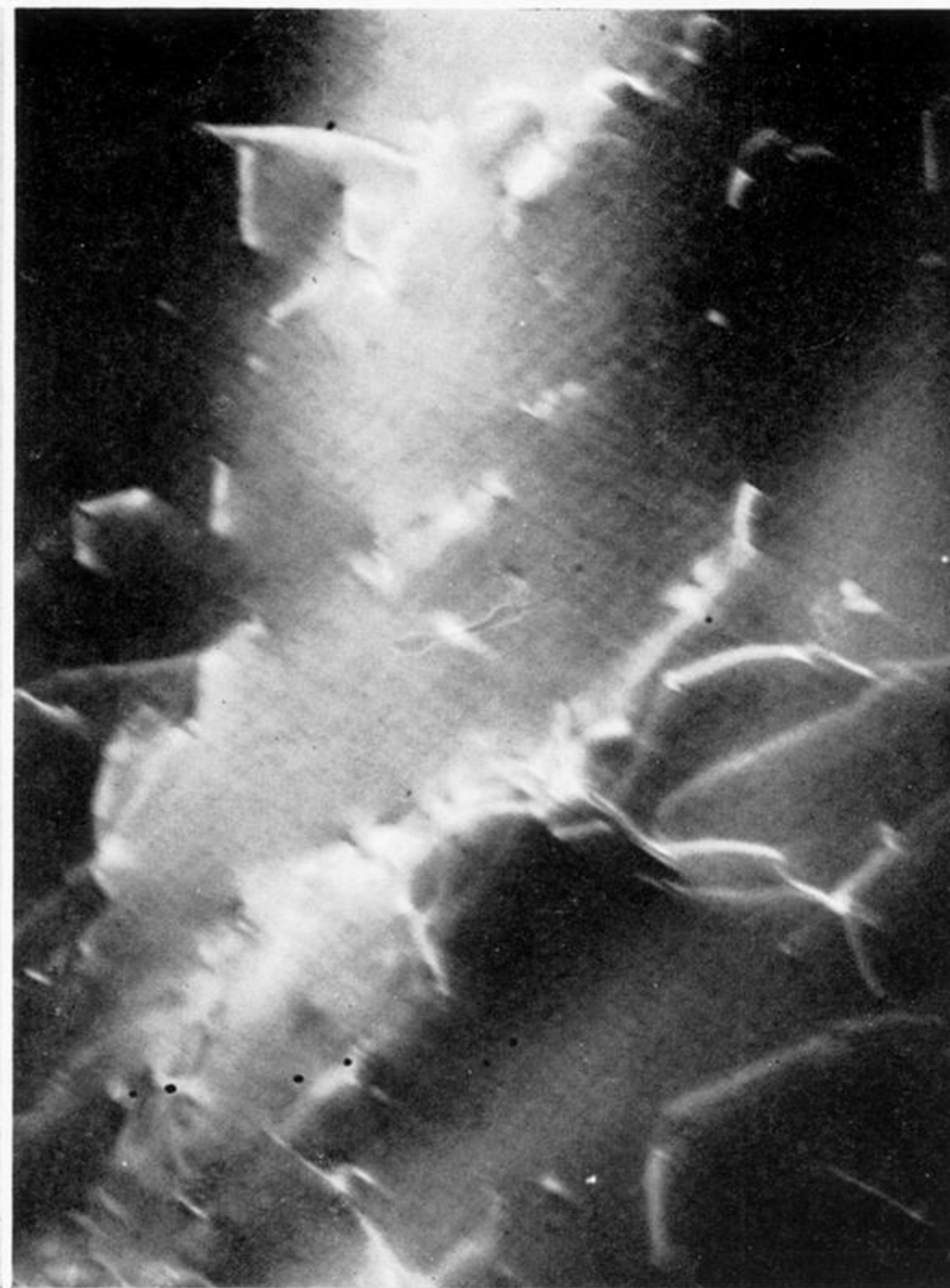


FIGURE 19. Bright field and dark field images of dislocations in aluminium. Note that the dislocations appear as light lines on the dark field image and as dark lines on the bright field image. (Magn. $\times 30\,000$.)

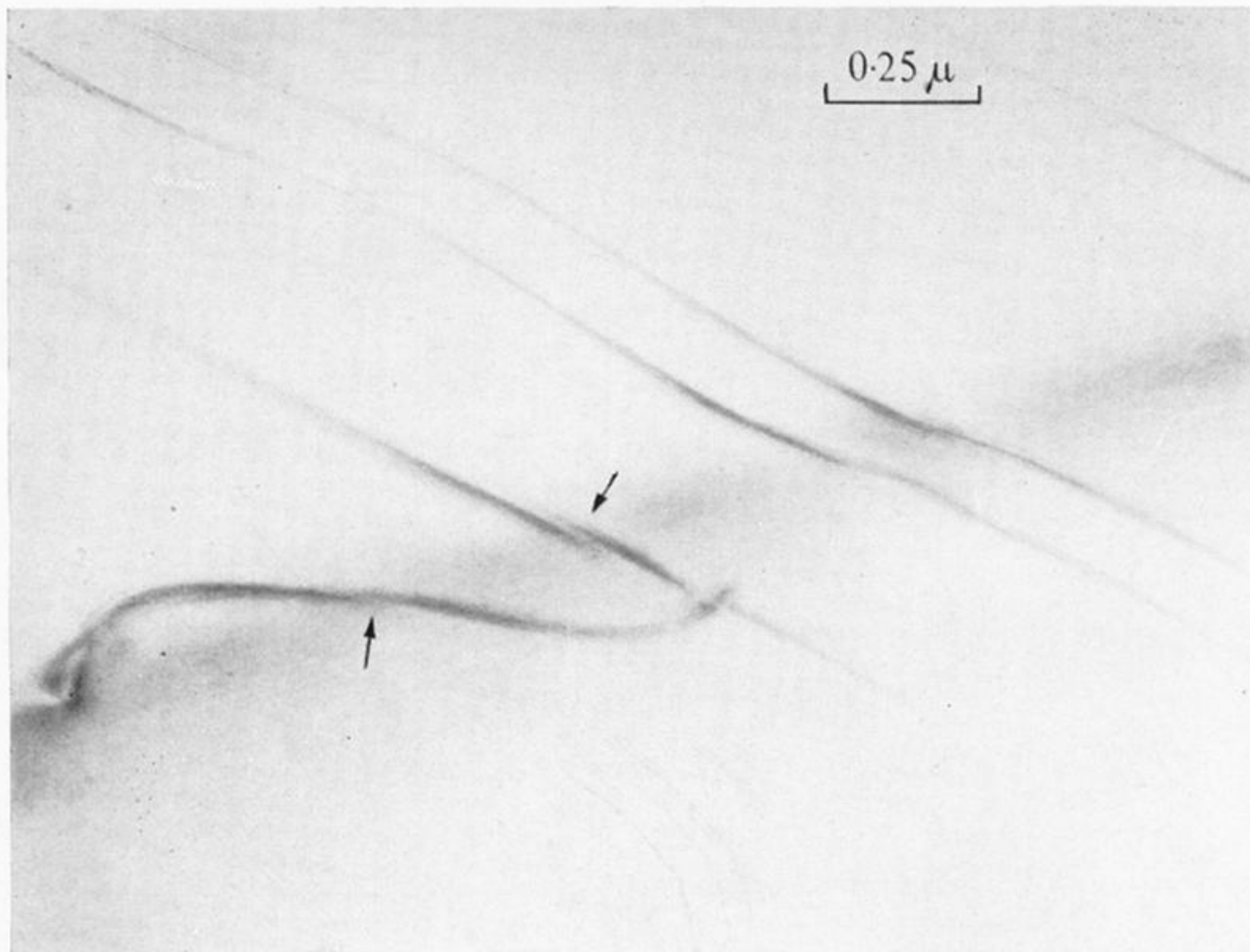
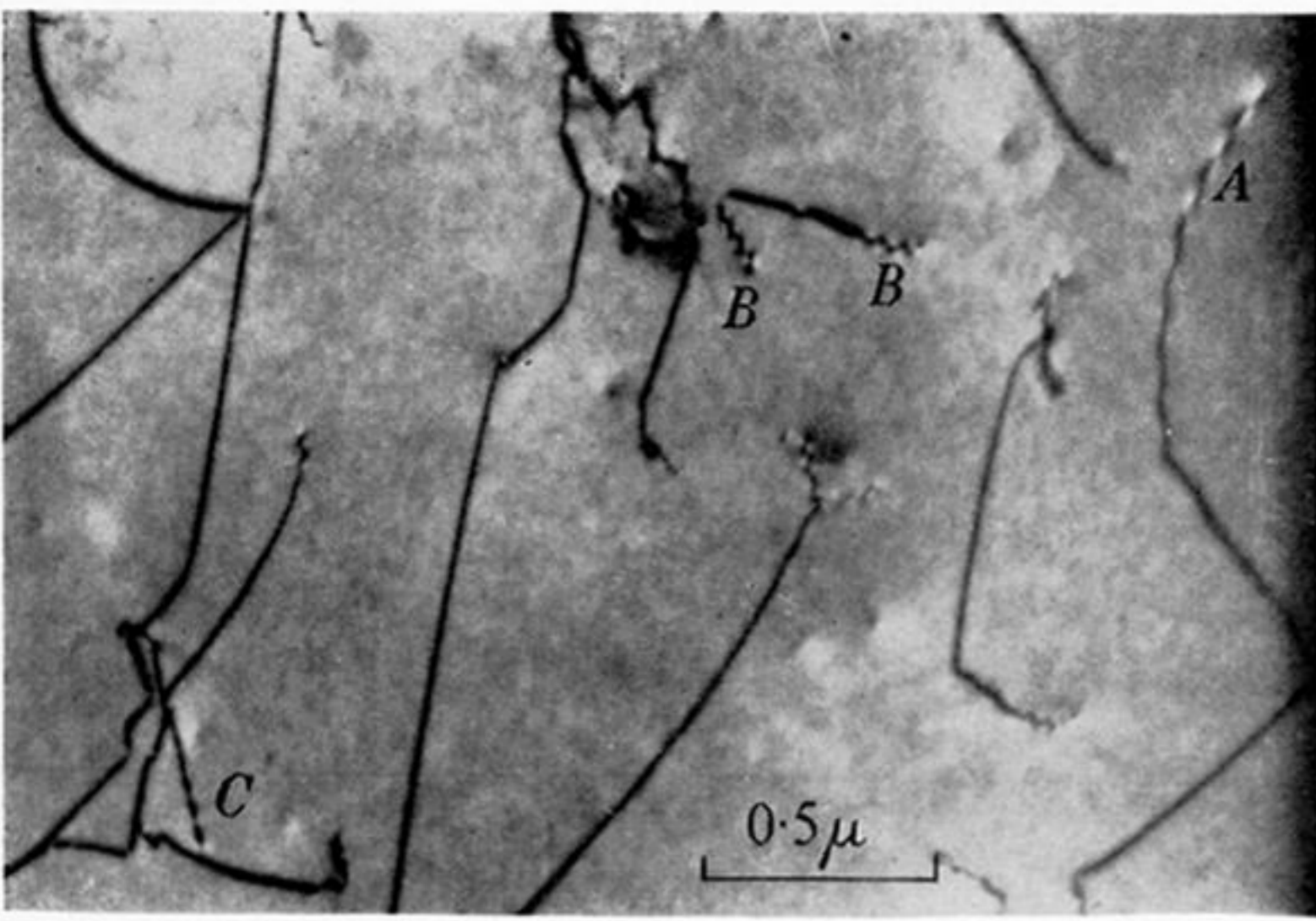
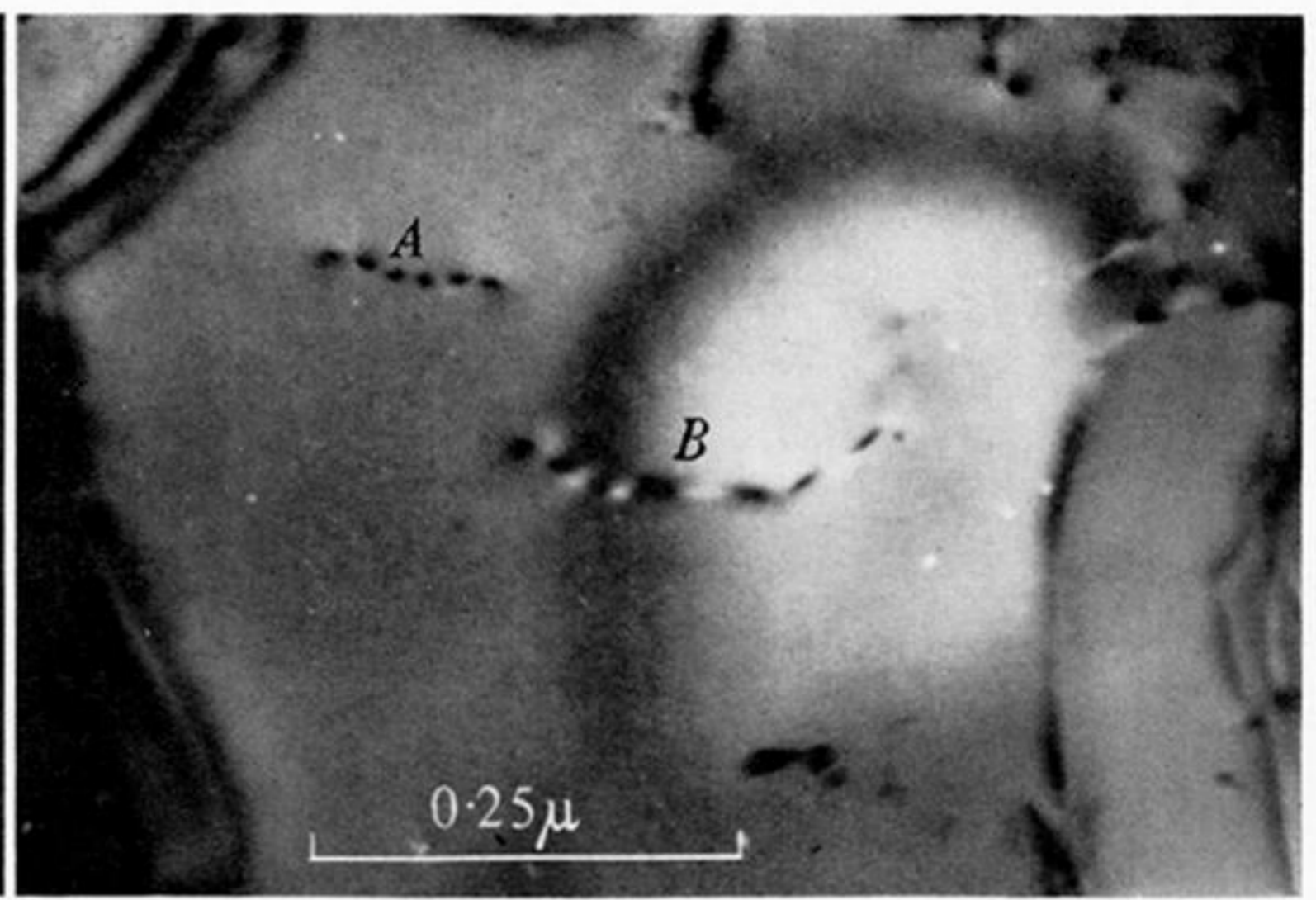


FIGURE 20. Micrograph illustrating the one-sided nature of dislocation contrast in aluminium. Note that the contrast changes from one side of the dislocation to the other where the dislocation crosses the extinction contour. Note also the rapid decrease in contrast on the side facing the dislocation and slower decrease on the other side. The width and total intensity of the image is a maximum on the edge of the extinction contour. (Magn. $\times 50\,000$.)

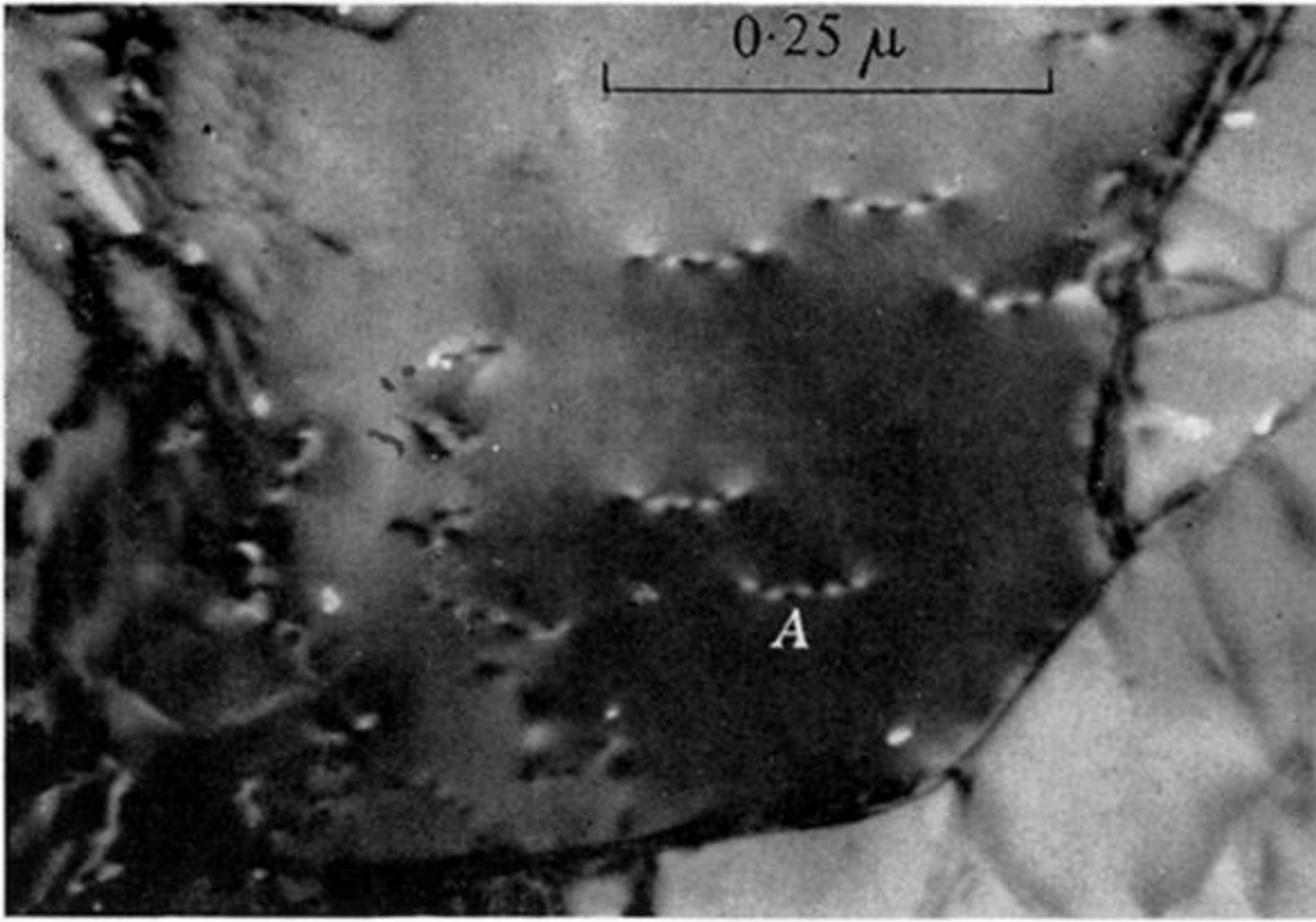
(a)



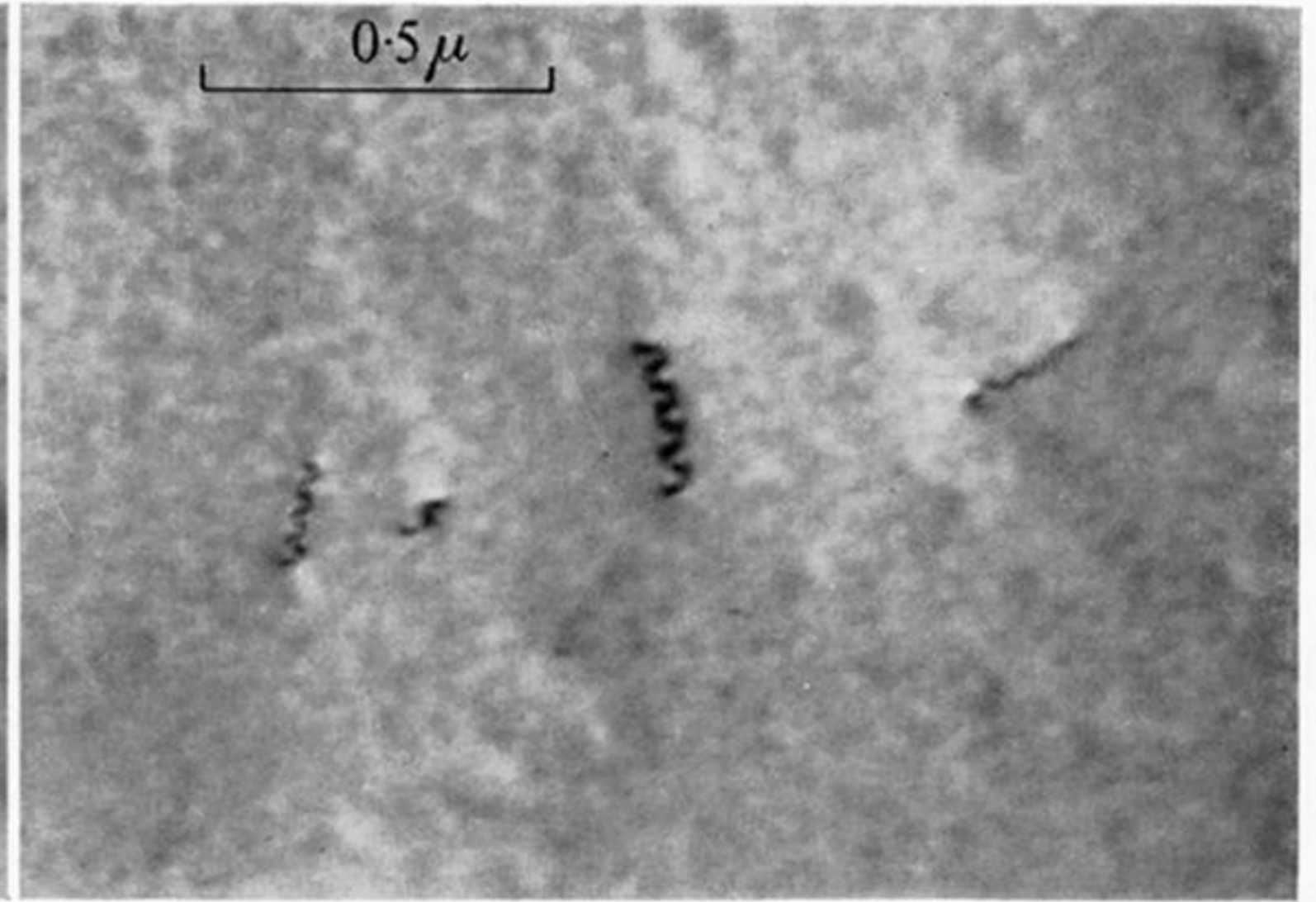
(b)



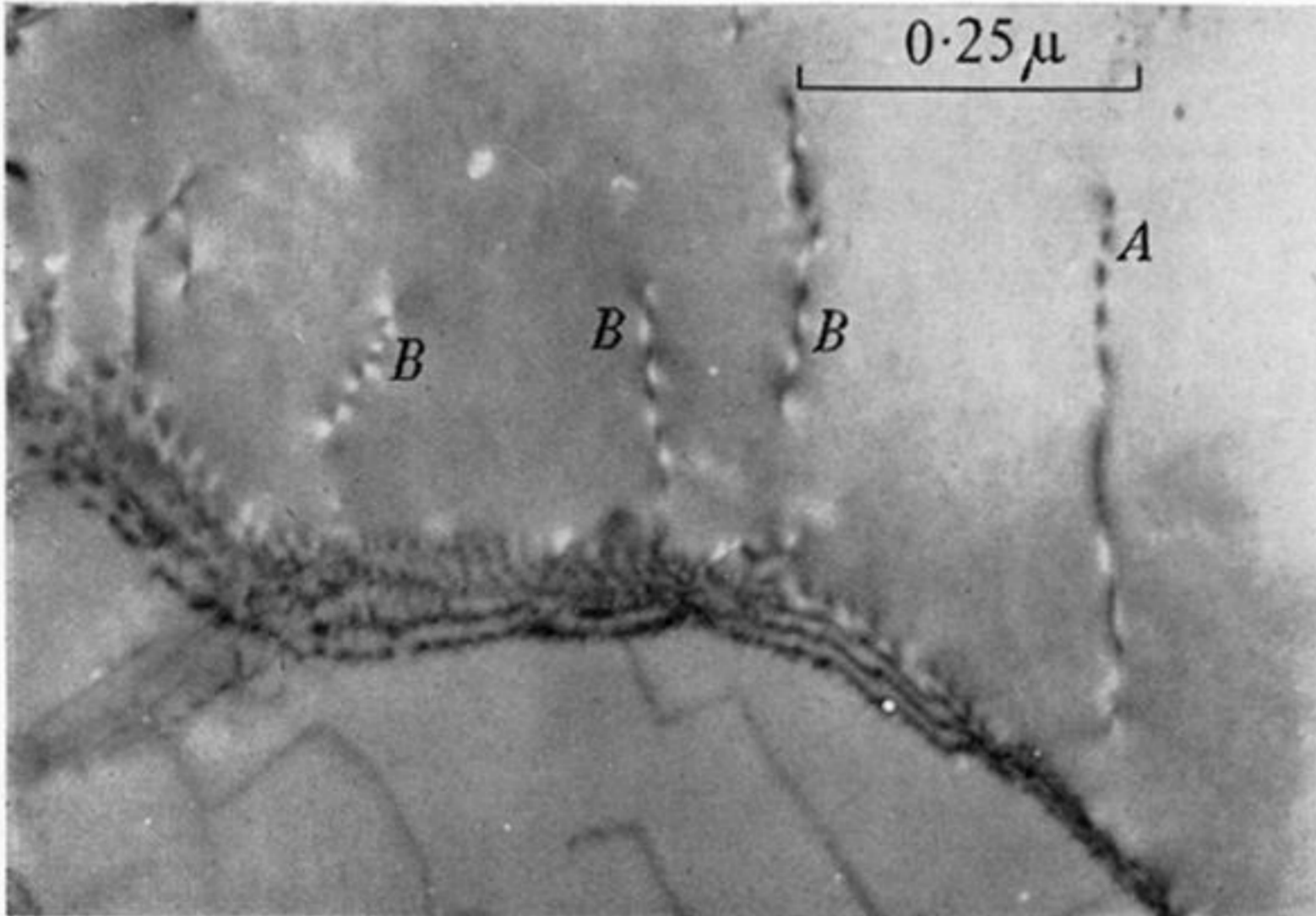
(c)



(d)



(e)



(f)

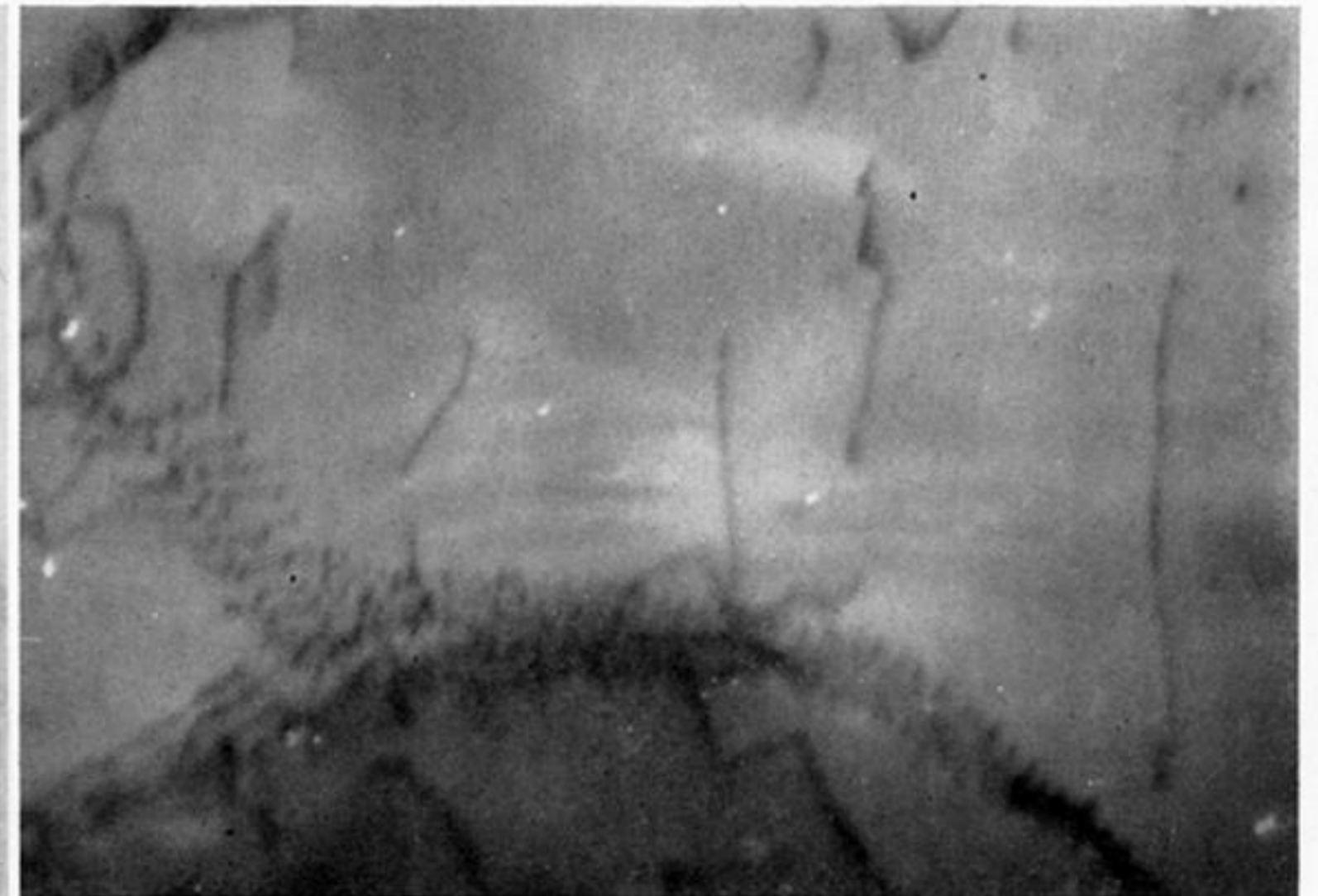


FIGURE 21. Micrographs of aluminium showing special contrast effects at dislocations. (a) *A*, alternating black-white appearance, *B*, zigzag contrast, *C*, dotted contrast. (Magn. $\times 26\,000$.) (b) *A*, dotted contrast; *B*, alternating black and white contrast. (Magn. $\times 100\,000$.) (c) Dotted, white contrast at dislocations in region of dark extinction contour. (Magn. $\times 100\,000$.) (d) Zigzag contrast. (Magn. $\times 40\,000$.) (e) *A*, dotted contrast; *B*, zigzag contrast. (Magn. $\times 75\,000$.) (f) Same area as (e) after tilting the specimen. (Magn. $\times 75\,000$.)

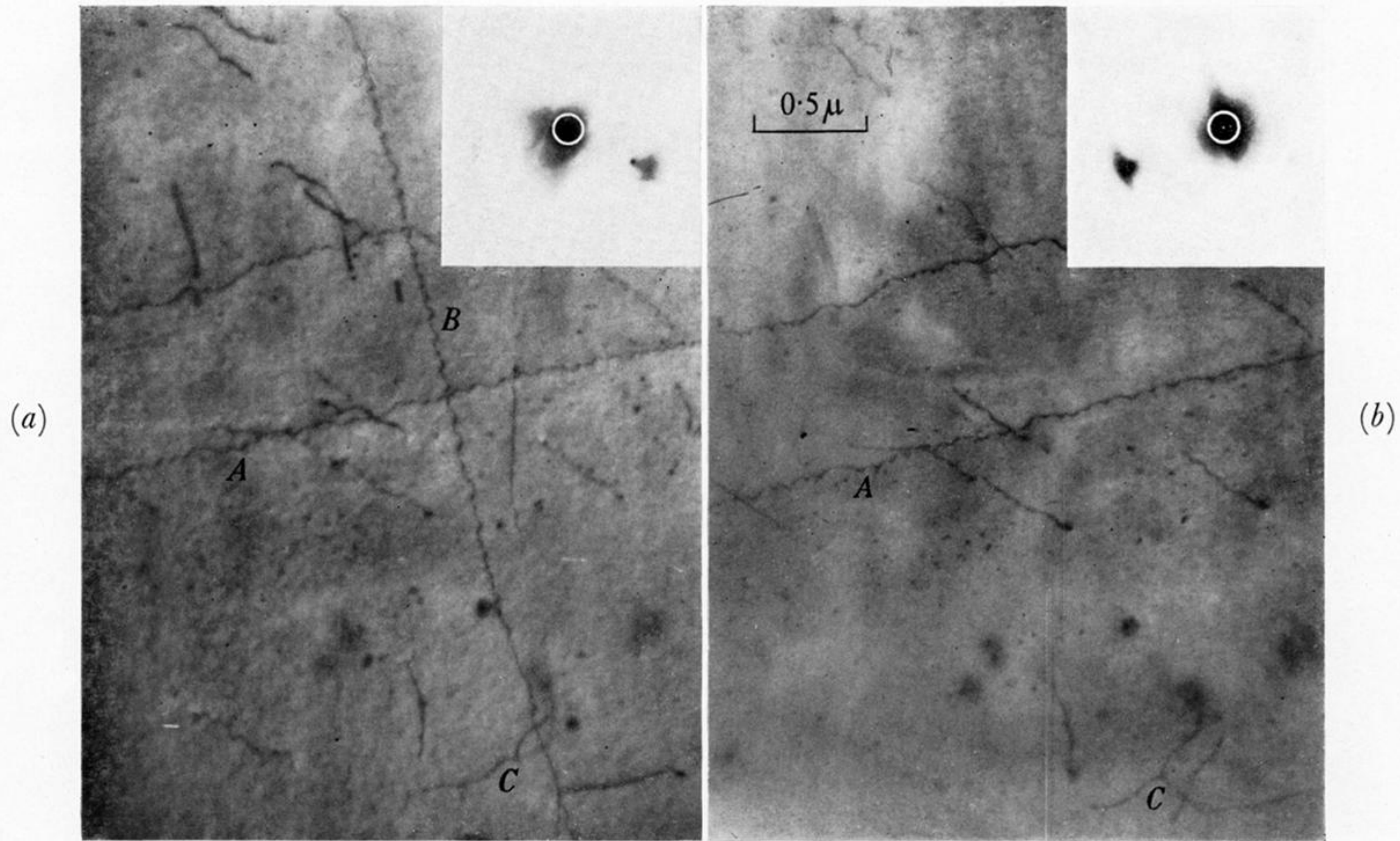


FIGURE 22. Sequence of micrographs (and diffraction patterns) of quenched aluminium + 4% copper alloy showing two helical dislocations *A* and *B*. After tilting dislocation *B* has vanished. Another dislocation has appeared at *C*. (Magn. $\times 25\,000$.)

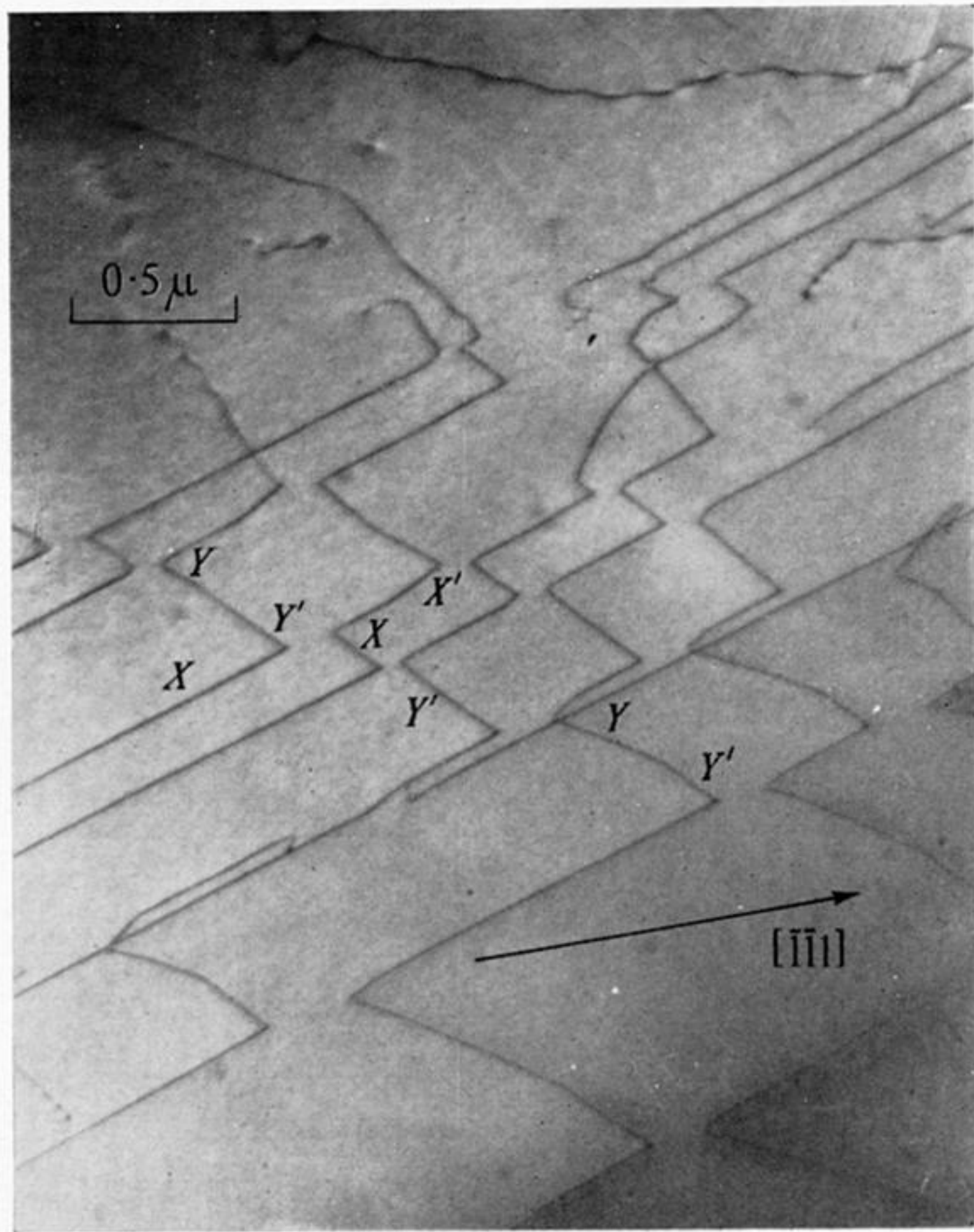


FIGURE 23. Interaction of two sets of dislocations X and Y to produce a resultant dislocation which is invisible. The normal to the foil is $[213]$. See figure 24 and text for interpretation. (Magn. $\times 25\,000$.)

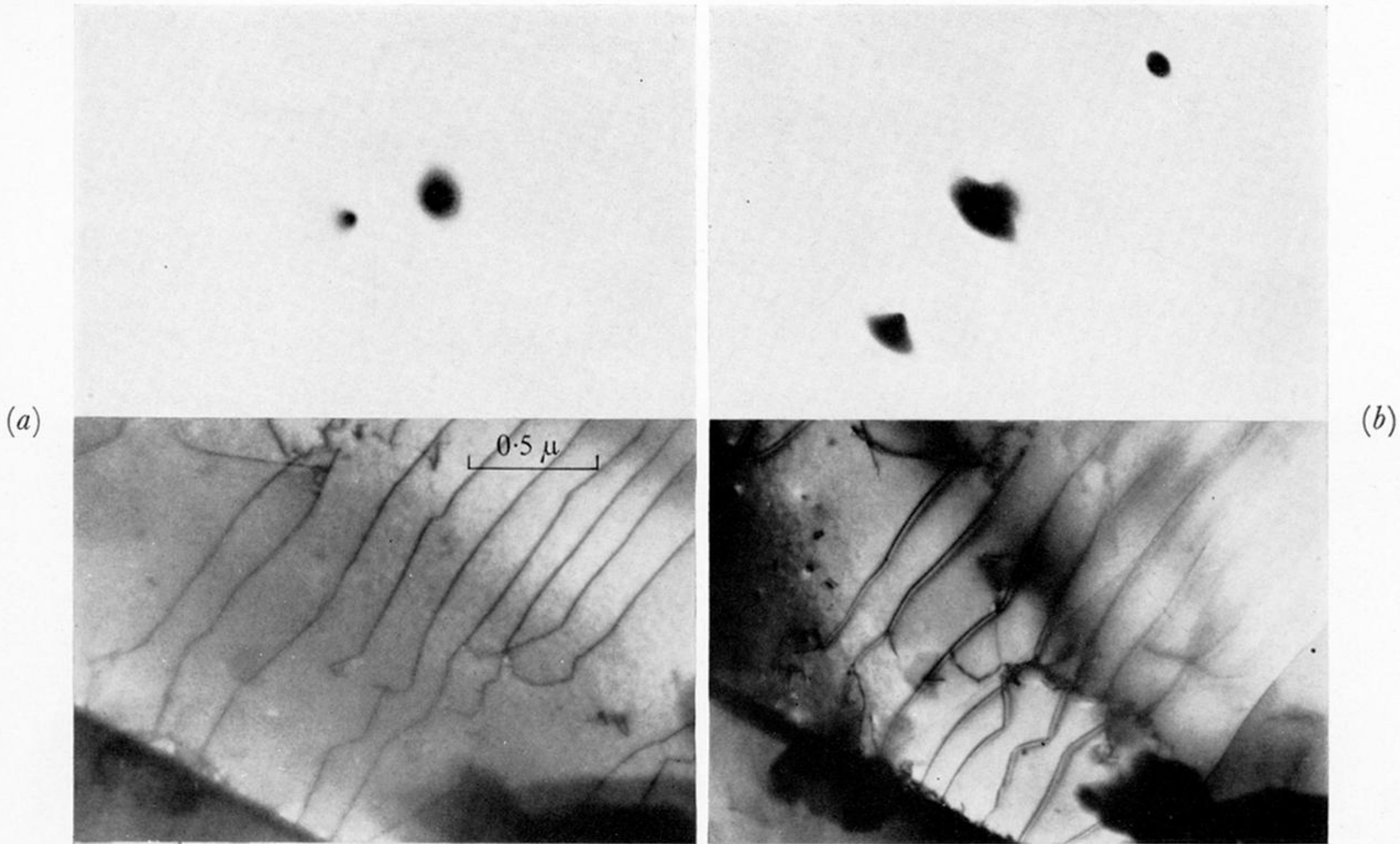


FIGURE 25. Micrographs of nickel showing (a) single images and (b) double images in the same area. Corresponding diffraction patterns are shown. See text for discussion. (Magn. $\times 30\,000$.)

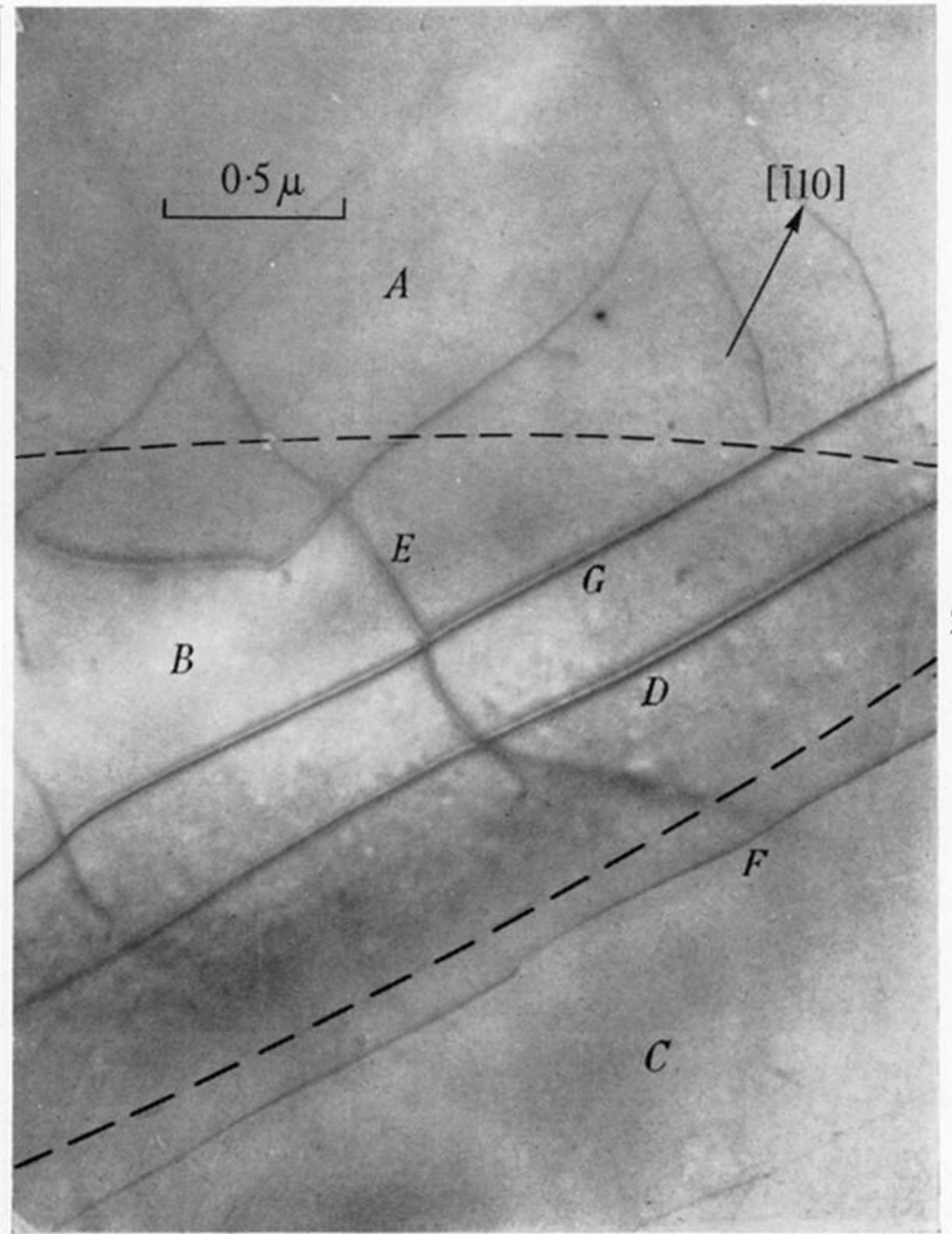
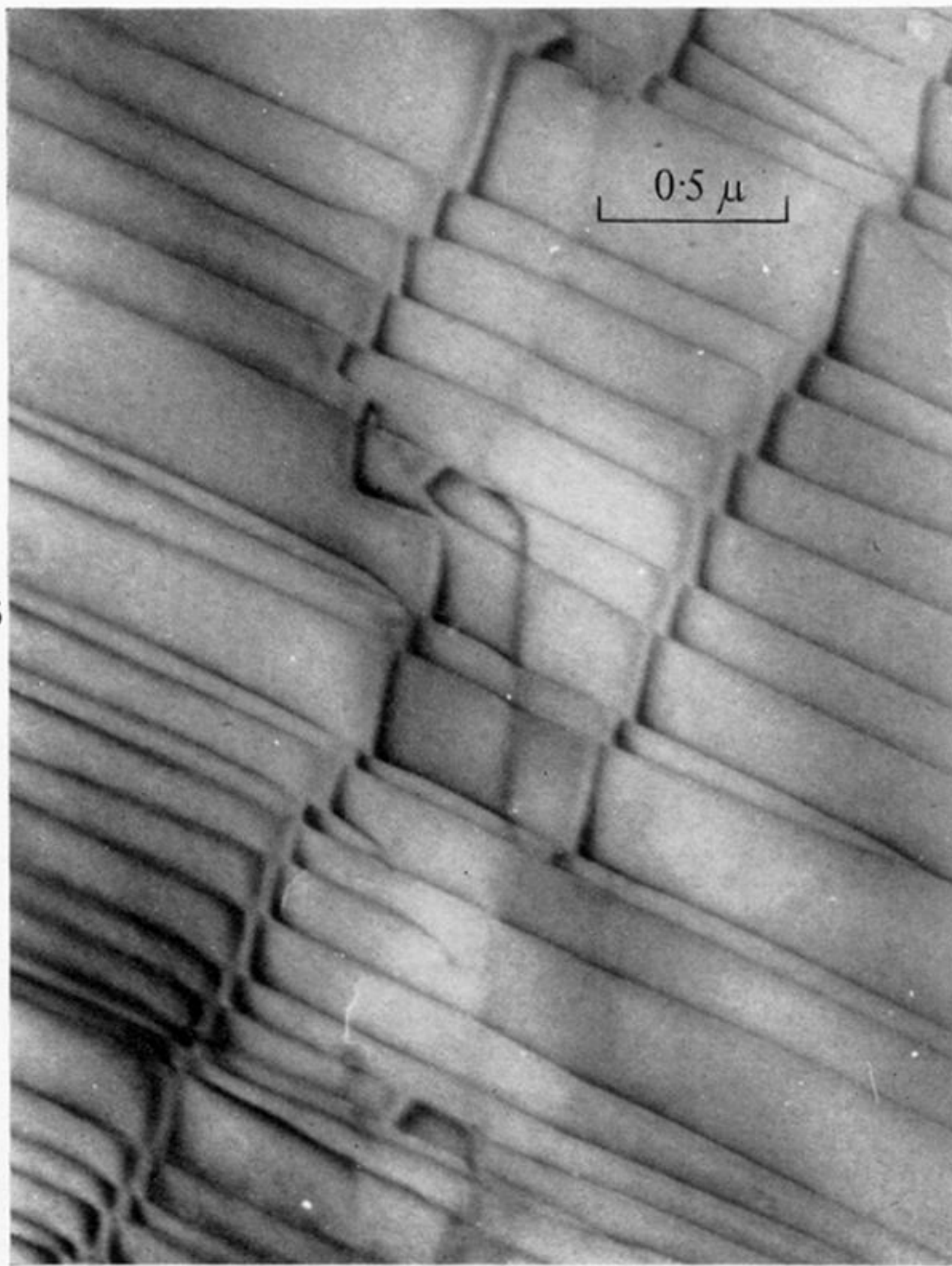


FIGURE 26. Micrograph of interacting dislocations in aluminium. Note the wide double images for one type of dislocation. See text for discussion. (Magn. $\times 30\,000$.)

FIGURE 27. Region showing double images of dislocations in aluminium. The approximate centres of high-order extinction contours are marked with broken lines. See text for discussion. (Magn. $\times 26\,000$.)

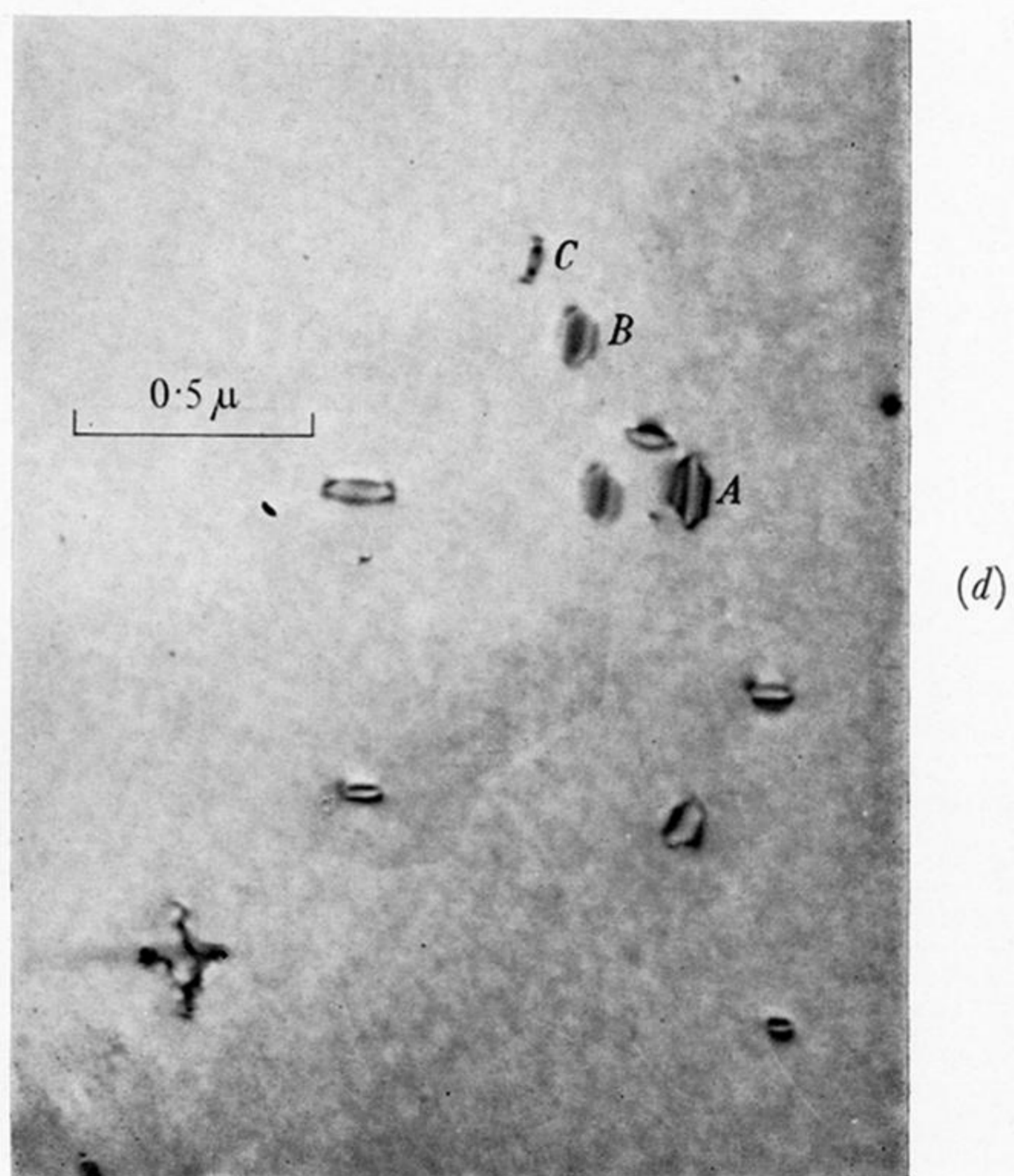
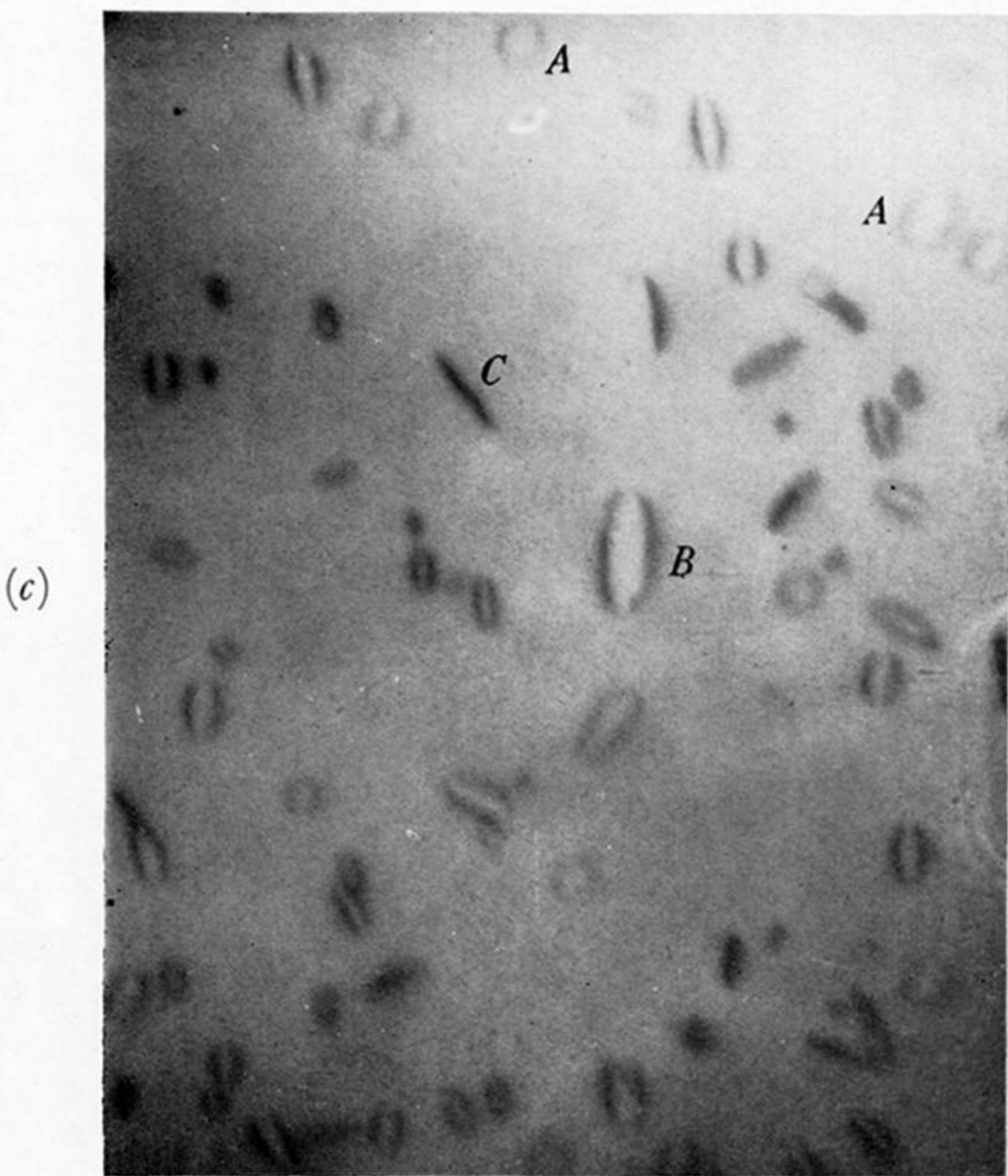
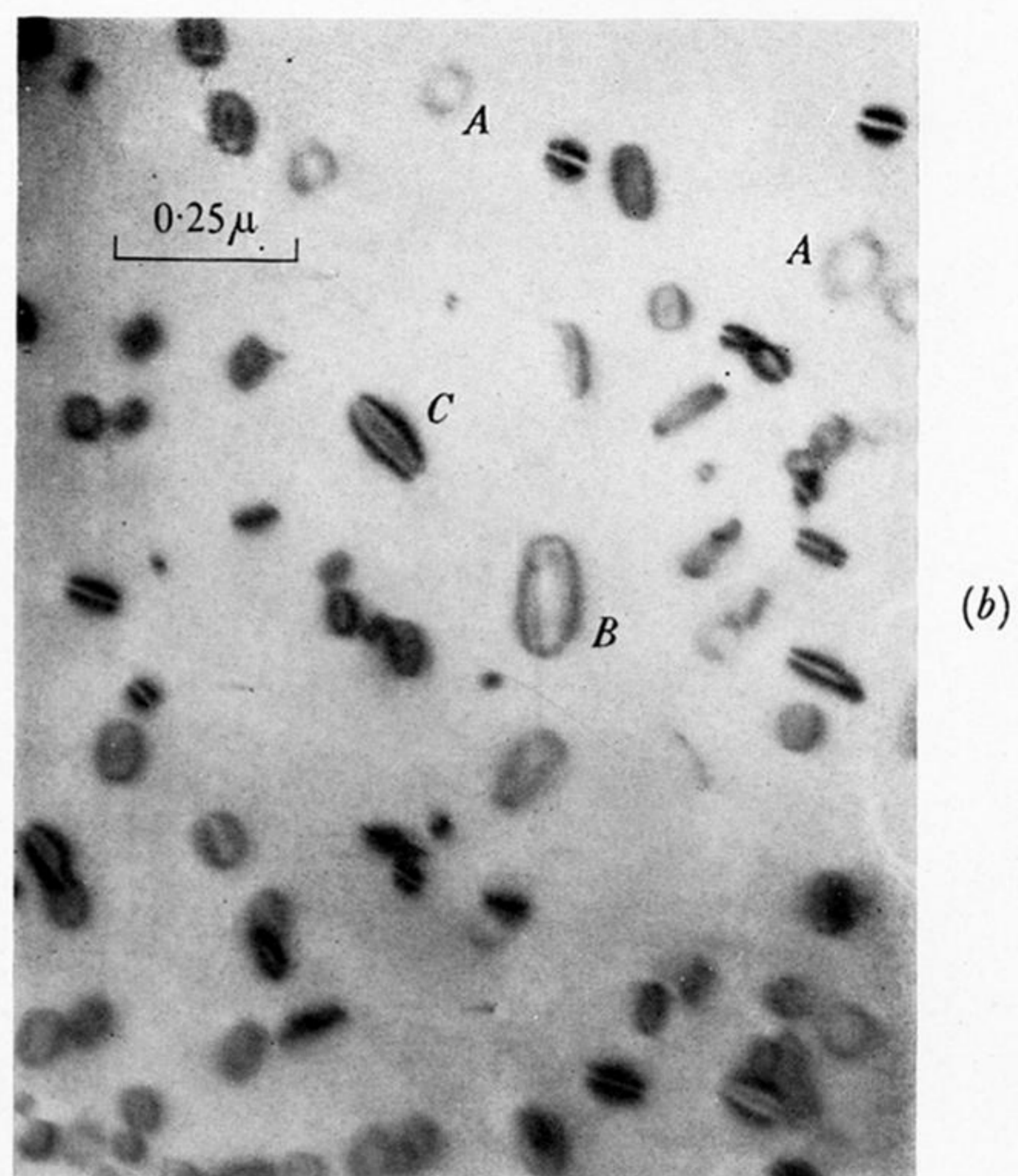
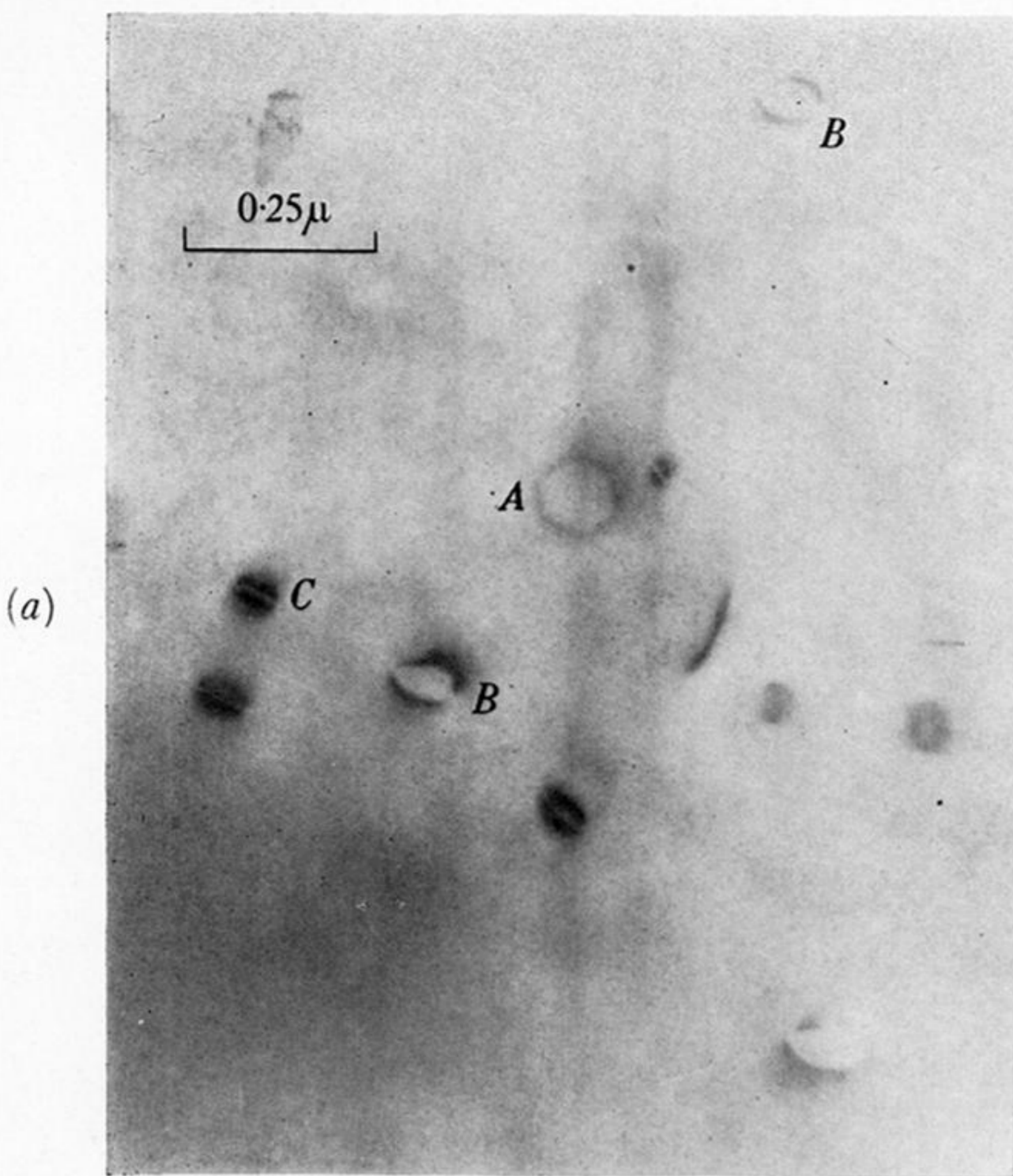
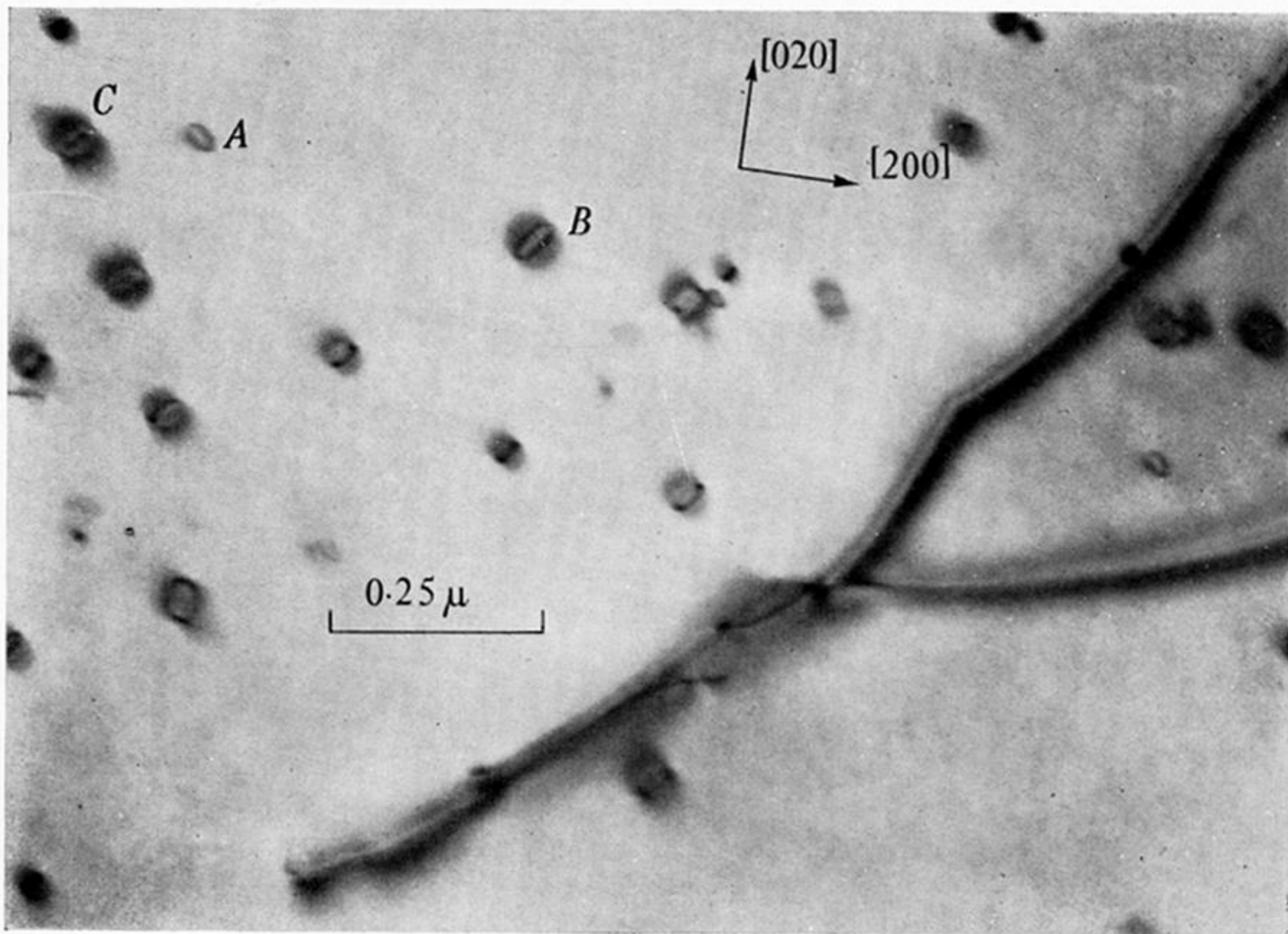
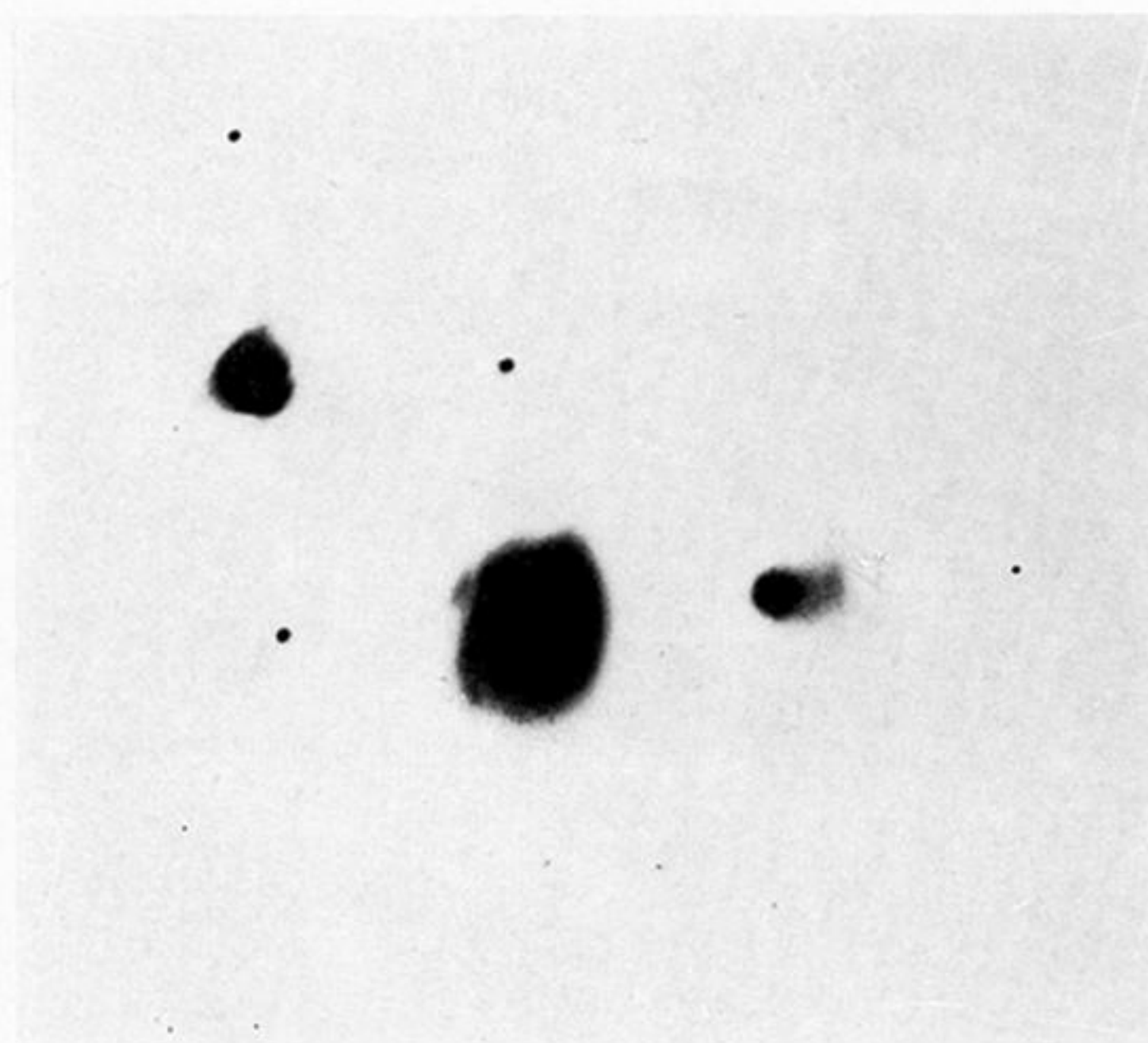


FIGURE 28. Images of dislocation loops in quenched aluminium. (a) *A*, hexagonal loop lying in a plane nearly parallel to the foil surface showing uniform contrast. Loops *B* and *C* are on inclined planes and the more steeply inclined parts are less visible. (Magn. $\times 65\,000$.) (b) *A*, dislocation with nearly uniform contrast. *B*, *C*, double images of dislocation loops. (Magn. $\times 60\,000$.) (c) Same area as (b) after tilting. (Magn. $\times 60\,000$.) (d) *A*, *B*, hexagonal loops showing double images. *C*, dotted appearance of a loop thought to be lying in a plane normal to that of the foil. (Magn. $\times 40\,000$.)



(a)



(b)

FIGURE 29. (a) Dislocation loops in quenched aluminium. Note the double images of loops at *B* and *C*. See text for discussion. (Magn. $\times 75\,000$.) (b) Selected area diffraction pattern from (a).